

https://dspace.org/

Geochronological studies in the Northern Scandinavian Caledonides, Finnmark Province, Northern Norway, new evidence for Grenvillian and Scandian components in the Kalak Nappe complex and the extent of the Mageroy Nappe

Gerber, Madelein

2006-11-14T13:21:00Z
http://hdl.handle.net/10539/1716

Downloaded from a DSpace repository. https://dspace.org/

GEOCHRONOLOGICAL STUDIES IN THE NORTHERN SCANDINAVIAN CALEDONIDES, FINNMARK PROVINCE, NORTHERN NORWAY: NEW EVIDENCE FOR *GRENVILLIAN* AND *SCANDIAN* COMPONENTS IN THE KALAK NAPPE COMPLEX, AND THE EXTENT OF THE MAGERØY NAPPE.

Madelein Gerber

A dissertation submitted to the Faculty of Science, University of the Witwatersrand, in fulfilment of the requirements for the degree of Master of Science.

Johannesburg, 2006

I declare that this dissertation is my own, unaided work. It is being submitted for the Degree of Master of Science by research in the University of the Witwatersrand, Johannesburg. It has not been submitted before for any degree or examination in any other University.

_____

M. Gerber

_____ day of January, 2006.

Abstract

U-Pb ID-TIMS ages are reported for several magmatic and anatectic phases from the Kalak Nappe Complex (KNC), northern Norwegian Scandinavian Caledonides. Euhedral prismatic zircons from a suite of plutons intruding the metaturbidite sequences of the Hellefjord Group, Sørøy-Seiland Nappe (upper KNC) yielded intrusion ages of 440.9 ± 1.5 Ma for a syenogranite, and 435.9 ± 1.6 Ma and 436.7 ±0.8 Ma, respectively, for a granite and gabbro. The period of magmatic activity was followed closely by a phase of deformation associated with upper amphibolite-granulite facies metamorphism at c. 430 Ma. This caused local anatexis in the granite and growth of magmatic zircon (429.5 ± 1.4 Ma), as well as the common growth of metamorphic titanite (431.4 ± 1 Ma and 427.8 ±2.7 Ma). These late Ordovician-early Silurian ages link this tectonometamorphic activity to the *Scandian* phase of the Scandinavian Caledonian orogeny. Evidence for *Scandian* tectonometamorphic activity is also recorded at c. 425 Ma in the Klubben Group of the Olderfjord Nappe (lower KNC). This is documented by the intrusion of a granodiorite pegmatite (425.9 ±0.7 Ma) and anatexis of the Klubben Group (425.5 ± 1.3 Ma). In addition, the Klubben Group records a c. 980 Ma *Grenvillian* age for anatectic veins crosscutting an earlier fabric (980.9 ± 2.6 Ma, syenogranitic leucosome), linking the initial evolution of the Klubben Group to the amalgamation of Rodinia.

It is suggested that a previously undetected structural break exists in the Sørøy Succession of the KNC at base of the Hellefjord Group. This is supported by c. 441-436 Ma *Scandian* ages obtained for bimodal magmatic activity in the Hellefjord, which does not relate to the intrusion of the SIP further down in the Sørøy Succession at c. 570-560 and c. 530-520 Ma. In addition, *Scandian* magmatic ages have not been detected in the Sørøy Succession underlying the Hellefjord Group. However, these ages are coeval with bimodal plutons in the overlying Magerøy Nappe (c. 440-436 Ma), which is composed largely of metaturbidite sequences. The Hellefjord Group is suggested to represent an extension of the Magerøy Nappe, which evolved in a ridge-trench intersection.

A tentative window of c. 430-425 Ma is suggested for the thrusting of the Magerøy Nappe over the Kalak Nappe Complex, in light of the formation of deformational fabrics in the Hellefjord Group at c. 430 Ma and the localised c. 425 Ma anatexis recorded in the Klubben Group.

Carpe Diem...

Acknowledgments

This project was carried out within the framework of a joint research agreement between the National Research Councils of South Africa and Norway (project number: 152325/V10)

I would like to express my heartfelt thanks to the following individuals and institutions:

- My supervisors, Profs. Lew Ashwal (Wits University) and Fernando Corfu (Oslo University), for their endless patience and advice.
- Prof. Trond Torsvik, our counterpart at the Norwegian Geological Survey and logistics organiser during field seasons in Norway.
- Prof. Donald. M. Ramsay, for acting guide and advisor during field seasons.
- Mrs. Gunborg Bye Fjeld, Department of Geosciences, University of Oslo, for her immense help during my visit to their school.
- Dr. David Roberts (NGU, Norway) and Prof. D. Gebauer (ETH Zürich, Switzerland), for taking the time to answer the emails of a complete stranger.
- Dr. L. Den Drijver (UJ, South Africa), for her assistance in understanding ion exchange chromatography.
- The Department of Geosciences, Oslo University, for the use of their wet chemistry and TIMS facilities.
- The Analytical Department and staff at the University of Johannesburg for the use of their SEM.

- A special thanks to my family, for the many big and small ways in which they have made my studies possible.

- And to Dave... for absent advice, support and inspiration.

Contents

Declaration ..... **iii**
Abstract ..... **v**
Dedication ..... **vii**
Acknowledgements ..... **ix**
Contents ..... **xi**
List of figures ..... **xiii**
List of tables ..... **xv**
List of abbreviations ..... **xvii**

1. Introduction **1**
2. Geology **5**
3. Methods **11**
4. Sample descriptions **13**
4.1 C04-16 (Garnet-hornblende-syenogranite augen gneiss) – Sørøy Island 13
4.2 NM04-3 (Metagabbro) – Sørøy Island 15
4.3 NM04-9 (Migmatised granite gneiss) – Sørøy Island 18
4.4 RJR02-58b (Granodiorite pegmatite) – Magerøy Island 21
4.5 C04-2 (Granite leucosome) – Magerøy Island 22
4.6 NM04-16 (Syenogranite leucosome) – Magerøy Island 26
5. Results and discussion **31**
5.1 C04-16 (Garnet-hornblende-syenogranite augen gneiss) – Sørøy Island 31
5.2 NM04-3 (Metagabbro) – Sørøy Island 33
5.3 NM04-9 (Migmatised granite gneiss) – Sørøy Island 34
5.4 RJR02-58B (Granodiorite pegmatite) – Magerøy Island 37
5.5 C04-2 (Granitic leucosome) – Magerøy Island 38
5.6 NM04-16 (Syenogranitic leucosome) – Magerøy Island 39
6. Regional Implications **43**
***7.* Conclusions** **49**

Appendix A – Visually estimated modal proportions **51**
Appendix B – TIMS data **53**
Appendix C – Methods **55**
Appendix D – Data reduction **65**
Appendix E – Additional Theory: Zircon, Titanite and U-Th-Pb systematics **73**
References **79**

List of figures

1. Introduction

1.1 Schematic diagrams showing the events leading to the Caledonian Orogeny 2

1.2 Simplified tectonostratigraphy of the Finnmark Province, northern Norway 3

2. Geology

2.1 Simplified tectonostratigraphy for the Caledonian Nappes of the Finnmark Province 6

2.2 Simplified geology of the island of Sørøy, Finnmark Province 7

2.3 Simplified geology of the island of Magerøy, Finnmark Province 9

4. Sample descriptions

4.1 Photomicrographs of sample C04-16 14

4.2 Selections of zircons from sample C04-16 15

4.3 CL images for sample C04-16 16

4.4 Photograph of NM04-3 17

4.5 Photomicrographs of sample NM04-3 17

4.6 Selection of zircons from sample NM04-3 18

4.7 Photograph of NM04-9 19

4.8 Photomicrographs of sample NM04-9 20

4.9 Selection of zircons from NM04-9 20

4.10 CL images for sample NM04-9 21

4.11 Photographs of sample RJR02-58B 22

4.12 Photomicrographs for sample RJR02-58B 23

4.13 Selection of zircons for sample RJR02-58B 24

4.14 Photomicrographs for sample C04-2 24

4.15 Selection of zircons for sample C04-2 25

4.16 CL images for sample C04-2 25

4.17 Photograph of NM04-16 27

4.18 Photomicrographs of sample NM04-16 27

4.19 Selection of zircons from sample NM04-16 28

4.20 CL images for sample NM04-16 ..... 28, 29

5. Results and discussion

5.1 Concordia diagram for sample C04-16 32

5.2 Examples of titanite from sample C04-16 33

5.3 Concordia diagram for NM04-3 35

5.4 Selection of titanite from sample NM04-3 35

5.5 Concordia diagram for sample NM04-9 37

5.6 Concordia diagram for sample RJR02-58B 39

5.7 Concordia diagram for sample C04-2 ……. 40
5.8 Concordia diagram for sample NM04-18 ……. 41

6. Regional implications

6.1 Schematic summary of results ……. 44
6.2 Suggested tectonostratigraphy ……. 46

7. Conclusions

7.1 Timeline summarising the evolution of the Kalak Nappe Complex…… 50

Appendix A

A-1 Modal classification after Streckeisen (1976) …… 51

Appendix E

E-1 Schematic diagram of common zircon morphologies……. 74

List of tables

Appendix A

A-1 Visually estimated modal proportions …… 51

Appendix B

B-1 TIMS results …… 53

List of abbreviations:

A	Ampere
Al	Aluminium
AMU	Atomic mass unit
ap	Apatite
bt	Biotite
c.	Circa
Ca	Calcium
Ce	Cerium
chl	Chlorite
CL	Cathodoluminescence
Cl	Chlorine
F	Fluorine
g	Gram
Gd	Gadolinium
gnt	Garnet
GMC	Gjesvær Migmatite Complex
hbld	Hornblende
HCl	Hydrochloric acid
HF	Hydrofluoric acid
HG	Hellefjord Group
HNO_3	Nitric acid
Ho	Holmium
ID-TIMS	Isotope Dilution Thermal Ionization Mass Spectrometry
k-	Kilo-
KNC	Kalak Nappe Complex
KG	Klubben Group
µ-	Micro-
m	Meter
m-	Milli-
Ma	Absolute time in millions of years
micro	Microcline
MN	Magerøy Nappe
musc	Muscovite
myr	Myrmekite
m.y.	Interval time in millions of years
n-	Nano-
OGZ	Oscillatory growth zone
p-	Pico-

Pb	Lead
perth	Perthite
plag	Plagioclase
ppm	Parts per million
Pr	Praseodymium
qtz	Quartz
REE	Rare earth element
SEM	Scanning electron microscope *or* Secondary electron multiplier
ser	Sericite
SIP	Seiland Igneous Province
SS	Sørøy Succession
Th	Thorium
Ti	Titanium
ttn	Titanite
U	Uranium
V	Volt
Zr	Zirconium
zrc	Zircon

1. Introduction

The current constitution of nappes in parts of Scandinavia (Norway and Sweden) is a direct consequence of collisions related to the Scandinavian Caledonian Orogeny, which thrust these units onto the Baltic shield during the early Palæozoic. This series of events involved collisions between Baltica, Laurentia and Avalonia, ultimately creating the superterrane 'Laurussia' just prior to the construction of Pangæa (Torsvik & Cocks, 2003 & 2004; figure 1.1). It also culminated in the closure of the Iapetus Ocean between Laurentia and Baltica that had opened after the break-up of Rodinia in the Neoproterozoic (Torsvik & Cocks, 2003).

Previous models for the evolution of the Scandinavian Caledonides assigned most of the polyphasal deformation and metamorphism observed in the Caledonian nappes to four stages, from c. 550-410 Ma. These stages affected different parts of Norway, and include the *Finnmarkian*, *Trondheim*, *Taconian* and *Scandian* events (Roberts, 2003 and references therein). The *Finnmarkian* event was the earliest noted Caledonian event in Norway (northern Norway, c. late Cambrian – middle Ordovician; $^{40}Ar/^{30}Ar$ mineral separates, Rice & Frank, 2003; Rb-Sr whole rock, Sturt et al., 1978). Sturt & Roberts (1991) suggested that the *Finnmarkian* was the result of the collision between the Baltoscandian margin and a magmatic arc. The *Trondheim* Event occurred some 25 million years after the *Finnmarkian* (central Norway, early Arenig; U-Pb zircon, Dunning, 1987; Roberts, D. *et al.*, 2002) and is related to oceanward subduction along the Baltoscandian margin and caused the obduction of ophiolites onto Baltica (Roberts, 2003). The *Taconian* event occurred during the mid–late Ordovician (central Norway, U-Pb zircon, Pedersen *et al.*, 1999; Nordgulen *et al.*, 1993) but only affected the lithologies off Laurentia that were later thrust onto Baltica. The last stage of the Norwegian Caledonian orogeny, the *Scandian* event (late Silurian – early Devonian; U-Pb zircon, Corfu *et al.*, 2006; Rb-Sr whole rock, Andersen *et al.*, 1982), relates to the collision of Baltica-Avalonia, Laurentia and the British Isles and is responsible for the current distribution of nappes within Scandinavia (Gee, 1975). However, more recent models for the tectonometamorphic evolution of the Kalak Nappe Complex (KNC), northern Norwegian Scandinavian Caledonides (figure 1.2) indicate a complex polyphasal history that began far earlier than the Caledonian orogeny. The KNC occurs towards the top of the nappe pile thrust onto the Baltic shield and is best exposed in the Finnmark province of northern Norway (figure 1.2). Recent U-Pb zircon SHRIMP and ID-TIMS ages have assigned a *Grenvillian* (1100-900 Ma; Meert & Torsvik, 2003) origin to felsic plutonism crosscutting the earliest

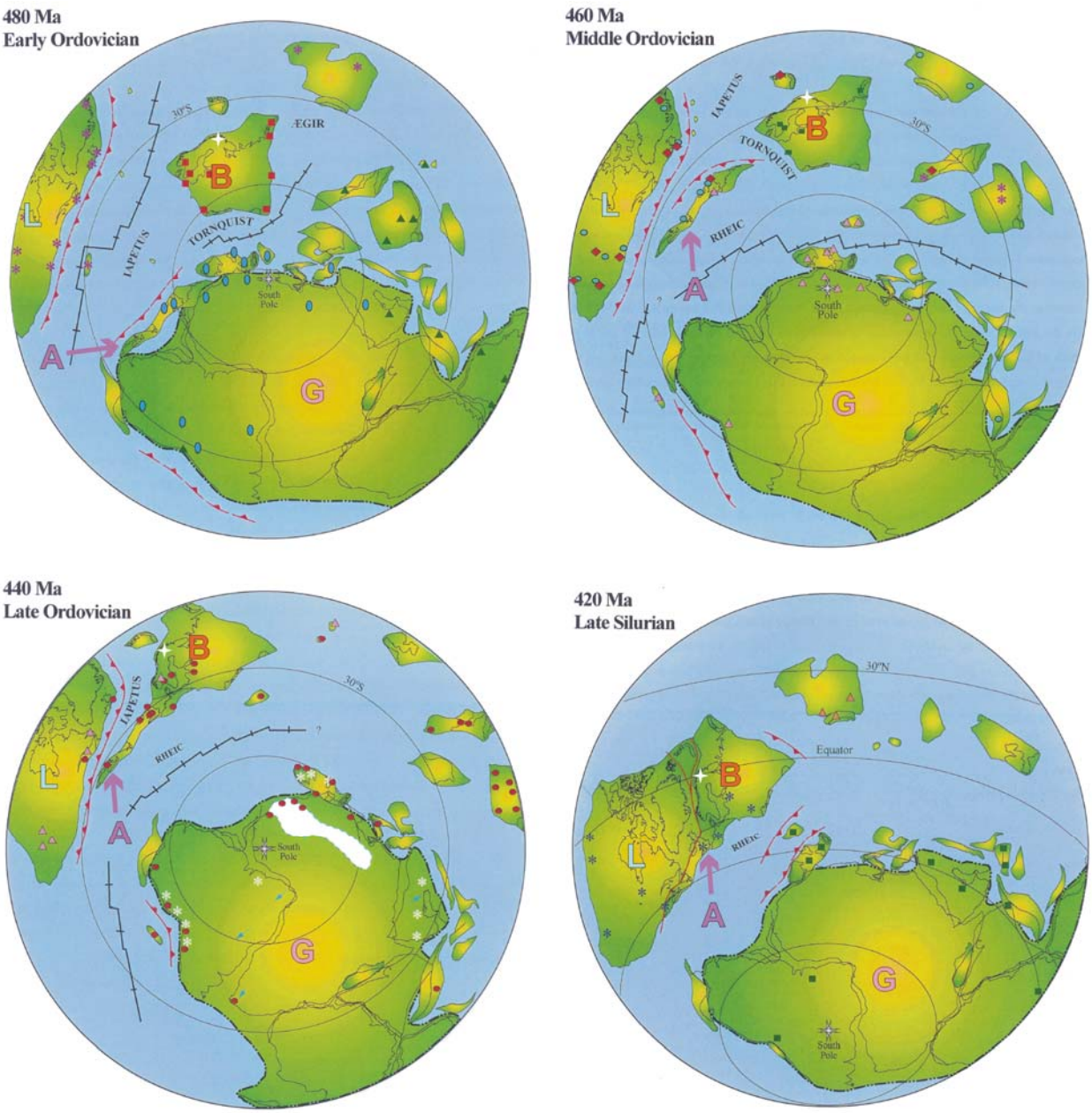


Figure 1.1 Schematic diagrams showing the events leading to the Caledonian Orogeny. *480 Ma* – Post-Rodinia break-up. Rifting has started off the coasts of Gondwana and Laurentia, signalling the closure of the Iapetus Ocean. *460 Ma* – The Iapetus Ocean is steadily closing, following the rifting of the continent Avalonia off of Gondwana, which is moving towards Baltica and Laurentia. Subduction continues off the coasts of Laurentia and Avalonia. *440 Ma* – Avalonia docks with Baltica and signals the start of the Scandinavian Caledonian Orogeny. Continued subduction along Laurentia further closes the Iapetus Ocean. *420 Ma* – Baltica-Avalonia dock with Laurentia, closing the Iapetus Ocean. This represents the main part of the Scandinavian Caledonian Orogeny. *(After Torsvik & Cocks, 2003).* The relative position of northern Norway in Baltica is marked with a white star.

L – Laurentia; B – Baltica; A – Avalonia; G – Gondwana.

deformational fabrics in the lower KNC (Kirkland et al., 2005a; Kirkland et al., in press; Corfu et al., 2005b). This relates the initial evolution of the lower KNC to the amalgamation of the supercontinent Rodinia at c. 1 Ga-1.2 Ga (Meert & Torsvik, 2003). Corfu et al. (in press) suggested that the KNC was largely derived from sediments shed off the margin of either Laurentia or

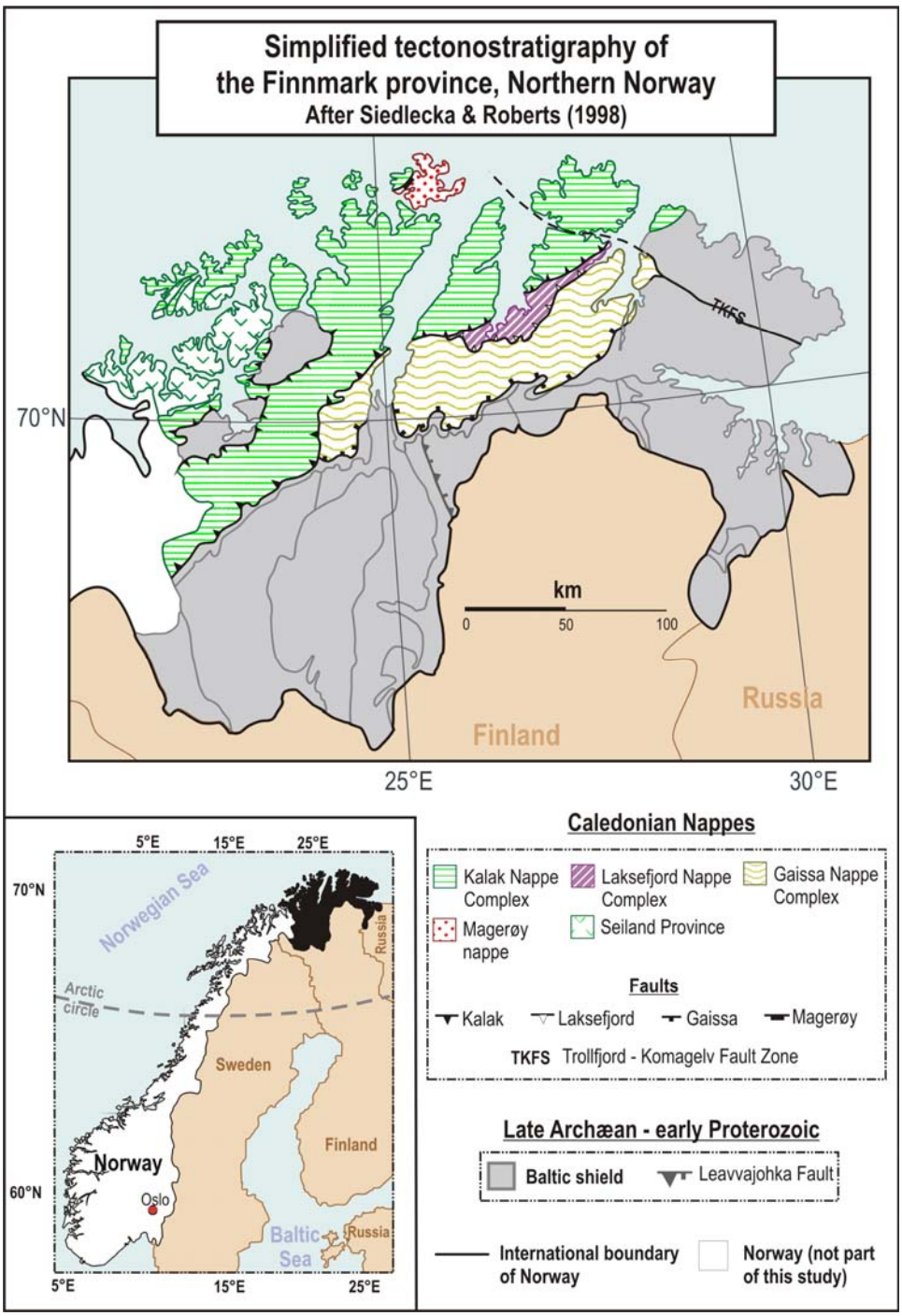


Figure 1.2 Simplified tectonostratigraphy of the Finnmark province, northern Norway. The inset shows the location of the Finnmark province in Norway (coloured in black). The province is composed of late Archæan-early Proterozoic basement gneisses of the Baltic shield and several nappes thrusted during the Caledonian Orogeny. The nappes include (from bottom to top): The Gaissa Nappe Complex, the Laksefjord Nappe Complex, the Kalak Nappe Complex and the Magerøy Nappe. The Kalak Nappe Complex is intruded by voluminous ultramafic-mafic-felsic-alkaline intrusions of the Seiland Igneous Province. *(After Siedlecka & Roberts, 1998).*

Greenland during this orogeny. Three additional tectonometamorphic events followed at c. 850 Ma (*Porsanger*), c. 710 (*Snøfjord*) and c. 440-420 Ma (*Scandian*) (Kirkland et al., in press; Corfu et al., in press). The *Porsanger* and *Snøfjord* events are recorded in the middle KNC and are likewise related to

felsic plutonism and anatexis (Kirkland et al., 2006; Corfu et al., 2005a). The *Porsanger* event has been related to the accretion of volcanic arcs outboard from the Baltic margin (Kirkland et al., in press). The *Scandian* event appears to be the only truly Caledonian orogenic phase recorded in the KNC, resulting from the initial collision of Baltica and Avalonia at c. 443 Ma, followed by their collision with Laurentia at c. 425 Ma (Robin et al., 2005; Cocks et al., 2003; Torsvik et al., 1992). Geochronological evidence for *Scandian* tectonothermal activity is primarily recorded in the Silurian Magerøy Nappe that was thrust over the KNC during this phase (Corfu et al., 2006; Andersen et al., 1982), although some Rb-Sr resetting has been recorded in the KNC (Dallmeyer, 1988). In addition, a period of active mafic-ultramafic-felsic-alkaline plutonism was recorded in the upper KNC at c. 570-560 Ma (R.J. Roberts; in press; R.J. Roberts, et al.; 2004), followed by a period of alkaline plutonism at c. 530-520 Ma (Pedersen et al., 1989). These plutons (collectively known as the Seiland Igneous Province) are suggested to have originated in an intracontinental rift environment (R.J. Roberts et al., in press).

Despite these published data, exact ages for many of the tectonothermal features in the KNC are still lacking. This project forms part of a reconnaissance study aiming to provide precise U-Pb ages for several of these features, with the ultimate aim of aiding in the tectonic re-evaluation of the area. The selected lithologies include mafic and felsic plutons, migmatites and a pegmatite from the KNC, and are all previously undated by U-Pb Isotope Dilution Thermal Ionization Mass Spectrometry (ID-TIMS). Zircon, and occasionally titanite, is dated because the former is more resilient and likely to retain ages of anatexis/intrusion, while the latter is highly reactive and useful for dating post-melting or post-intrusion metamorphic events. ID-TIMS is used in conjunction with petrography and cathodoluminescence (CL) imaging to determine the origin of zircon and titanite (magmatic vs. metamorphic), thereby aiding in a more rigorous interpretation of the U-Pb data.

2. Geology

The KNC consists of up to eight nappes (Gayer et al., 1985; Rice, 1985), which are not necessarily laterally continuous (Zwaan & Roberts, 1978). In addition, the nappes are known by different names in different regions of Finnmark (Zwaan et al., 1975; Roberts, 1974; Ramsay & Sturt, 1976; Daly et al., 1991). The tectonostratigraphic divisions and nomenclature of Daly et al. (1991) are used (figure 2.1) since they cover the same general area as the present study. The nappes of the KNC include the basal Kolvik Nappe, which rests on the major Kalak thrust separating it from the underlying Laksefjord Nappe Complex. The Kolvik Nape is sequentially overlain by the Olderfjord Nappe, Havvatnet Imbricate Stack and finally the Sørøy-Seiland Nappe. The latter is bound at the top by the Magerøy Fault and the overlying Silurian aged Magerøy Nappe.

The constituent nappes of the KNC repeat a tectonostratigraphy of a younger sedimentary cover sequence unconformably overlying Precambrian gneisses (Ramsay & Sturt, 1977). The sedimentary sequence has been correlated between the various nappes of the KNC (Zwaan & Roberts, 1978) and was named for the type locality on the island of Sørøy (figure 2.2) (Ramsay, 1971b). The Sørøy Succession (SS) is thought to represent a conformable sedimentary package from a deepening ocean basin (from bottom to top)(Ramsay, 1971b): Klubben Group quartzites and psammites (shallow water environment), Storelv Group schists and pelites, Falkenes Group marbles and pelites (slightly deeper shelf environment), Åfjord Group pelites and quartzite, and the Hellefjord Group metaturbidite sequence (deeper basin shelf environment) (Ramsay, 1971b; Roberts, 1968, Roberts, 1971; figure 2.1). The Precambrian gneisses underlying the SS include both para- and orthogneisses thought to have been rifted off the Baltic shield (Ramsay & Sturt, 1977). The latter comprises Proterozoic granite, diorite and mafic gneisses (c. 1450-1800 Ma; Siedlecka et al., 2004; Skår, 2002) with variable Riphean-Cambrian sedimentary cover (Zwaan & Roberts, 1978). Various igneous bodies intrude the Klubben and Storelv groups of the Sørøy-Seiland Nappe, the largest of which includes the range of variably deformed ultramafic-mafic-felsic-alkaline plutons of the Seiland Igneous Province (SIP; Robins & Gardner, 1974). Several small felsic and gabbroic bodies also intrude the Hellefjord Group and were assumed to form part of the SIP based on petrographic similarities (Roberts, 1968; Stumpfl & Sturt, 1965). The base of the KNC is characterised by a thick sequence of blastomylonites where it was thrust over the Laksefjord nappe (Sturt et al., 1975).

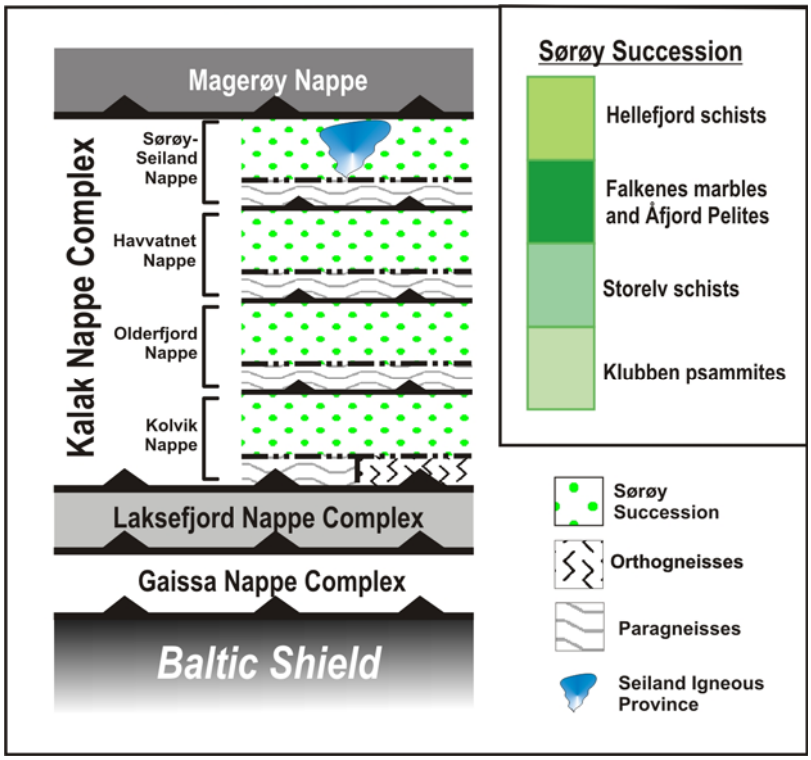


Figure 2.1 Simplified tectonostratigraphy for the Caledonian Nappes of the Finnmark province, which rest on autochthonous Baltic shield. Details for the tectonostratigraphy of the Kalak Nappe Complex are after Daly *et al.* (1991). The inset shows the simplified stratigraphy for the Sørøy Succession *(After Ramsay, 1971b)*.

The Silurian Magerøy Nappe overlies the KNC and was thrust onto Klubben Group psammites of the Sørøy-Seiland Nappe during the early Silurian *Scandian* event (Andersen, 1981; Ramsay & Sturt, 1976). The contact between the two nappes is characterised by strongly flattened and sheared lithologies, including blastomylonites, phyllonites and mylonitised augen gneisses and schists (Ramsay & Sturt, 1976). Away from the sheared contact the Klubben Group has undergone preferential partial melting of its more arkosic members, which gave rise to the Gjesvær Migmatite Complex (Andersen et al., 1982). The migmatites contain two generations of leucosome: the first generation leucosome is conformable with the folded gneissic host, and the second occurs along the hinges of these folds (Ramsay & Sturt, 1976). Andersen (1982) noted that the deformation and anatexis relating to the formation of the Gjesvær Migmatite Complex occurred prior to the emplacement of the Magerøy Nappe and assigned the metamorphism to the *Finnmarkian* event. Rb-Sr ages in the GMC were reset to c. 410 Ma by the *Scandian* orogeny (Andersen et al., 1982).

Deformational features in the KNC are preserved to varying extent. Depending on the locality, anything from two (Akselsen, 1982) to five (Gayer et al., 1985) deformational phases relating to the Scandinavian Caledonian orogeny are preserved, and are usually not traceable over long distances (Townsend, 1987).

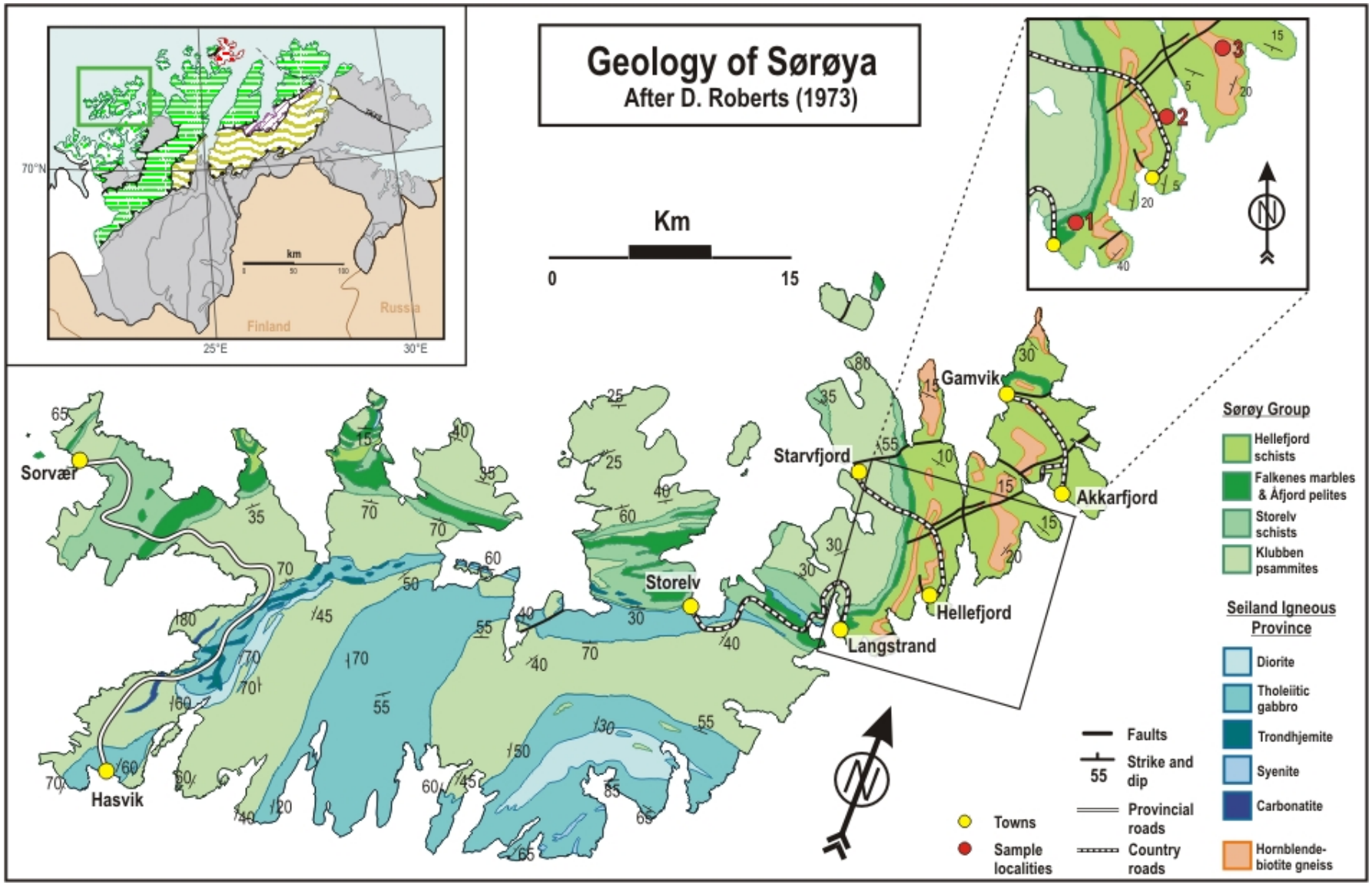


Figure 2.2 Simplified geology of the island of Sørøy, Finnmark province, northern Norway. The inset to the top left shows the location of Sørøy island in Finnmark (highlighted in a green box). The inset to the top right shows the locations of samples 1-3. ***(After Roberts, 1973).***

Relating the deformational phases to specific orogenic events has also proved to be a complex matter. Sturt et al. (1978) related D1 and D2 to early Caledonian activity and D¬3 to the onset of the later *Scandian* event, while Gayer et al. (1985) report evidence from the eastern KNC suggesting that all five deformational phases are solely related to early Caledonian deformation. In contrast, evidence for only two thrusting events is relatively common in the KNC (e.g. Zwaan & Roberts, 1978; Akselsen, 1982). Generally, metamorphic grades increase from the bottom of the nappe pile to the top, from upper greenschist to amphibolite and local granulite facies (Townsend, 1987; Rice, 1985). The initial deformation in the KNC was of a ductile nature and produced large scale, commonly recumbent folding (Ramsay & Sturt, 1975; Zwaan & Roberts, 1978; Gayer et al., 1985) (Sturt et al., 1977; Zwaan & Roberts, 1978; Townsend, 1987). Periods of strong flattening are also associated with this deformation and are locally preserved (Zwaan & Roberts, 1978). This was later followed by brittle deformation (Zwaan & Roberts, 1978; Townsend, 1987; Gayer et al., 1985) involving 'open, upright to moderately flat folds' (Zwaan & Roberts, 1978). Transport directions in the KNC are generally SE and ESE, with a minimum transport distance of 75 km determined from palinspastic reconstructions of the Finnmark Caledonides (Townsend, 1987).

The lithologies described in this study were selected to represent magmatic and anatectic events from the top and bottom of the SS in an attempt to provide a broad overview of tectonometamorphism throughout the succession. Sample locations are shown in figures 2.2 and 2.3. Samples 1-3 were taken from the Hellefjord Group (upper Sørøy-Seiland Nappe), Sørøy Island (figure 2.2). Exposures of the Hellefjord Group are largely restricted to the NE corner of Sørøy, with the exception of a relatively small occurrence along the northern central part of the island (figure 2.2). In the NE sector of Sørøy the Hellefjord Group is only moderately deformed, with dips ranging from 10-30°, and dip direction turning from NW in the south to SW in the north. However, the Hellefjord Group becomes increasingly deformed towards the contact with the underlying Falkenes Group. The three sampled lithologies represent both felsic (sample C04-16 syenogranite augen gneiss; sample NM04-9 migmatised granite gneiss) and mafic (sample NM04-3, metagabbro) magmatic activity. Deformation in the samples is similar to that of the host metasediments, with local evidence for upper amphibolite-granulite facies metamorphism (sample NM04-9). Samples 4-6 were taken from the Gjesvær Migmatite Complex in the Klubben Group (Olderfjord Nappe) on Magerøy Island. Regional dips of the Klubben Group on Magerøy are fairly steep (~50-70°), with dip directions

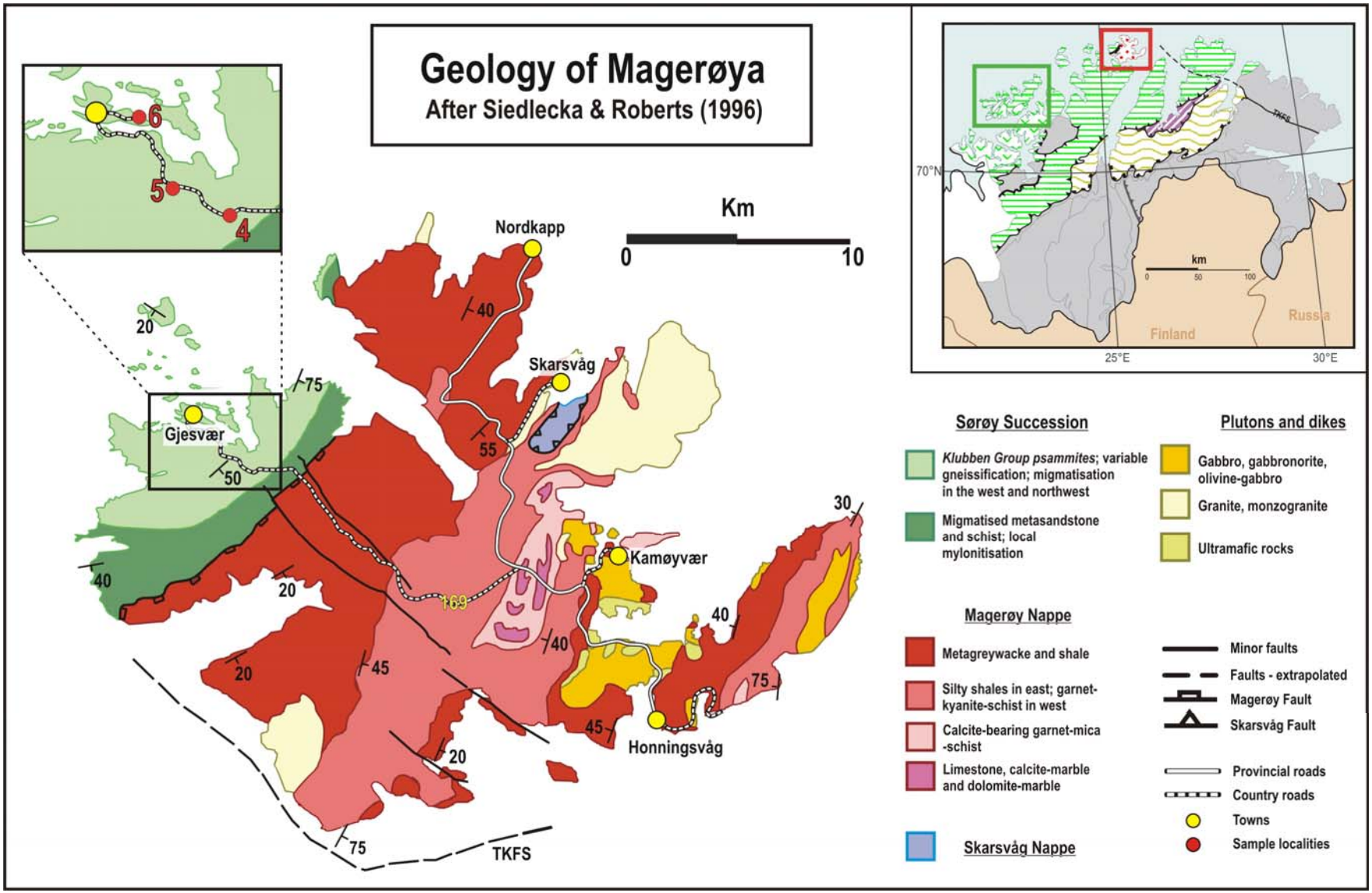


Figure 2.3 Simplified geology of the island of Magerøya, Finnmark province, northern Norway. The inset to the top right shows the location of Magerøya in Finnmark (highlighted in a red box). The inset to the top left shows the locations of samples 4-6. ***(After Siedlecka & Roberts, 1996).***

turning from ESE in the north to SSE in the south. Sample NM04-16 represents the younger of two generations of leucosome in the main body of the Gjesvær Migmatite Complex. On hand specimen scale, the restite and conformable first generation leucosome are affected by tight centimetre-scale isoclinal D1-folds, while the crosscutting second generation leucosome is locally undeformed. Sample C04-2 represents a single leucosome phase conformable to the folded bedding in the Klubben Group and occurs outside and to the SE of the main migmatite body (2 km SE of sample NM04-16). Sample RJR02-58B is a pegmatite that crosscuts the Klubben Group (collected ~2 km SE of C04-2).

3. Methods

Non-magnetic zircons with a euhedral simple prismatic morphology and without any visible inclusions or cores were selected and prepared following the methods of Krogh (1982a, 1982b, 1972). A simple prismatic morphology implies that the crystal is dominated by one of each prism and pyramidal faces (Pupin, 1981; Corfu et al., 2003). U-Pb isotope measurements were done on a Finnigan MAT 262 thermal ionization mass spectrometer. All errors are given to 2σ. CL images were done on a Jeol SEM with CL-detector. A full description of the methods and related theory are given in Appendix C.

4. Sample descriptions

Visually estimated modes for all samples are given in Appendix A.

4.1. C04-16 (Garnet-hornblende syenogranite augen gneiss) – Sørøy Island

Foliated, black, white and pink, porphyroblastic (≤0.5-10 mm) garnet-hornblende-syenogranite augen gneiss. The gneiss was sampled approximately 1 km E of Langvatn, Sørøy Island, by Prof. F. Corfu (no GPS coordinates available). The gneiss is foliated and dip directions change abruptly from NW-dipping in the western part to S-dipping in the eastern part of the body. It is currently unclear whether this change in dip-direction is due to faulting or folding. The foliation observed in the gneiss is parallel to foliation in the host Hellefjord Group. The contact with the Hellefjord schists is sharp, supporting an intrusive nature (F. Corfu, field notes).

The sample consists of elongate perthite porphyroclasts (7-20 mm) surrounded by a matrix of microcline, plagioclase, quartz, biotite, hornblende, garnet, zircon, myrmekite and minor apatite and oxides (figure 4.1a). Hornblende is porphyroblastic and occurs as slightly elongated clusters 2-4 mm in length associated with biotite laths (figure 4.1b). The foliation is defined by the subparallel alignment of perthite porphyroclasts, hornblende and biotite (figure 4.1a). Garnet porphyroblasts (1-2 mm) are associated with biotite and hornblende and commonly crosscut them (figure 4.1c). Zircon is generally associated with biotite (figure 4.1d, e, g) and occurs as colourless simple euhedral prisms with dominant {100} prism and {101} pyramidal terminations and length:width ratios of either >1:3 or ≤1:3 (figure 4.2). These features are in keeping with the crystallisation of primary zircon from a granitic magma (Corfu et al., 2003; Pupin, 1981; also see Appendix D, section D-1). CL imaging of simple prismatic zircons with length:width >1:3 indicates fairly simple crystallisation histories with no change in crystal morphology (figure 4.3a). Oscillatory growth zones (OGZs) are partially obliterated by recrystallisation textures (figure 4.3a). Euhedral zircon crystals with length:width ratios ≤1:3 occasionally contain cores that are variably rounded (figure 4.3c). Overgrowths around the cores show variations in crystal morphology during their growth, but usually have well preserved OGZs (figure 4.3b, c). A small population of zircon crystals with either complex prismatic or rounded morphologies are also present. Zircon is also occasionally hosted by hornblende (figure 4.1f) and garnet. However, this association is considered to be inherited from biotite that was replaced by hornblende and later garnet. Titanite occurs both as

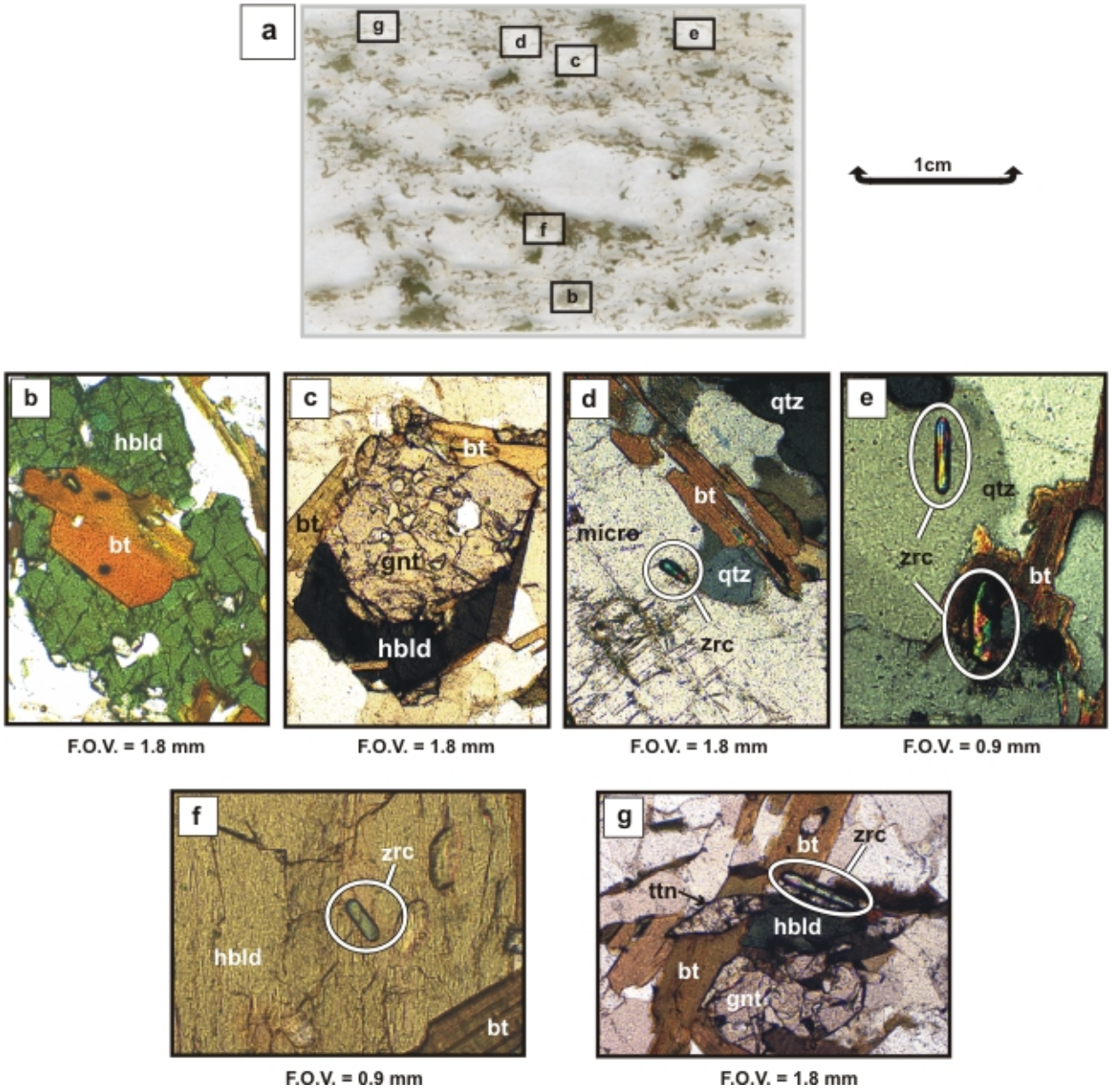


Figure 4.1 Photomicrographs of sample C04-16 (garnet-hornblende syenogranite augen gneiss, Sørøya). ***(a)*** **Mesoscopic characteristics showing the subparallel alignment of K-feldspar porphyroclasts, amphibole and biotite clusters.** ***(b)*** **Hornblende porphyroblast with a biotite inclusion. Hornblende appears to have grown from the breakdown of biotite.** ***(c)*** **Garnet porphyroblast crosscutting both hornblende and biotite.** ***(d, e, f & g)*** **Zircon is observed as inclusions in microcline, quartz, biotite and amphibole.** ***(g)*** **Euhedral titanite occurs as inclusions in biotite, These crystals may be shared with metamorphic hornblende or garnet.**

bt – biotite; gnt – garnet; hbld – hornblende; micro – microcline; myr – myrmekite; perth – perthite; plag – plagioclase; qtz – quartz; ttn – titanite; zrc – zircon.

euhedral-anhedral crystals with light yellow-pale brown colouring (figure 4.1g). Euhedral titanite crystals with a distinct diamond shaped cross section are found as inclusions in biotite and are primary magmatic in origin (Deer, Howie & Zussman, 1992; Corfu & Stone 1998). Subhedral and anhedral titanite crystals occur as inclusions in, or lenticular aggregates of crystals along the edges of hornblende, suggesting a metamorphic origin (Corfu & Stone, 1998). Occasionally a euhedral titanite crystal is shared between an adjacent

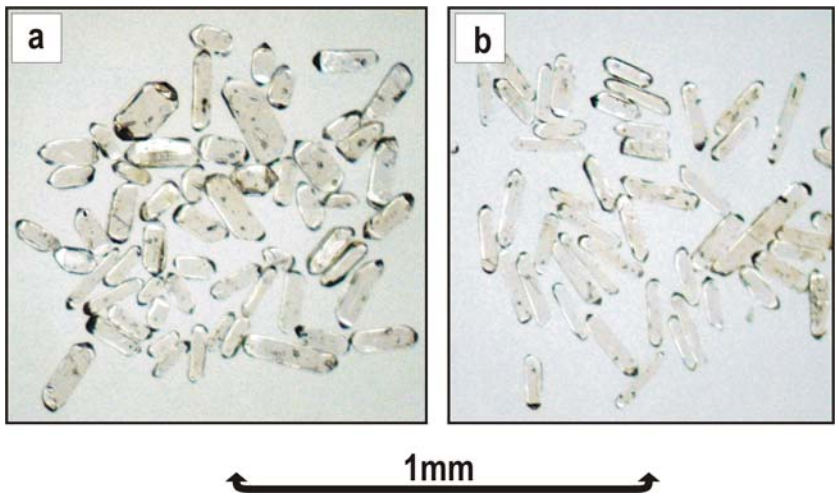


Figure 4.2 Selections of zircons from C04-16 (garnet-hornblende syenogranite augen gneiss, Sørøya). *(a)* Simple prismatic zircons with length: width ratios ≤1:3 and *(b)* simple prismatic zircons with length: width ratios of >1:3. Both zircon populations are fairly uniform in their morphologies, colour and presence of inclusions. However, cores are observed in the shorter prisms.

hornblende and biotite crystal. In such a case the portion of the crystal enclosed by biotite retains a euhedral shape, but is distinctly rounded where it is enclosed by hornblende. Rare examples of metamorphic titanite rosettes occur as inclusions in garnet and hornblende. Magmatic zircon in the granite could provide an age for the initial intrusion, while metamorphism in the gneiss might be constrained by titanite.

4.2 NM04-3 (Metagabbro) – Sørøy Island

Foliated, altered, grey and black, homogeneous, fine-medium grained (≤6 mm) metagabbro. The sample was taken along the road from the town of Hellefjord to Skarvfjord (N70°48'30.2'', E23°18'40.7") by M. Gerber and Prof. F. Corfu. At the sample location the metagabbro has retained most of its igneous texture, although hornblende clusters are partially aligned and elongated creating a N-S foliation dipping 10° W (figure 4.4). The sampled body is one of several metagabbros present in the Hellefjord Group that were originally regarded as sheared and tectonically emplaced equivalents of the Storelv gabbro of the SIP (Roberts, 1968).

The gabbro is composed of hornblende clusters 0.5-5 mm in length (after pyroxene), plagioclase, titanite, rutile and minor zircon (figure 4.5a). Zircon is only observed in mineral separates, and occurs as euhedral simple prisms dominated by {100} prism and {101} pyramidal faces, indicative of crystallisation from a magma (Corfu et al., 2003) (figure 4.6). Zircon is generally of poor quality with surface pitting and common occurrences of

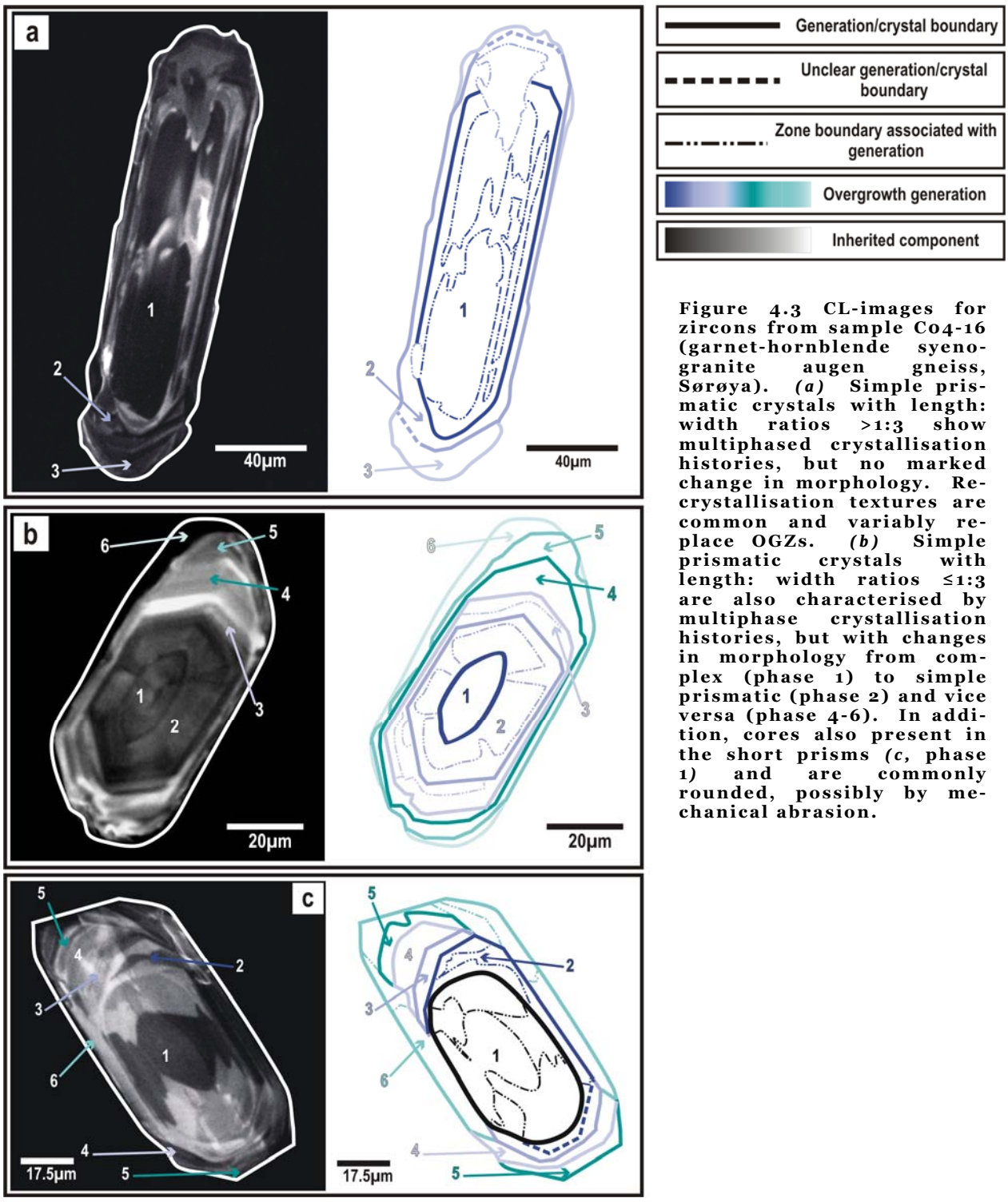


Figure 4.3 CL-images for zircons from sample C04-16 (garnet-hornblende syenogranite augen gneiss, Sørøya). *(a)* Simple prismatic crystals with length: width ratios >1:3 show multiphased crystallisation histories, but no marked change in morphology. Recrystallisation textures are common and variably replace OGZs. *(b)* Simple prismatic crystals with length: width ratios ≤1:3 are also characterised by multiphase crystallisation histories, but with changes in morphology from complex (phase 1) to simple prismatic (phase 2) and vice versa (phase 4-6). In addition, cores also present in the short prisms *(c,* phase 1*)* and are commonly rounded, possibly by mechanical abrasion.

cracks. Titanite is associated with hornblende and occurs as elongate aggregates of subhedral crystals parallel to the foliation (figure 4.5a, b, c). Their association with hornblende and subhedral morphologies are indicative of a metamorphic origin, growing from the breakdown of hornblende (Corfu & Stone, 1998; Frost et al., 2000). Examples are observed of titanite-clusters replacing hornblende crystals to varying extent. The growth of titanite from the metamorphic breakdown of hornblende parallel to the fabric dates both the age



Figure 4.4 Photograph of NM04-3 (metagabbro, Sørøya) (geological hammer-handle for scale), showing the sub-parallel alignment of hornblende clusters. Hornblende (after pyroxene) weathers negatively, giving the rock a pock-marked appearance.

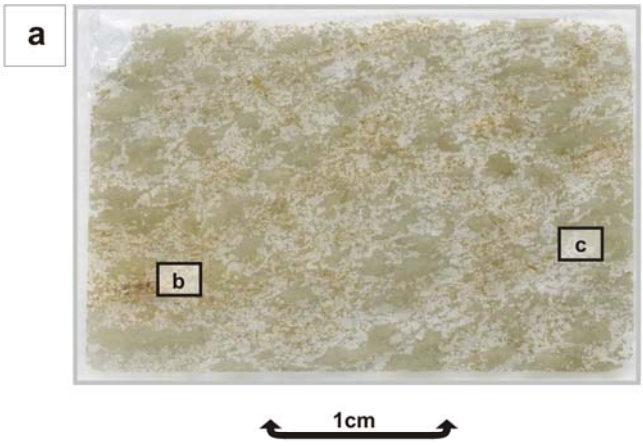


Figure 4.5 Photomicrographs of sample NM04-3 (metagabbro, Sørøya). *(a)* shows the sub-parallel alignment of hornblende clusters. The orange colouring is caused by the presence of metamorphic titanite and rutile from the breakdown of hornblende. *(b & c)* Titanite (indicated in red circles) occurs in clusters of subhedral-anhedral crystals associated with hornblende, commonly with a crosscutting relationship.

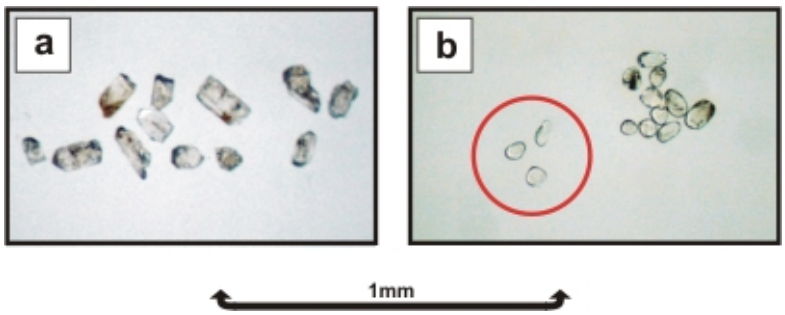


Figure 4.6 Selection of zircons from sample NM04-3 (metagabbro, Sørøya). The crystals have simple euhedral morphologies dominated by {100} prism and {101} pyramidal terminations *(a)*. Their overall quality is poor due to frequent occurrences of inclusions and cracks. A small number of crystals also appear to contain cores. However, abrasion yielded good quality, but small, inclusion-free zircon pieces *(b)* encircled in red.

of metamorphism and deformation. In addition, an age of intrusion can be determined from the magmatic zircon obtained from mineral separates.

4.3 NM04-9 (Migmatised granite gneiss) – Sørøy Island

A folded, foliated, black, white and red, heterogeneous, coarse grained-pegmatitic (2-12 mm) garnet-biotite-migmatised granite gneiss. The sample was taken approximately 2.5 km southwest of the Akkarfjord docks (N70°46'13.5'', E23°20'37.2") by M. Gerber. The degree of gneissosity varies throughout the body from a strongly foliated medium-grained rock (figure 4.7) to a poorly foliated or coarsely crystalline body resembling a granitic intrusion. Isoclinal folding is present on a cm scale with fold hinges running approximately SSW. Where the rock is strongly gneissic, leucosomes (3-20 cm) are coarsely crystalline compared to the host gneiss and parallel to the foliation, sometimes pooling in the fold axes (figure 4.7). In contrast, where the rock is poorly foliated and coarsely crystalline, the leucosomes are short (2-4 cm) and poorly defined. Adjacent to the gneiss the Hellefjord Group appears to have undergone partial melting of its more arkosic layers, but returns to normal sedimentary layering away from the gneiss. The Hellefjord Group locally dips at approximately 4° SSW, with little obvious evidence for deformation.

The granite gneiss consists of microcline, perthite, plagioclase, quartz, biotite, garnet, myrmekite and minor hornblende, zircon and titanite (figure 4.8a). Garnet is porphyroblastic and occurs as elongate grains up 1 cm in length (figure 4.8 a, d). The leucosomes consist of microcline, quartz, myrmekite and minor plagioclase and zircon. The gneissic foliation (where present) is defined by the segregation of subparallel aligned biotite. Zircon in both the gneiss and leucosomes dominantly occurs as colourless euhedral simple prisms with {100}



Figure 4.7 Photograph of NM04-9 (migmatised granite gneiss, Sørøya) (geological hammer for scale), showing a strongly gneissic nature with prominent asymmetrical folds. Well developed anatectic leucosomes occur both parallel to the gneissic foliation *(X)* and as large pools of melt parallel to the fold axis *(Y)*. Garnet porphyroblasts are visible, with larger crystals associated with the leucosomes. Elsewhere this lithology grades into a slightly more massive, coarser grained variety with smaller and less well defined leucosomes.

prism and {101} pyramidal faces, indicating a magmatic origin (Corfu et al., 2003) (figure 4.9). In the gneiss, zircon is hosted by biotite (euhedral-subhedral, length:width up to 1:4) (figure 4.8b), whereas in the leucosome zircon is found in either microcline or plagioclase (euhedral, length:width >1:4) (figure 4.8e). CL images of euhedral simple prismatic zircon indicate cores in simple prisms with length:width ratios ≤1:4, but none in crystals with ratios >1:4 (figure 4.10). Cores occasionally retain primary OGZs and are characteristically bordered by a CL-bright rim (figure 4.10a). Prisms with length:width ratios of >1:4 show evidence for continuous growth histories with no change in crystal morphology (figure 4.10). In addition, recrystallisation textures are also observed that partially or wholly replace OGZs. Titanite in the gneiss occurs as euhedral-subhedral crystals associated with biotite (figure 4.8b), as well as occasional metamorphic titanite rosettes in garnet (figure 4.8c). Since magmatic zircon is observed in both the leucosomes and the gneiss, it is possible to obtain ages for both the initial intrusion of the granite and subsequent anatexis. Furthermore, the apparent synchronicity between anatexis and deformation implies that ages obtained for anatexis will date both the metamorphism and deformation.

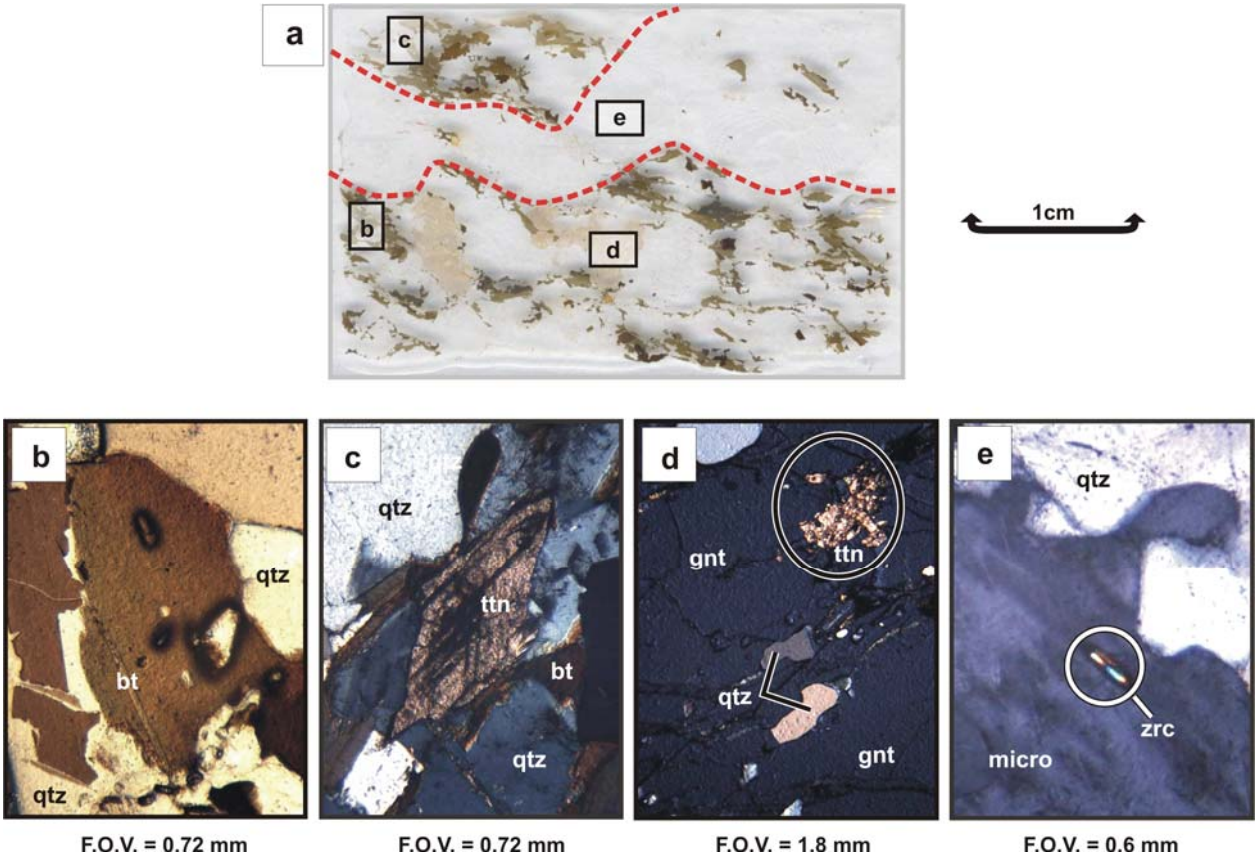


Figure 4.8 Photomicrographs of sample NM04-9 (migmatised granite gneiss, Sørøya). *(a)* The leucosomes are characterised by a smaller proportion of mafic minerals (e.g. biotite, titanite, garnet) compared to the restite. *(b)* Zircon and titanite in the gneiss occur as inclusions in biotite, and are easily distinguishable by black pleochroic haloes. *(c)* Both primary euhedral and metamorphic titanite are present in the sample. *(d)* Occasionally, metamorphic titanite occurs as titanite rossettes in porphyroblastic garnet. *(d)* Zircon in the leucosomes occur only as inclusions in plagioclase and microcline with length: width ratios >1:3.

bt – biotite; gnt – garnet; micro – microcline; myr – myrmekite; plag – plagioclase; qtz – quartz; ttn – titanite; zrc – zircon.

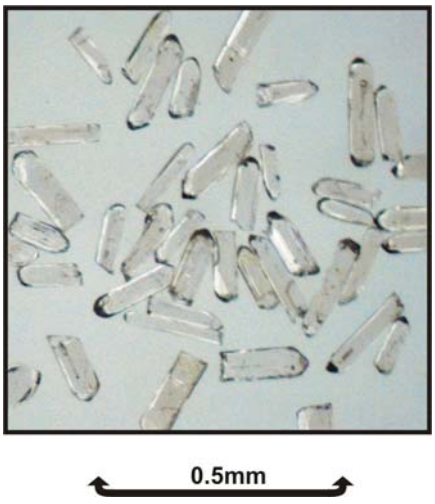


Figure 4.9 Selection of zircons from NM04-9 (migmatised granite gneiss, Sørøya). The zircons are dominated by the {100} prism and {101} pyramidal terminations. Cores are only observed in crystals with a length: width ratio ≤1:3. Besides this, the zircons are generally uniform in morphology and colour.

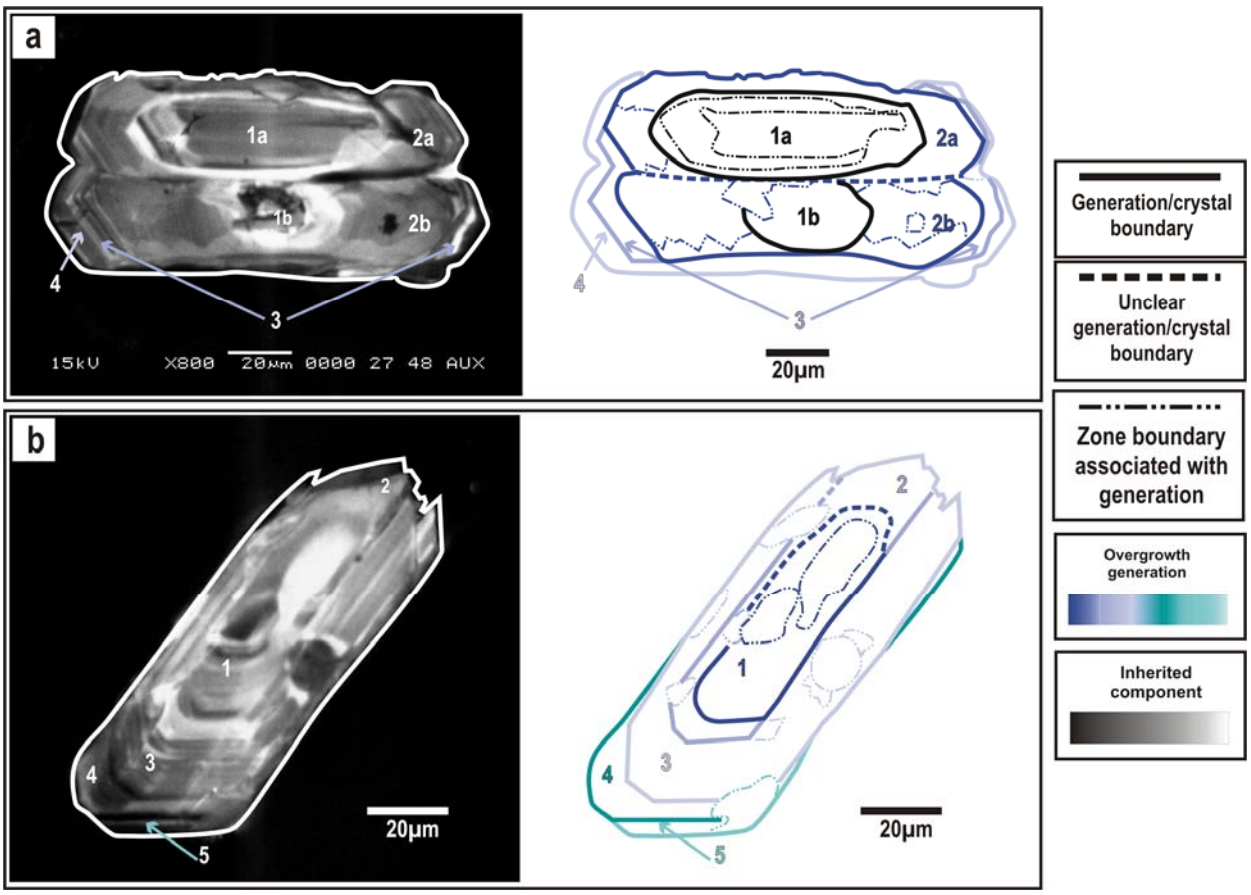


Figure 4.10 CL images for zircons from sample NM04-9 (migmatised granite gneiss, Sørøya). *(a)* Euhedral simple prisms with length: width ratios ≤1:4 commonly contain cores. Some of the cores appear to be magmatically rounded (phase 1a), while others resemble complex prisms (phase 1b). OGZs are well preserved in some cores (phase 1a) and suggest that they were originally simple prismatic. Overgrowths are simple prismatic with development of both {101} and {211} pyramidal terminations (phases 2a and b), although this changes to {101} dominant (phases 3 and 4). Overgrowths may show sector zoning. *(b)* In contrast, simple prisms with length: width ratios >1:4 do not contain cores and indicate continuous multiphased growth histories dominated by {100} prism and {101} pyramidal terminations. Recrystallisation textures are present and partially obliterate OGZs. Many crystals are bordered by a broken CL-bright rim (e.g. *a*, phase 4).

4.4 RJR02-58B (Granodiorite pegmatite) – Magerøy Island

Pink and white, granodiorite pegmatite. The pegmatite outcrops along road no. 169, approximately 4 km SE of the town of Gjesvær (N71°04'40.6'', E25°27'31.6"). The pegmatite is ~4 m wide and intrudes the Klubben Group psammites at a shallow angle relative to the relict sedimentary bedding. Visible disruption and folding of the sedimentary layering occurs at the contact with the pegmatite and continues for ~2 m outwards from the contact after which the metasediments resume a fairly undeformed appearance (figure 4.11a). Variably melted xenoliths are entrained in the pegmatite and are correlated with the adjacent Klubben Group (figure 4.11b).

The pegmatite is composed of plagioclase, microcline, quartz, muscovite and minor biotite and zircon (figure 4.12a). Zircon occurs dominantly as euhedral

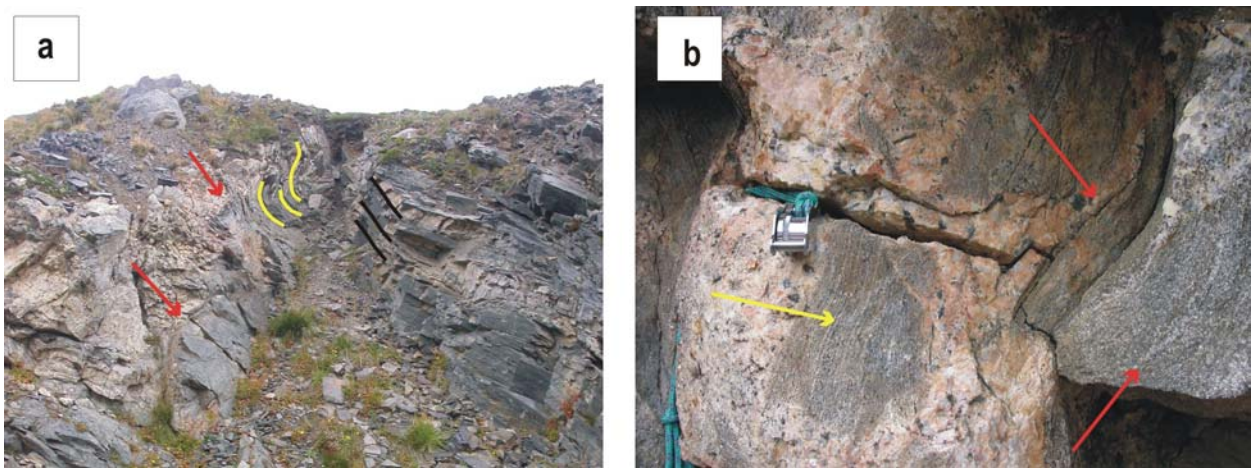


Figure 4.11 Field photos of sample RJR02-58B (granodiorite pegmatite, Magerøya) Picture *(a)* shows the contact of the pegmatite with the host metapsammites of the Klubben Group (red arrows). Just to the right of the contact the bedding of the metapsammites are disrupted and folded upwards (yellow lines). Within two meters away from the contact the bedding of the metapsammites have returned to normal (black lines). *(b)* Close-up of the contact. The psammites adjacent to the pegmatite (red arrows) are folded and bound by a sharp contact with the pegmatite. In addition, pieces of psammite are included in the pegmatite (yellow arrow) and are melted to various degrees. Hand lens for scale.

complex prismatic or partially rounded crystals in muscovite and plagioclase (figure 4.12b, c, d), and rarely biotite (figure 4.12e). These zircon crystals are dominated by {100} prism and {101} pyramidal terminations, typical for zircons crystallising from a pegmatitic melt (Corfu et al., 2003) (figure 4.13). However, in the heavy mineral separates, these simple prismatic features are restricted to light-dark brown overgrowths on complex prismatic crystals. Nevertheless, based on the similarities in morphologies between the simple prismatic crystals and the overgrowths, it is argued that they represent that same phase of zircon growth and will yield an age on intrusion.

4.5 C04-2 (Granitic leucosome) – Magerøy Island

Folded, white and pink, coarse grained (1-10 mm) granitic leucosome, hosted by a foliated, black and white, medium-coarse grained (0.5-2mm) garnet-biotite-gneiss. The sample was collected by Prof. F. Corfu approximately 2 km S of the town of Gjesvær along road no. 169 (N71°05´13.3", E25°24'48.7"). The leucosome occurs as a 'discrete vein, 1-5 cm wide', controlled by the 'steep, westward striking gneissosity of the host'. Tight cm scale isoclinal folds affect both the leucosome and the host gneiss. (F. Corfu, field notes).

The leucosome is composed of plagioclase, microcline, quartz and minor biotite, muscovite and zircon (figure 4.14a). Zircon is hosted in muscovite (figure 4.14b) and occurs as colourless euhedral simple prismatic crystals dominated by {100} prism and {101} pyramidal faces, typical for crystallisation of zircon from

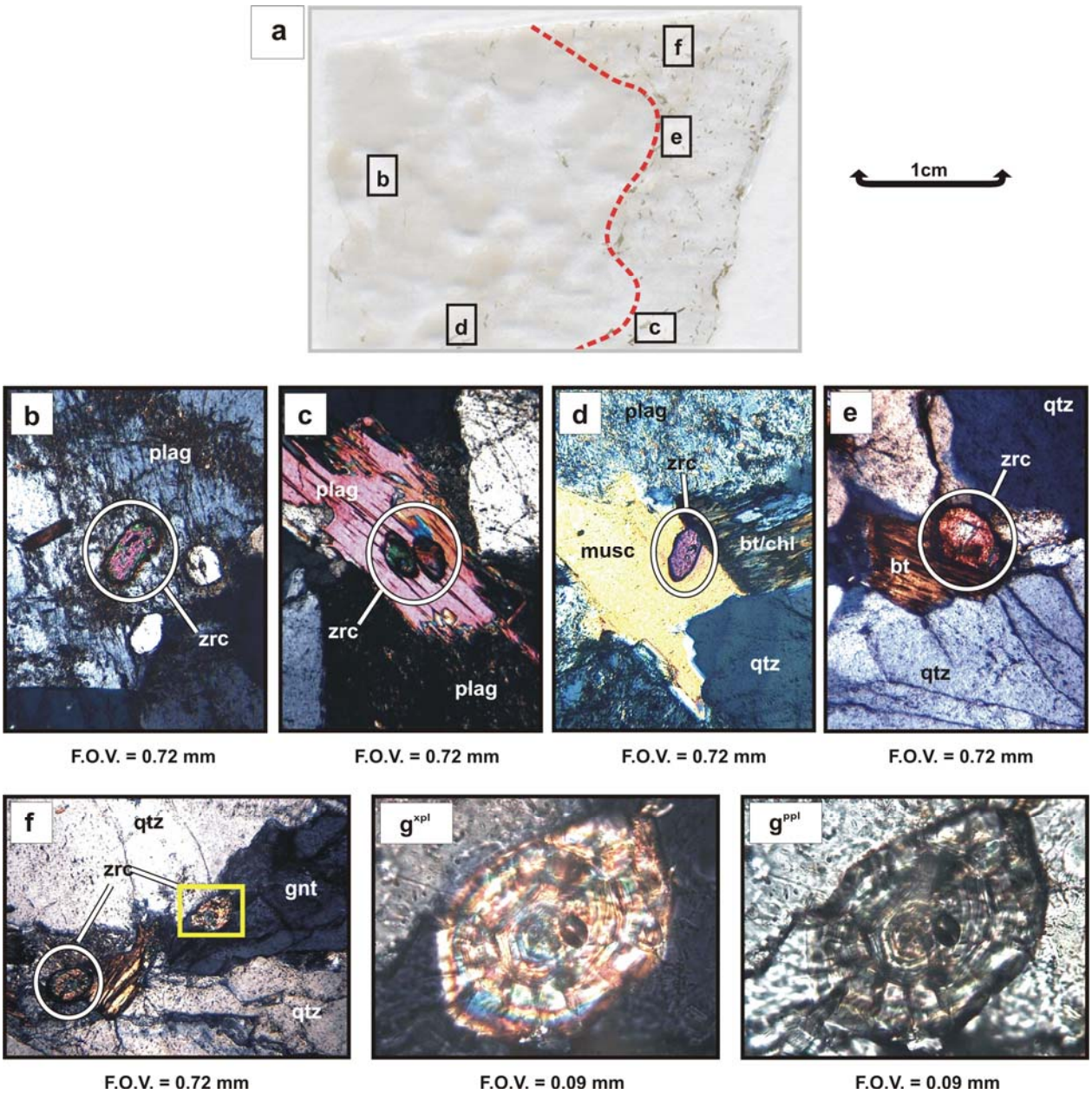


Figure 4.12 Photomicrographs for sample RJR02-58B (granodiorite pegmatite, Magerøya). Zircon commonly occurs as inclusions in highly sericitized plagioclase *(a)* and muscovite *(c & d)*. Crystal morphologies vary from variably rounded simple prismatic *(b)* to variably rounded complex prisms *(c)*. Rare occurrences are observed of complex prismatic zircon hosted by biotite *(e)* and small veins *(f)* in association with garnet, biotite and quartz. Cores and occasionally OGZs (*g*) are visible. All zircons have length: width ratio <1:3.

bt – biotite; chl – chlorite; gnt – garnet; musc – muscovite; plag – plagioclase; qtz – quartz; ser – sericite; zrc – zircon.

a granitic melt (Corfu et al., 2003) (figure 4.15). The zircon prisms are dominated by length:width ratios of ≤1:3, although a small population with ratios >1:3 also occurs. CL imaging revealed the common presence of cores in zircons with length:width ratios ≤1:3, with overgrowths that show a gradual change from a complex prismatic to simple prismatic morphology (figure 4.16a). The cores are variably rounded and commonly show recrystallisation textures. All cores are bordered by a CL-bright rim. In contrast, simple prisms with

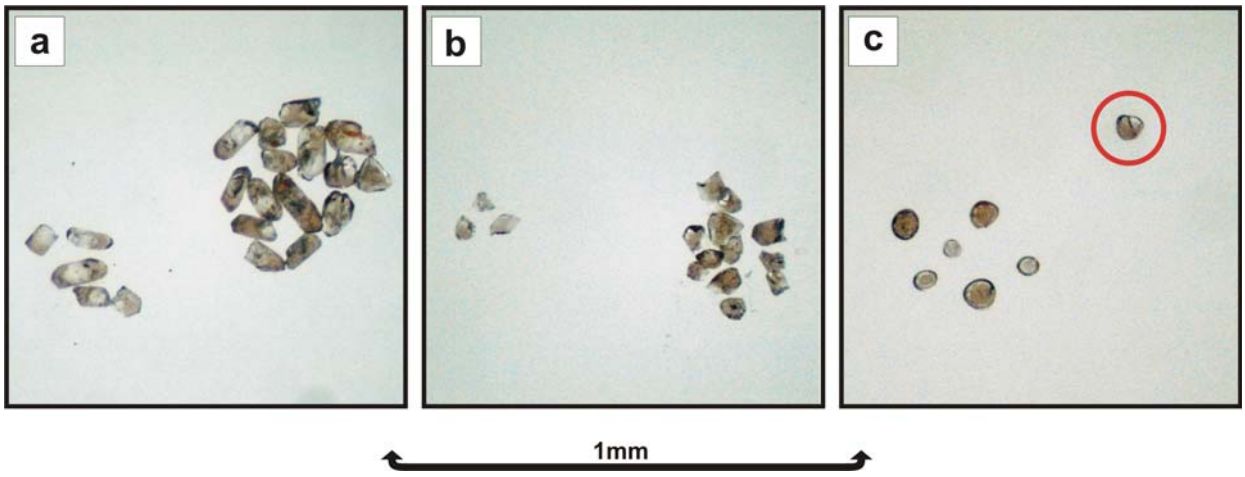


Figure 4.13 Selection of zircons from sample RJR02-58B (granodiorite pegmatite, Magerøya). *(a)* Overgrowths with a simple prismatic morphology are easily distinguished from the complex prismatic core through colour differences. The overgrowths are also notably free of inclusions, compared to the cores. *(b)* The cores were easily removed using a pair of blunt tweezers, leaving high quality overgrowths with no or little traces of core. *(c)* Abrasion of the overgrowths yielded high quality pieces, with the exception of the encircled grain that still contained a piece of visible core.

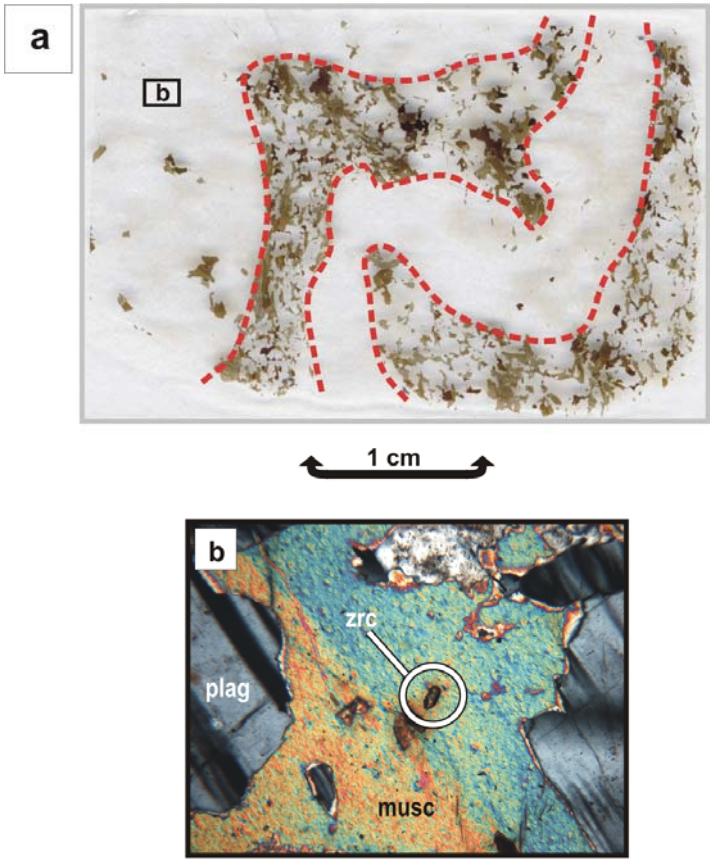


Figure 4.14 Photomicrographs for sample C04-2 (granitic leucosome, Magerøya). *(a)* The leucosome and host gneiss have been deformed, producing tight isoclinal folds. *(b)* An example of zircon hosted by muscovite in the leucosome. The zircon appears to have a simple prismatic morphology.

ap – apatite; bt – biotite; micro – microcline; musc – muscovite; myr – myrmekite; plag – plagioclase; qtz – quartz; ser – sericite; ttn – titanite; zrc – zircon.

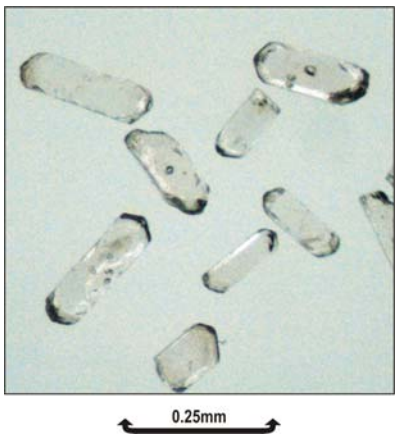


Figure 4.15 Selection of zircons from sample C04-2 (granitic leucosome, Magerøya). The zircons have a simple prismatic morphology dominated by {100} prismatic and {101} pyramidal faces. In general the crystals are homogeneous in colour and fluid inclusions are commonly observed.

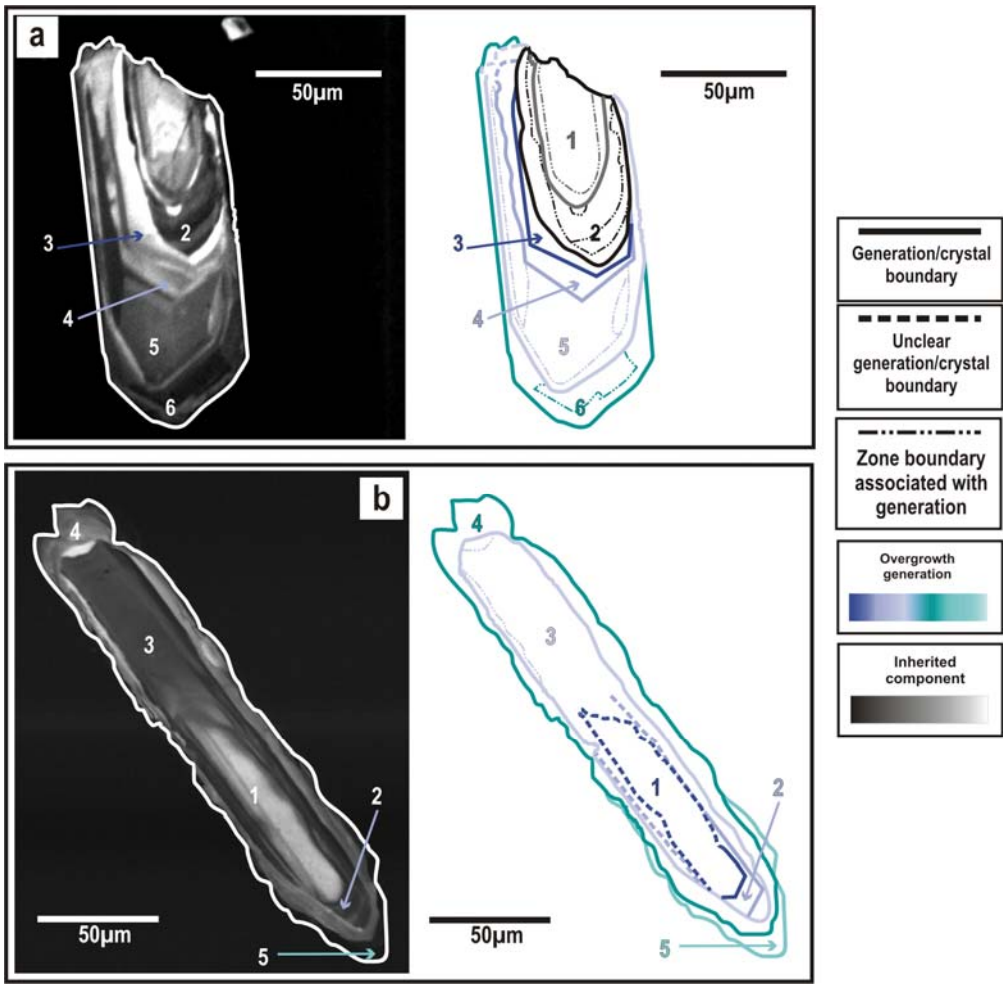


Figure 4.16 CL images for zircons from sample C04-2 (granitic leucosome, Magerøya). *(a)* Simple prisms with length: ratios ≤1:3 commonly contain cores (phase 1 and 2) with complex growth histories, In this particular case, the core is a double inheritance since two components are present. The cores are variably recrystallised and magmatically rounded, and very seldom retain OGZs. Additionally the cores are marked by a CL-bright rim. Overgrowths occur as both simple and complex prismatic. This example shows an overgrowth (phases 3-6) that changes from {100} prism and {101} pyramidal dominated (phase 3 and 4) to slightly {211} pyramidal dominated (phase 5) and back again (phase 6). *(b)* Simple prisms with length: width ratios >1:3 show no obvious signs for inheritance, although recrystallisation features are commonly observed, partially obscuring original relationships. Occasionally OGZs and original phase boundaries are still visible (phase 2), and may show signs of magmatic resorption (phase 3. In general, the prisms are bound by a CL-dark phase (*a*, phase 6 and *b*, phase 5).

length:width ratios >1:3 show no evidence for inheritance (figure 4.16b). Recrystallisation textures are observed in all zircon morphologies. The presence of magmatic zircon in the leucosome dates the migmatisation event.

4.6 NM04-16 (Syenogranitic leucosome) – Magerøy Island

Folded, foliated, black, white and red, medium-coarse grained (1-5 mm) migmatitic garnet-biotite-gneiss hosting two generations of folded, white, medium-coarse grained (2-5 mm) syenogranitic leucosomes. The sample was collected from the Gjesvær docks by M. Gerber (N71°05'51.6'', E25°24'09.1"). The first generation leucosome is parallel to the foliation of the host gneiss (figure 4.17) and both are affected by a D1 folding event (Andersen et al., 1982). The second generation leucosome is parallel to the D1-fold axis and crosscuts both the gneissic foliation and the first generation leucosome. Folding occurs on a centimetre scale and is asymmetrical. For the purposes of this study, the second generation leucosome was isolated for U-Pb geochronology in order to date the youngest melt producing event that affected the Gjesvær Migmatite Complex.

The leucosome consists of microcline, quartz, biotite, plagioclase, muscovite, myrmekite and trace garnet, zircon, titanite and oxides (figure 4.18a). Garnet is porphyroblastic and occurs as 1-2 mm crystals evenly distributed throughout the leucosome and commonly grows at the expense of biotite. Zircon is hosted in biotite and occurs as colourless variably rounded complex prismatic crystals, with few occurrences of colourless simple euhedral crystals (figure 4.18b). The latter are typified by {100} prism and {101} pyramidal terminations, characteristic of crystallisation from a granitic melt (Corfu et al., 2003; Pupin, 1981) (figure 4.19). Length:width ratios of both ≤1:3 and >1:3 are observed in the simple prismatic crystals. CL revealed the presence of cores in crystals with length:width ratios ≤1:3 (figure 4.20a, b). Cores show evidence for resorption indicated by highly irregular but smooth boundaries, and are overgrown by normally zoned magmatic zircon with both simple and complex morphologies. Simple prismatic zircons with length:width ratios >1:3 are characterised by continuous growth phases and do not contain evidence for inheritance (figure 4.20c, d). Recrystallisation textures are observed in all zircon morphologies, which partially or wholly obliterate OGZs. Most of the zircons are bordered by a CL-bright rim, indicating a post-crystallisation disturbance. Zircon is occasionally hosted in porphyroblastic garnet (figure 4.18c). However, this is considered to be an inherited inclusion from biotite replaced by the garnet. Since the second generation leucosome contains magmatic zircon it is possible



Figure 4.17 Photograph of NM04-16 (syenogranitic leucosome, Magerøya) (pencil for scale), showing two generations of anatectic leucosome. The first generation leucosome is parallel to the folded gneissic foliation of the host, while the second generation leucosome is parallel to the fold axis and cross-cuts the gneissic foliation and first generation leucosome.

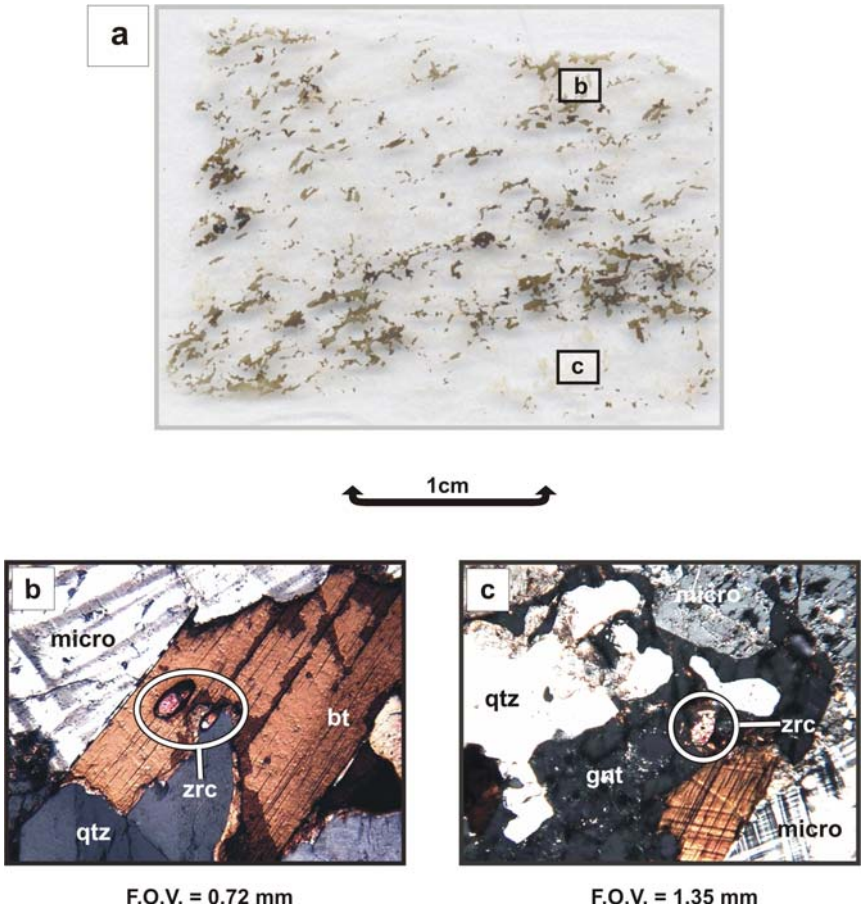


Figure 4.18 Photomicrographs of sample NM04-16 (syenogranitic leucosome, Magerøya). *(b)* Zircon is associated exclusively with biotite, and mostly occurs as variably rounded complex prismatic crystals with few simple prisms. Biotite is occasionally eroded by quartz or garnet *(b and c)*, exposing the zircon inclusions.

bt – biotite; chl – chlorite; gnt – garnet; micro – microcline; musc – muscovite; myr – myrmekite; plag – plagioclase; qtz – quartz; ser – sericite; zrc – zircon.

to date the age of the migmatisation. This will also give a minimum age for the D1-folding and anatexis that is crosscut by the second generation leucosome

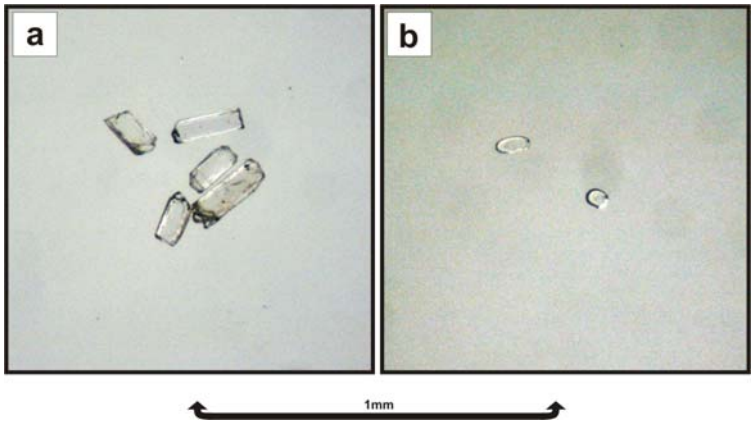


Figure 4.19 Selection of zircons from sample NM04-16 (syenogranitic leucosome, Magerøya). *(a)* Simple prisms (especially those of length: width ratios >1:3) commonly occur as broken pieces with slightly pitted features. *(b)* However, abrasion yielded high quality, but small grains.

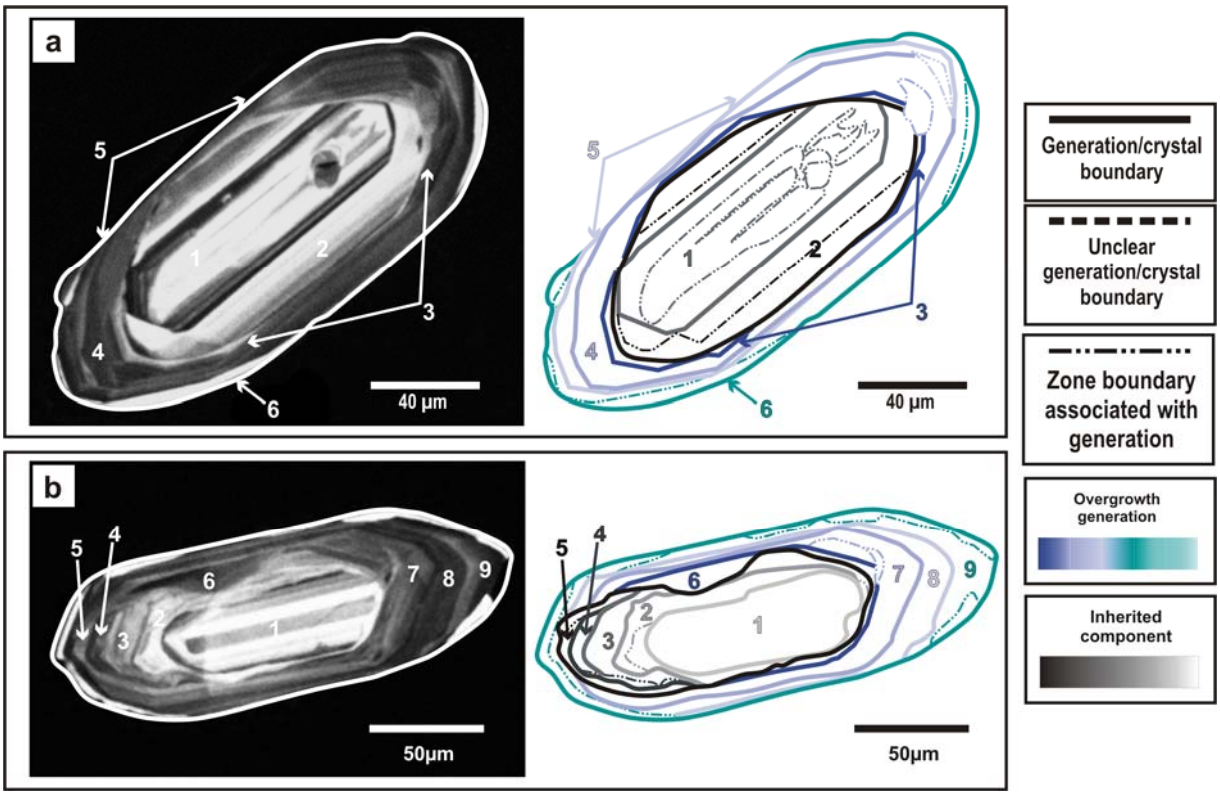


Figure 4.20 CL images for zircons from sample NM04-16 (syenogranitic leucosome, Magerøya). *(a)* Simple euhedral prisms with length: width ratios ≤1:3 commonly contain cores. The cores themselves have complex histories, and may contain their own inherited component (phase 1). Recrystallisation textures are observed in the core that partially obliterates original OGZs. The cores also show signs of magmatic resorption, especially in *(b)*, where the inherited phases 1-5 have an eroded anhedral shape. Growth phases and OGZs are commonly well preserved in the overgrowths, which are always bordered by a CL-bright rim.

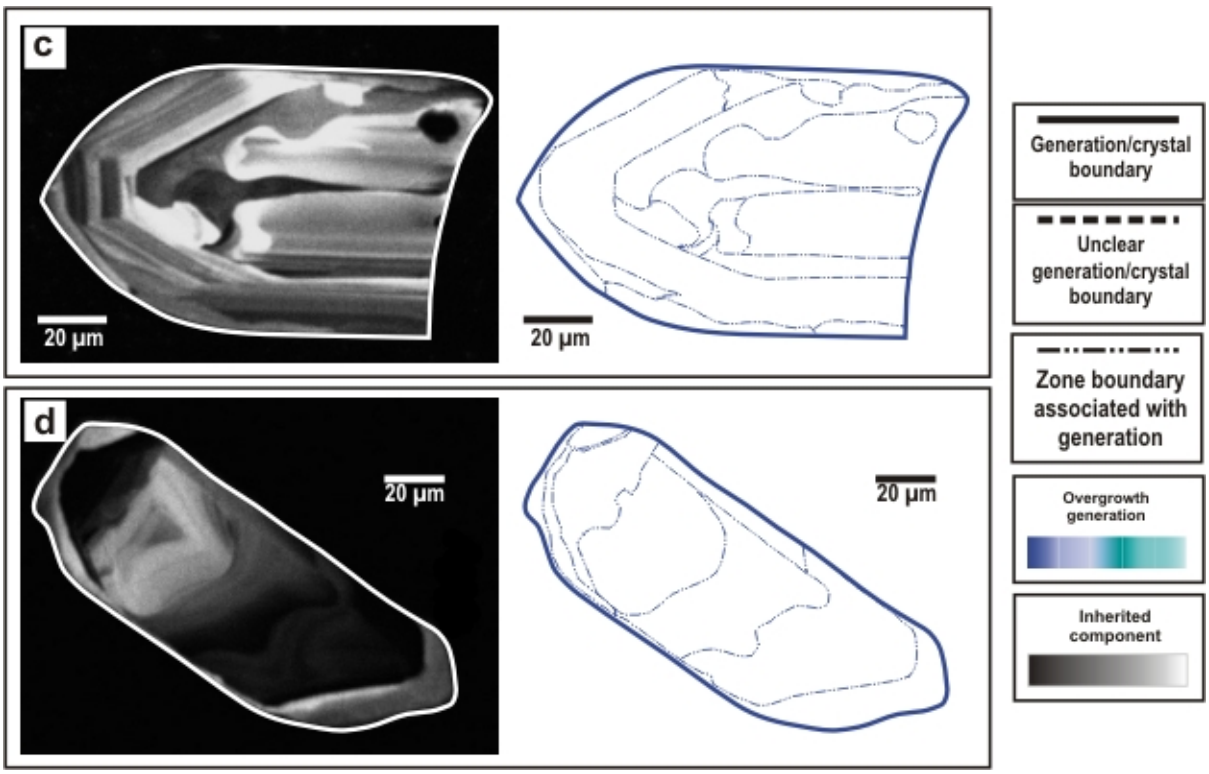


Figure 4.20 CL images for zircons from sample NM04-16, cont. (syenogranitic leucosome, Magerøya). ***(c)*** **Simple prismatic zircons with length:width ratios >1:3 generally show continuous growth histories with no change in crystal morphology. Recrystallisation textures are common and variably obliterate the OGZs. Extreme cases of recrystallisation were also observed** ***(d)*** **where no internal structure remained at all, producing an 'agate-like' pattern.**

5. Results and discussion

All TIMS data are given in Appendix B.

5.1 C04-16 - (Garnet-hornblende syenogranite augen gneiss) – Sørøy Island

5.1.1 TIMS data:

Zircon

Five U-Pb analyses were performed on multicrystal fractions of euhedral tips (fractions 87/6 and 89/51), simple prisms with length:width >1:3 (fractions 87/5 and 89/57) and simple prisms with length:width ≤1:3 (fraction 87/7). Prisms and tips with larger length:width ratios were preferentially selected for analyses since their potential for carrying an inherited component was considered smaller. The data indicate moderate to high U concentrations (200-863 ppm), 206Pb/204Pb values of 452-12,639 and Th/U ratios between 0.33-0.45.

Four of the analyses (87/6, 87/7B, 89/51 and 89/57) are concordant within error, but are spread along the Concordia curve between approximately 433 and 442 Ma (figure 5.1). The fifth point (87/5) is slightly discordant with an older 207Pb/206Pb age of 447 ± 4 Ma. There is no apparent correlation between crystal morphology and discordancy or age.

Titanite

Two fractions of titanite were selected based on colour (pale titanite, fraction 89/S3 and yellow titanite, fraction 89/S4) (figure 5.2). The data indicate very low U content (43 and 62 ppm), Th/U values (0.05 and 0.06) and 206Pb/204Pb ratios (144 and 191) compared to zircons from the same sample. The colour difference is attributed to slightly lower concentrations of Pb and U in the pale titanites.

Both the analyses are concordant within error and yield a Concordia age of 431.4 ± 1.1 Ma, which overlaps with the younger of the zircon data points (figure 5.1). The larger error ellipses for the titanite analyses are due to small concentrations of U and Pb, as well as a large 204Pb component.

5.1.2 Discussion:

Based on the magmatic morphologies of the zircons in sample C04-16, the spread of concordant data over c. 8 m.y. along Concordia is suggested to be a combination of magmatic growth with either a) the presence of an inherited

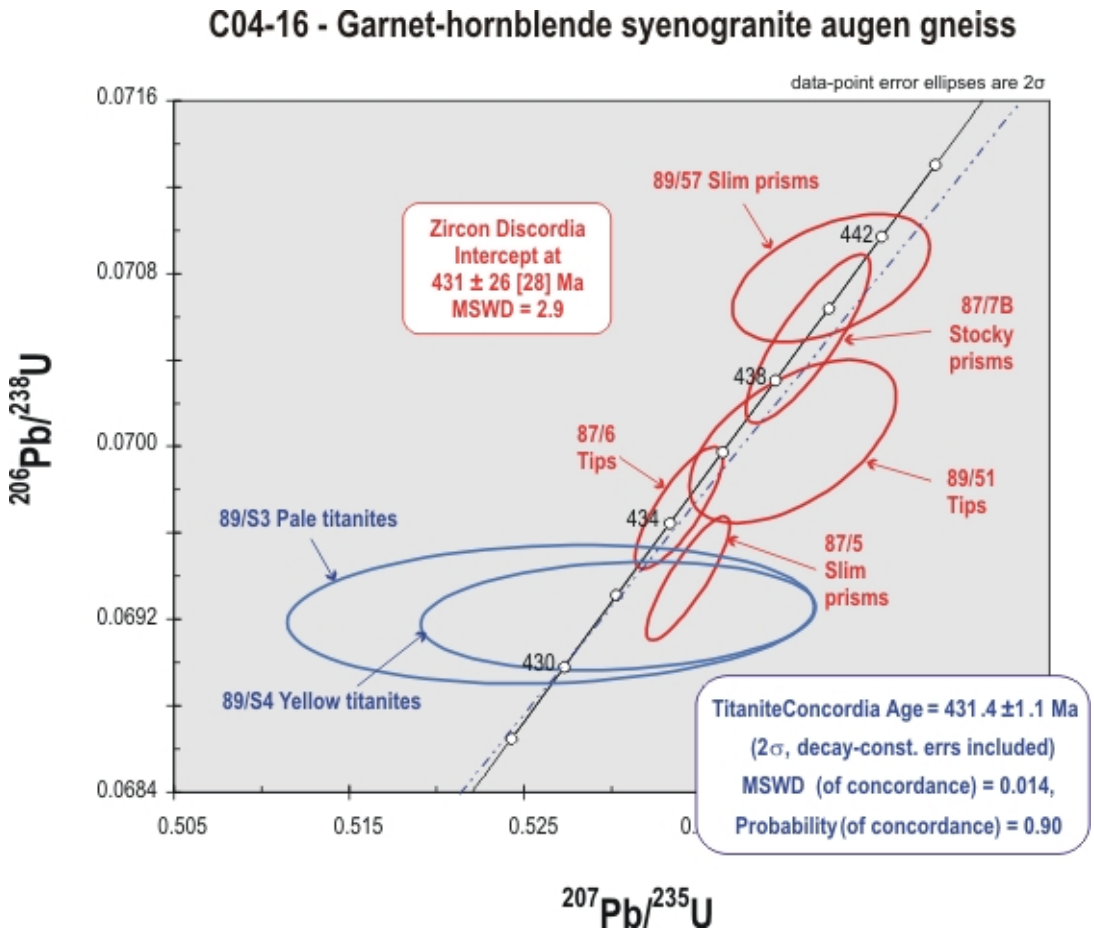


Figure 5.1 Concordia diagrams for sample C04-16 (garnet-hornblende syenogranite augen gneiss, Sørøya), including zircon (red) and titanite (blue) data points. The data points of the individual fractions are shown, indicating no apparent correlation between zircon morphology and the spread of ages. The four concordant data points define a spread of ages of c. 6 m.y from c. 441-435 Ma. The fifth discordant point has an older $^{207}Pb/^{206}Pb$ age of 447 ± 4 Ma. Two fractions of sphene define a Concordia age of 431.44 ±0.97 Ma which marginally overlaps with the lower concordant zircon data point. A discordia line fitted to the data has an imprecise lower intercept of 431 ± 26 Ma. The upper intercept is ignored due to the large error. Due to the minimal evidence for cores, inheritance-effects are assumed to be negligible. However, the abundant evidence for recrystallisation suggests a degree of Pb-loss has occurred. Therefore, the uppermost concordant zircon point is suggested to approximate the age on intrusion at c. 441 Ma, while the lower intercept is the best approximation for a metamorphic event at c. 431 Ma.

component, or b) dispersion through Pb-loss and/or the growth of metamorphic zircon. In the former case the zircons may contain a component inherited from the Hellefjord schists. However, only fraction 87/5 has an older 207Pb/206Pb age of 447 ± 4 Ma that indicates a possible inherited component. In addition, only one example of inheritance was observed under CL (n=17) (figure 4.3). Therefore, while cores may be present, their scarcity implies that they account for only a very small proportion of the total zircon population and are not solely responsible for the spread of data. On the other hand, many crystals show evidence for recrystallisation (e.g. figure 4.1), thereby arguing in favour of Pb-loss. No evidence for metamorphic overgrowths is observed. In this case, the older data point (fraction 89/57) at 440.9 ± 1.5 Ma is suggested to best

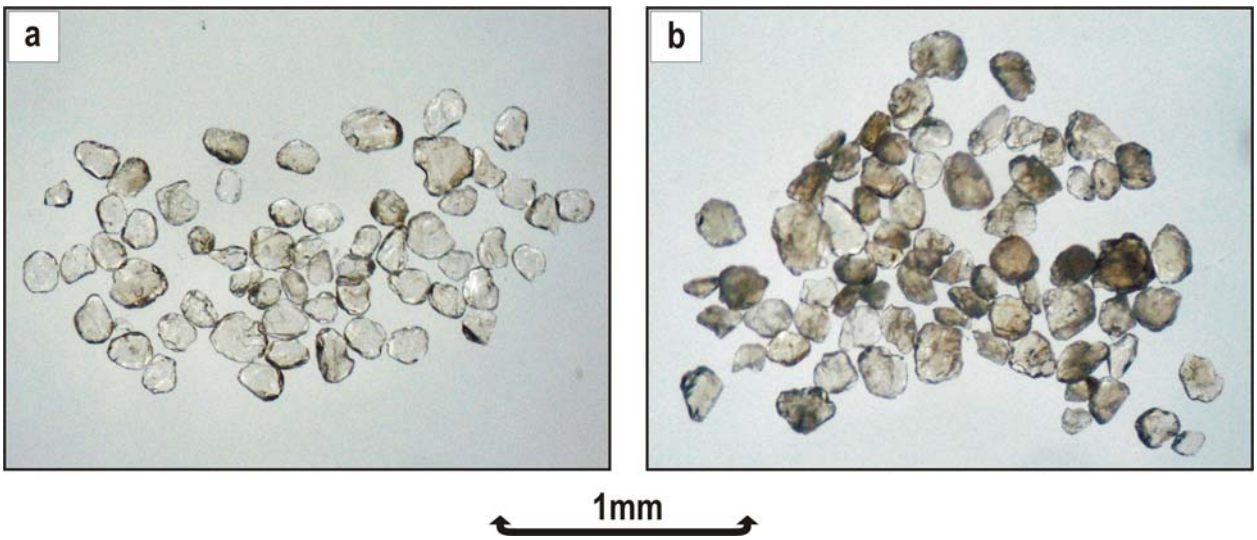


Figure 5.2 Examples of pale *(a)* and dark *(b)* titanite from sample C04-16 (garnet-hornblende syenogranite augen gneiss, Sørøya). A separate fraction each type was selected for analyses. The pale titanites have slightly lower concentrations of Pb and U, which would account for the colour difference.

approximate the age of intrusion, with Pb-loss during a subsequent metamorphic event.

Due to the highly reactive nature of titanite and its ready growth under metamorphic conditions (Scott & St. Onge, 1995), it is likely that both the primary magmatic and later metamorphic crystals in this sample will record the same age. Therefore the 431.4 ± 1.1 Ma Concordia age from titanite fractions 89/S3 and 89/S4 is suggested to date a post-intrusion metamorphic event. These data points overlap with the youngest of the concordant zircon data points (fraction 87/6). It is suggested that the recrystallisation and associated Pb-loss observed in the zircons are related to this c. 430 Ma event.

5.2 NM04-3 (Metagabbro) – Sørøy Island

5.2.1 TIMS data:

Zircon

Due to the general lack and poor quality of zircons in this sample, all crystals that did not contain obvious inclusions or cores were abraded, and the best parts salvaged for analyses. This approach yielded small, but high quality pieces. Four single-crystal analyses were performed, for which data indicate moderate to low U contents (126-240 ppm), high Th/U ratios (1.18-1.41) and 206Pb/204Pb ratios between 160-2,075. The low 206Pb/204Pb ratio and high 204Pb content in fraction 87/11 may be a result of contamination rather than alteration processes, since the high common Pb level is not shared by any of the other grains.

The four analyses define a Concordia age of 436.7 ± 0.8 Ma (MSWD = 1.8; figure 5.3).

Titanite

Three fractions of inclusion-free titanite were analysed (figure 5.4). Data indicate low U contents (18-25 ppm), very high Th/U ratios (2.95-3.90) and 206Pb/204Pb ratios between 65-102.

The three data points define a Concordia age of 427.8 ± 2.7 Ma (MSWD = 1.7) (figure 5.3). Although fraction 117/S7 is similar to fraction 89/S8 in total Pb (4 ppm), total U (18 and 22 ppm, respectively) and common Pb content (~50 and 67 pg, respectively), it has a lower 206Pb/204Pb ratio, suggesting less radiogenic Pb. Such a small concentration of radiogenic Pb (<4 ppm) may have lead to an erroneous measurement of the Pb-isotopic ratios and subsequent larger errors and a younger 207Pb/206Pb age. The Concordia age is therefore suggested to be closer to the c. 428 Ma ages of fractions 89/S8 and 117/S10.

5.2.2 Discussion:

A slight spread (~ 3 m.y.) is observed in the zircon data points, which, based on the generally poor quality of the zircons, is attributed to recent Pb-loss. However, since both the 207Pb/206Pb and U-Pb are within error, the spread is considered negligible. In this case the Concordia age of 436. 73 ± 0.84 Ma is suggested to best approximate the age of crystallisation.

The metamorphic nature of the titanites implies that the c. 428 Ma age dates post-crystallisation metamorphism. This is within error of the c. 430 Ma metamorphic age obtained from sample C04-16, suggesting that both ages relate to the same event. In addition, the growth of titanite in clusters parallel to the foliation suggests that the combined metamorphic age of c. 430 also dates the age of formation of the fabric observed in the gabbro.

5.3 NM04-9 (Migmatised granite gneiss) – Sørøy Island

5.3.1 TIMS data:

Five analyses of zircons were performed on multicrystal fractions of tips (fractions 87/2 and 89/52), broken (fractions 87/4 and 89/56) and whole prisms (fraction 87/3) with length:width >1:4. However, since the distinction between long and short simple prisms is somewhat arbitrary, a small number of simple prisms with length:width ≤1:4 may have been included in the selected

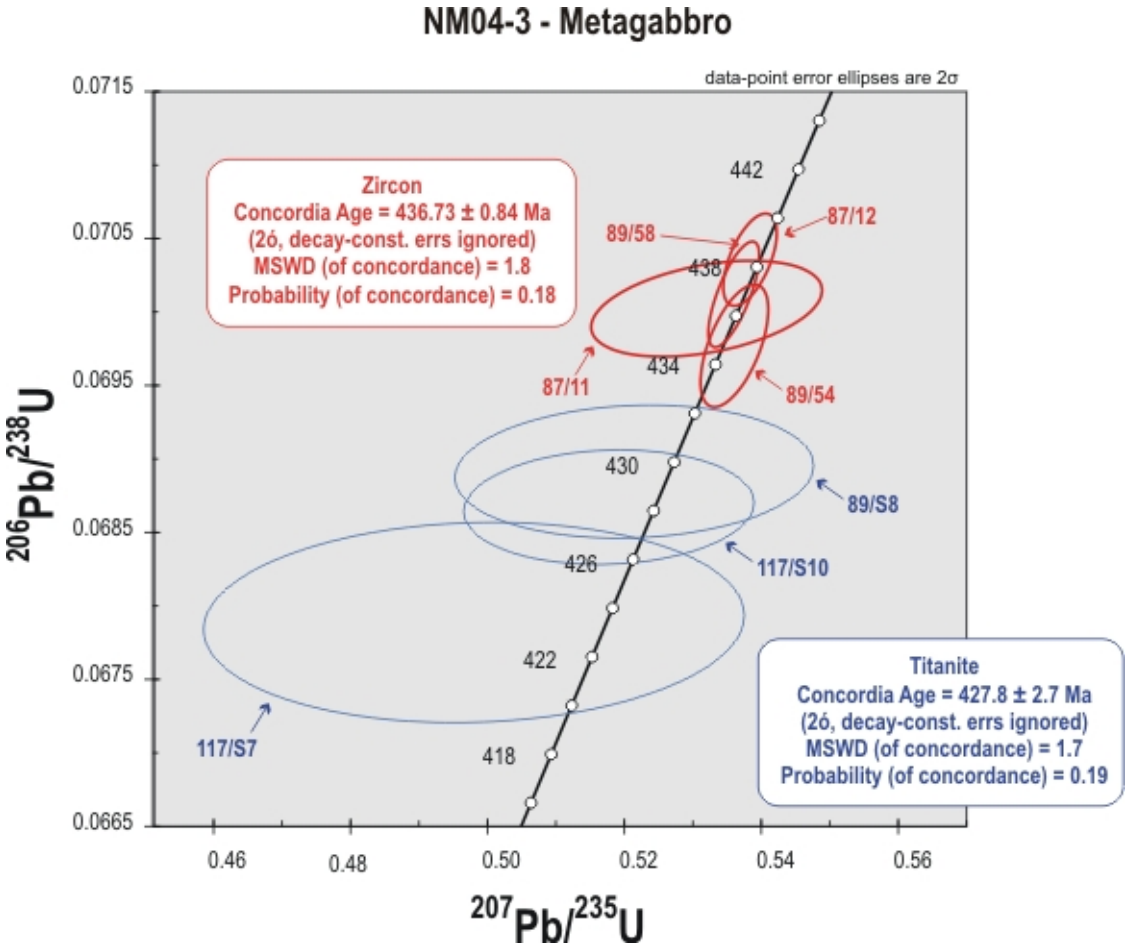


Figure 5.3 Concordia diagrams for NM04-3 (metagabbro, Sørøya). Zircon (red) and titanite (blue) data points define two age populations with a Concordia age of 436.7± 0.8 Ma (MSWD = 1.8) for the zircons and 427.8 ± 2.7 Ma (MSWD = 1.7) for titanite). The larger error in fraction 87/11 appears to be caused by a large amount of common Pb, while in fraction 117/S7 it is a combination of low overall U and Pb and a large common Pb component.

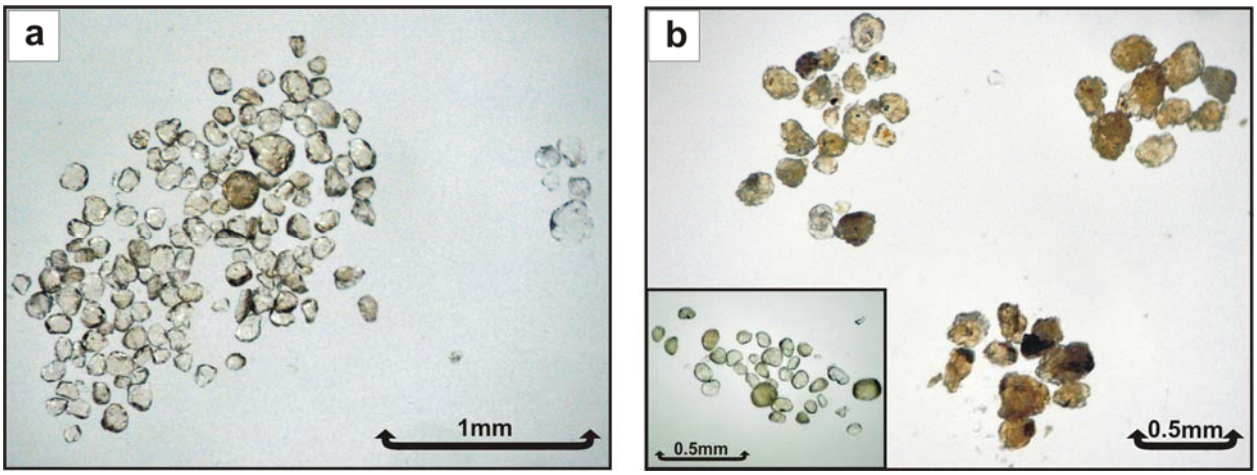


Figure 5.4 Selection of titanite from sample NM04-3 (metagabbro, Sørøya). Two populations are observed – *(a)* pale yellow to colourless grains that are mostly well rounded and *(b)* an orange-yellow angular population composed of composite grains. Inclusions are seldom observed in the pale yellow populations, but are ubiquitous in the orange-yellow grains. After abrasion, however, the composite grains broke down to grains of similar appearance to the pale-yellow grains *(inset)*.

fractions. Preference was given to tips, since they were less likely to contain any inherited component. The data indicate moderate U contents (182-417 ppm), 206Pb/204Pb values between 3195-5765 (with the exception of fraction 89/52 which has a value of 535) and Th/U ratios 0.20-0.33.

Four of the analyses plot concordantly but are spread along the Concordia curve between approximately 436-429 Ma. The fifth point is discordant with an older 207Pb/206Pb age of 464 ± 14 Ma (figure 5.5). A discordia line fitted to the data points yields lower intercept of 432 ± 10 Ma and an imprecise upper intercept of 872 ± 640 Ma (MSWD = 5.6). There is no apparent correlation between crystal morphology and age.

5.3.2 Discussion:

The euhedral magmatic zircon morphologies and evidence for both inheritance and recrystallisation suggest that the poor MSWD of the discordia line could be a mixture between either: a) inheritance + magmatic growth + Pb-loss or b) inheritance + 2 stages of 'magmatic' growth. In the first case, the growth of all the euhedral zircons would be related to the initial intrusion of the granite, possibly at c. 436 Ma. The upper discordant point would then represent the inherited component, while the spread of data below c. 436 Ma is attributed to Pb-loss from a metamorphic event at c. 430 Ma. While this model accounts for the older 207Pb/206Pb age of 464 ± 14 Ma in fraction 89/52 and the evidence of recrystallisation, it does not account for the growth of new zircon in a leucosome assemblage. Since euhedral crystals are observed in both the host gneiss and leucosome in different associations, it suggests that at least two phases of 'magmatic' zircon growth have occurred. Therefore, evidence appears to favour the intrusion of the granitic body at c. 436 followed by an anatectic event at c. 430 Ma, with a minor older component inherited from the Hellefjord Group. The recrystallisation textures observed in some crystals may be a result of the continuation of metamorphism after crystallisation. The additional overlap of metamorphic titanite data from samples C04-16 (~12 kms to the west) and NM04-3 (~6 kms to the west) at c. 430 Ma supports the suggestion of an anatectic event and zircon growth at 429.5 ± 1.4 Ma. In addition, the pooling of melt in the fold hinges suggests that anatexis occurred simultaneously with deformation. Therefore the 429.5 ± 1.4 Ma zircon age also dates the folding event. This overlaps well with the c. 430 Ma age obtained for the formation of the foliation in the metagabbro (sample NM04-3).

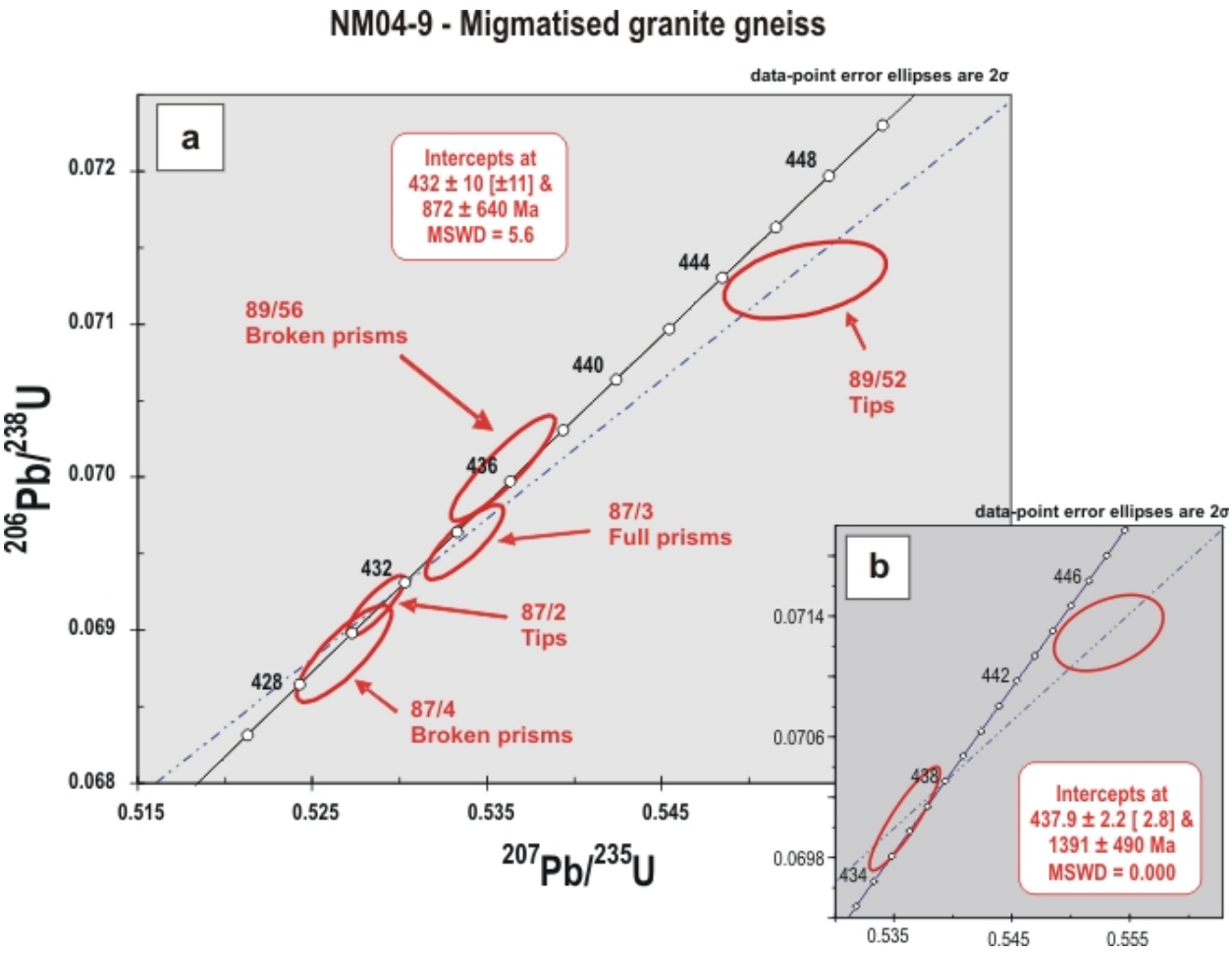


Figure 5.5 Concordia diagrams for zircons from sample NM04-9 (migmatised granite gneiss, Sørøya). *(a)* The distribution of concordant data points along Concordia is due to Pb-loss rather than inheritance since there is very little evidence for cores under CL. In contrast recrystallisation textures are commonly observed. However, fraction 89/52 does contain some inherited component indicated by an older $^{207}Pb/^{206}Pb$ age of 464 ± 14 Ma. A discordia line fitted to the data points has a very poor MSWD of 5.6, resulting from the presence of more than two zircon components. Therefore, based on the evidence for Pb-loss and little inheritance, the upper concordant data point is suggested to best approximate the date of intrusion (c. 436 Ma), with a metamorphic event at c. 430 Ma. *(b)* An estimation of the age of the inherited component is made by fitting a discordia line through the upper concordant and the discordant point. This yields an imprecise upper intercept of 1391 ± 490 Ma, suggesting a Proterozoic source.

A discordia line between the upper concordant (fraction 89/56) and the discordant point (fraction 89/52) yield an imprecise upper intercept of 1391 ± 490 Ma, suggesting a Mesoproterozoic source for the inheritance. However, owing to the small number of data points and large error, this intercept is not interpreted with confidence.

5.4 RJR02-58B (Granodiorite pegmatite) – Magerøy Island

5.4.1 TIMS data:

Three single crystal analyses were performed on selected simple prismatic overgrowths. The data indicate high to very high U contents (843-3,432 ppm), 206Pb/204Pb values between 2,875-22,110 and Th/U ratios of ≤0.01.

The three data points define a Concordia age of 425.9 ± 0.7 Ma, with an MSWD of 0.47 (figure 5.6).

5.4.2 Discussion:

Since the simple prismatic morphologies of the overgrowths correspond to a magmatically grown phase, 425.9 ± 0.7 Ma is interpreted as the age of intrusion for the pegmatite. This is approximately 5 m.y. younger than the 429.5 ± 1.4 Ma zircon age for anatexis determined for sample NM04-9 (migmatised granite gneiss) and the 431.4 ± 1.1 Ma titanite metamorphic age of sample C04-16 (garnet-hornblende syenogranite augen gneiss) from the overlying Hellefjord Group.

5.5 C04-2 (Granitic leucosome) – Magerøy Island

5.5.1 TIMS data:

One multicrystal (fraction 87/1) and a single crystal analysis (fraction 97/9) were performed on selected simple prisms with length:width ≤1:3, as well as one single crystal analysis on a simple prismatic tip from a crystal with length:width >1:3 (fraction 89/59). The data indicate moderate to high U contents (302-1,828 ppm), 206Pb/204Pb values between 1,972-10,604 and Th/U ratios of ≤0.20.

The result of the single tip analysis plotted concordantly at 425.5 ± 1.3 Ma. The two fractions of stocky prisms plotted discordantly with older 207Pb/206Pb ages of 864 ± 3 Ma and 712 ± 8 Ma, respectively (figure 5.7). A discordia line fitted to the data was anchored at 425.5 ± 1.3 Ma, and gave an imprecise upper intercept of 1002 ± 52 Ma (MSWD = 11.7).

5.5.2 Discussion:

The crystal morphology of the euhedral simple prisms with length:width ratios >1:3 (fraction 89/59) and lack of inheritance under CL suggests that this represents new zircon grown from a melt environment. This implies that the concordant 425.5 ± 1.3 Ma age represents the age of anatexis in the metasediments. This age also overlaps with the similar Concordia age determined for the granodiorite pegmatite (RJR02-58B) at 425.9 ± 0.7 Ma, assigning them both to the same event. The poor MSWD (11.7) of the discordia line suggests that the data are a combination of more than just the c. 425 Ma and a c. 1000 Ma component. Discordia lines anchored at 425.5 ± 1.3 Ma and taken through the individual discordant data points yield upper intercepts of

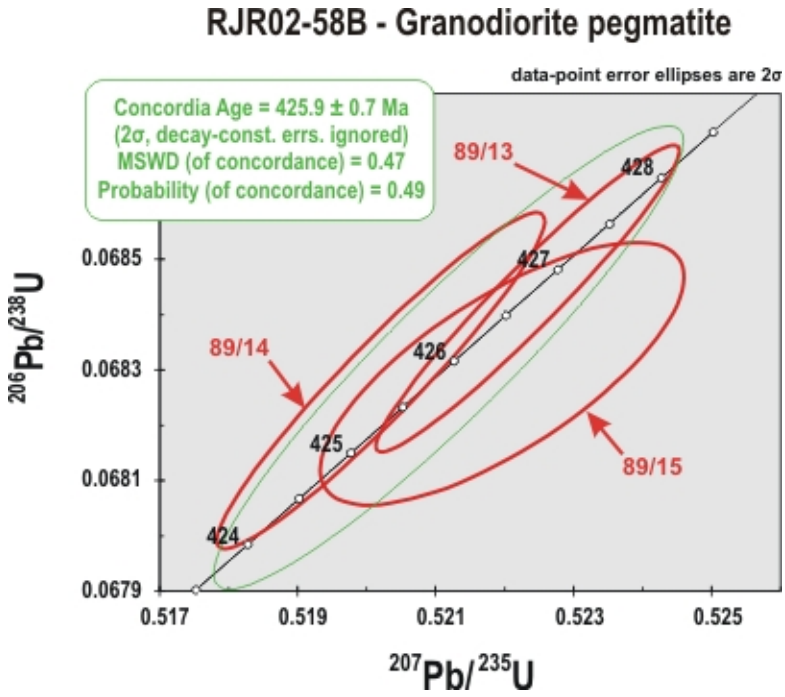


Figure 5.6 Concordia diagram for zircons from sample RJR02-58B (granodiorite pegmatite, Magerøya). The three single crystal analyses (red) yielded a Concordia age (green) of 425.9 ± 0.7 Ma (MSWD = 0.47). Despite the small sample sizes, the high U and Pb contents allowed for high accuracy.

952 ± 23 Ma (fraction 87/9) and 1007.0 ± 7.4 Ma (fraction 87/1), respectively. This suggests two Mesoproterozoic sources for the inheritance most likely entrained from the host Klubben Group psammites.

5.6 NM04-16 (Syenogranitic leucosome) – Magerøy Island

5.6.1 TIMS data:

Four single crystal analyses were performed on simple prismatic tips (fractions 89/16, 89/17 and 89/18) and a single prism with length:width >1:3 (fraction 89/55). The prism analysed in fraction 89/55 initially contained a biotite inclusion that extended along the c-axis for the entire length of the crystal. After abrasion the prism was cleaved in half along the inclusion, but the halves were themselves devoid of any inclusions or surficial remains of the biotite. Therefore, it is unlikely that the prism contained an inherited component. Tips were selected since they were also less likely to contain any inherited material. Data from the analyses indicate low to moderate U contents (71-281 ppm), Th/U ratios between 0.15-0.50 and 206Pb/204Pb ratios between 1,099-3,280.

Three of the analyses plot concordantly within error but are spread between approximately 980-957 Ma. The fourth point plots discordantly, with an older 207Pb/206Pb age of 952 ± 10 Ma (figure 5.8). A discordia line fitted to the

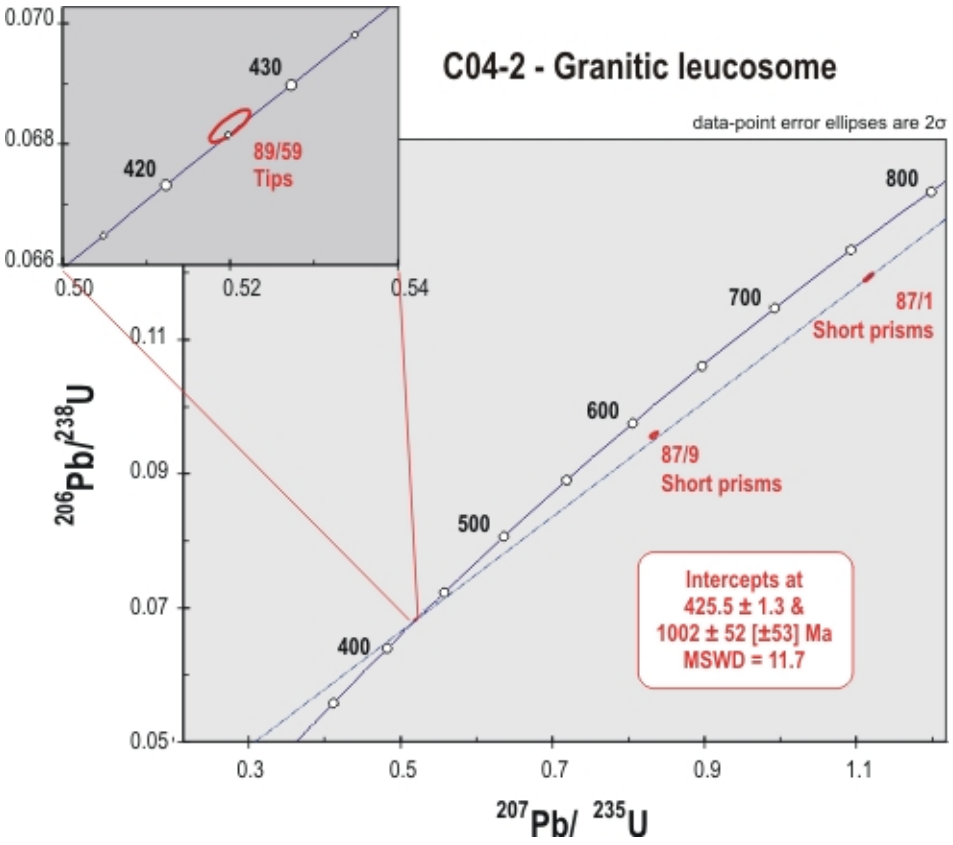


Figure 5.7 Concordia diagrams for zircons from sample C04-2 (granitic leucosome, Magerøya). The single concordant data point, fraction 89/59 *(inset)* yields an age of 425.5 ± 1.3 Ma. This age is within error of the Concordia age of c. 425 Ma age obtained for RJR02-58B (granodiorite pegmatite). Fractions 87/1 and 87/9 are both discordant, and define a discordia line (anchored at fraction 89/59) with an upper intercept of 1002 ± 52 Ma (MSWD = 11.7). Both the poor MSWD and CL evidence suggests that there are multiple sources of inheritance in addition to the youngest episode of growth at c. 425 Ma. Discordia lines through each of the discordant data points (anchored at 89/59) yielded upper intercepts of 952 ± 23 Ma (87/9) and 1007.0 ± 7.4 Ma (87/1), suggesting two Mesoproterozoic sources.

data has an upper intercept of 982 ± 12 Ma and an imprecise lower intercept of 704 ± 180 Ma, with an MSWD of 1.3.

5.6.2 Discussion

Two possibilities exist to explain the spread of concordant data points over ~23 m.y. along Concordia, and include inheritance and Pb-loss. Frequent observations of cores under CL makes it likely that some inheritance has occurred. This is confirmed by the older 207Pb/206Pb age of 952 ± 10 Ma fraction 89/16. In addition, the presence of recrystallisation textures observed in CL strongly suggests that a degree of Pb-loss has occurred.

However, since it is unlikely that fraction 89/55 contained any inherited component, the 980.9 ±2.6 Ma Concordia age is regarded as the best estimate for the melt-producing event. The lower intercept of discordia line (704 ± 180 Ma) is interpreted with caution due to the large error. Rb-Sr dating of the GMC

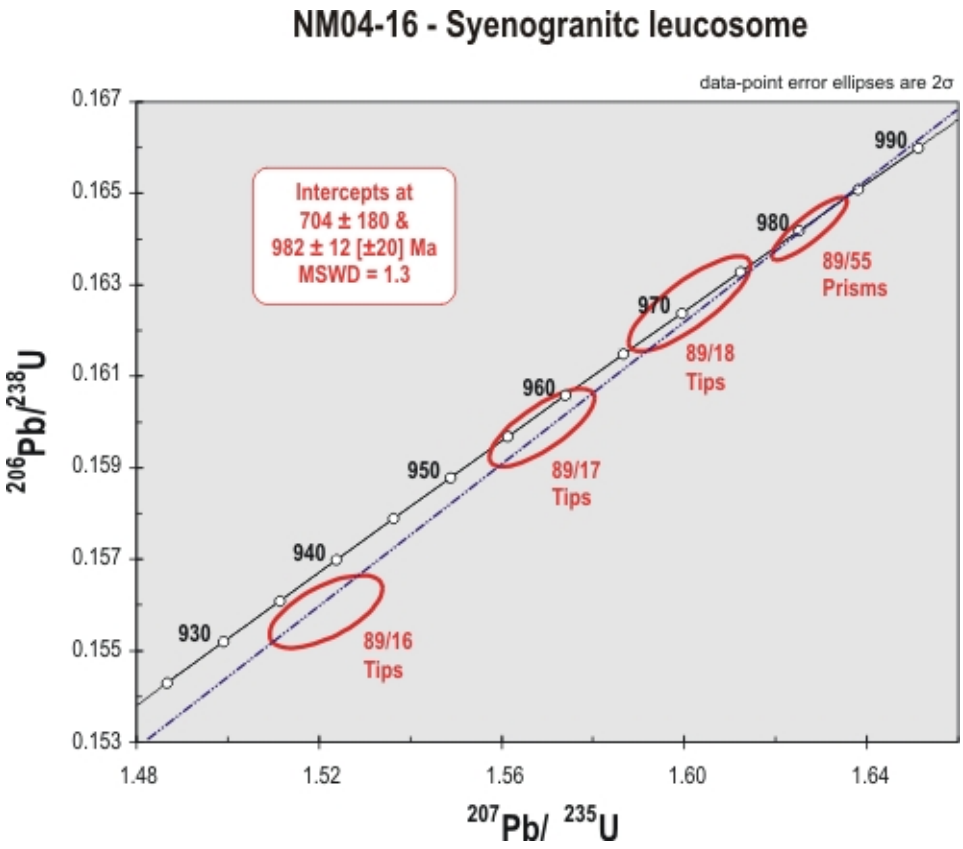


Figure 5.8 Concordia diagrams for zircons from sample NM04-16 (granitic leucosome, Magerøya). The spread of concordant ages appears to be a combination of inheritance and Pb-loss, since evidence for both was observed in CL. Fraction 89/55, however, is suggested to best approximate the age of migmatisation at 980.9 ±2.6 Ma. The lower discordant data point (fraction 89/16) has an older $^{207}Pb/^{206}Pb$ age of 952 ± 10 Ma, supporting an inherited component. A discordia line has an upper intercept of 982 ± 12 Ma, and an imprecise lower intercept of 740 ± 180 Ma. It is speculated that the lower intercept may reflect the effects of two events: one event at c. 850 Ma and a later event at c. 425 Ma, recorded in samples C04-2 (granitic leucosome) and RJR02-58B (granodiorite pegmatite). Discordia lines through fractions 89/16 and 89/17, anchored at 850 Ma, yield upper intercept ages of 1087 ± 90 Ma and 999 ± 58 Ma respectively, and are within error of the upper intercepts obtained from C04-2 for inheritance ages.

by Andersen et al. (1982) confirmed c. 410 Ma whole-rock resetting, suggesting that the c. 740 Ma age obtained from the zircon discordia may be a 'ghost' event caused by partial resetting of the U-Pb systems. However, Corfu et al. (in press) report c. 850 and c. 700 Ma ages for two distinct orogenic events in the KNC. In view of this, the 704 ± 180 age may be a real age related to either one of these orogenies. Upper intercepts for discordia lines through fractions 89/16 and 89/17 anchored at 425 Ma (963 ± 17 Ma and 966 ± 13 Ma, respectively) and 700 Ma (993 ± 34 Ma and 975 ± 25 Ma, respectively) yield ages for the inherited component that are younger than the c. 980 Ma magmatic age of fraction 89/55. However, if the discordia lines are anchored at 850 Ma (± 10 Ma), the upper intercepts become 1087 ± 90 Ma and 999 ± 58 Ma, respectively, yielding a more realistic age for the inherited component. In addition, the latter intercepts are within error of the intercept obtained for fraction 87/1, sample C04-2 (1007.0 ± 7.4 Ma), suggesting a similar source. Although this is

not conclusive, it seems more likely that the lower intercept for sample NM04-16 is related to an orogenic event at c. 850 Ma, rather than a c. 410 Ma event. The latter would still have led to Pb-loss subsequent to the c. 850 Ma orogeny, causing the large error currently observed in the lower intercept. In addition, the c. 980 Ma age obtained from the second generation leucosome yields a lower limit for the D1 deformation and anatexis.

6. Regional Implications

The original interpretation of Roberts (1968) that the gabbroic bodies in the Hellefjord Group are tectonically transported equivalents of the SIP is annulled for the following reasons. Most importantly, a Concordia age of 436.7 ±0.8 Ma obtained from euhedral magmatic zircons places it well outside the range for the intrusion of mafic plutons of the SIP at c. 570-650 Ma (R.J. Roberts, in press; R.J. Roberts et al., 2004). Therefore, the metagabbro (sample NM04-3) cannot be part of the SIP. In addition, the corresponding date of 435.9 ± 1.6 Ma for the initial intrusion of the granite (sample NM04-9) suggests that it is co-genetic with the gabbro. Consequently the metagabbro (sample NM04-3) is suggested to be intrusive into the Hellefjord Group rather than a thrusted component. In light of this, the data for the plutons from the Hellefjord Group suggest a relatively simple tectonothermal evolution related to the *Scandian* event (figure 6.1). Magmatic activity occurred from c. 441 Ma to c. 436 Ma, starting with the intrusion of a syenogranite (sample C04-16), followed by a granite (sample NM04-9) and gabbro (sample NM04-3). *Scandian* post-intrusion metamorphism in the HG appears to be relatively well defined at c. 430 Ma, and is responsible for local anatexis and growth of new zircon (sample NM04-9) and titanite (sample C04-16 and NM04-3) as well as partial resetting of pre-existing zircon and titanite (sample C04-16 and NM04-3). In addition, the c. 430 Ma event appears to be responsible for the formation of metamorphic fabrics in the granite (sample NM04-9) and gabbro (sample NM04-3). This association is extended to sample C04-16 (syenogranite), considering the small distance between the samples and the overlap of metamorphic ages at c. 430 Ma. In contrast, data from the Klubben Group on Magerøya indicate a more complicated tectonothermal history (figure 6.1). Samples C04-2 and RJR02-58B show that the *Scandian* event produced upper amphibolite/granulite facies metamorphism and anatexis in the Klubben Group at c. 425 Ma. These anatectic melts allowed for the growth of new magmatic zircon and overgrowths around pre-existing grains. In contrast, sample NM04-16 from the Gjesvær Migmatite Complex (2 km N of C04-2) shows no definite U-Pb zircon evidence for a *Scandian* event, suggesting that the latter did not play an important role in its tectonometamorphic evolution. However, the CL-bright rims observed in the last growth phase in zircons from NM04-16 are interpreted to be a result of minor recrystallisation and Pb-loss related to the *Scandian*. This would be in agreement with the 410 ± 28 Ma metamorphic age obtained by Andersen et al. (1982) for Rb-Sr resetting in the Gjesvær Migmatite Complex.

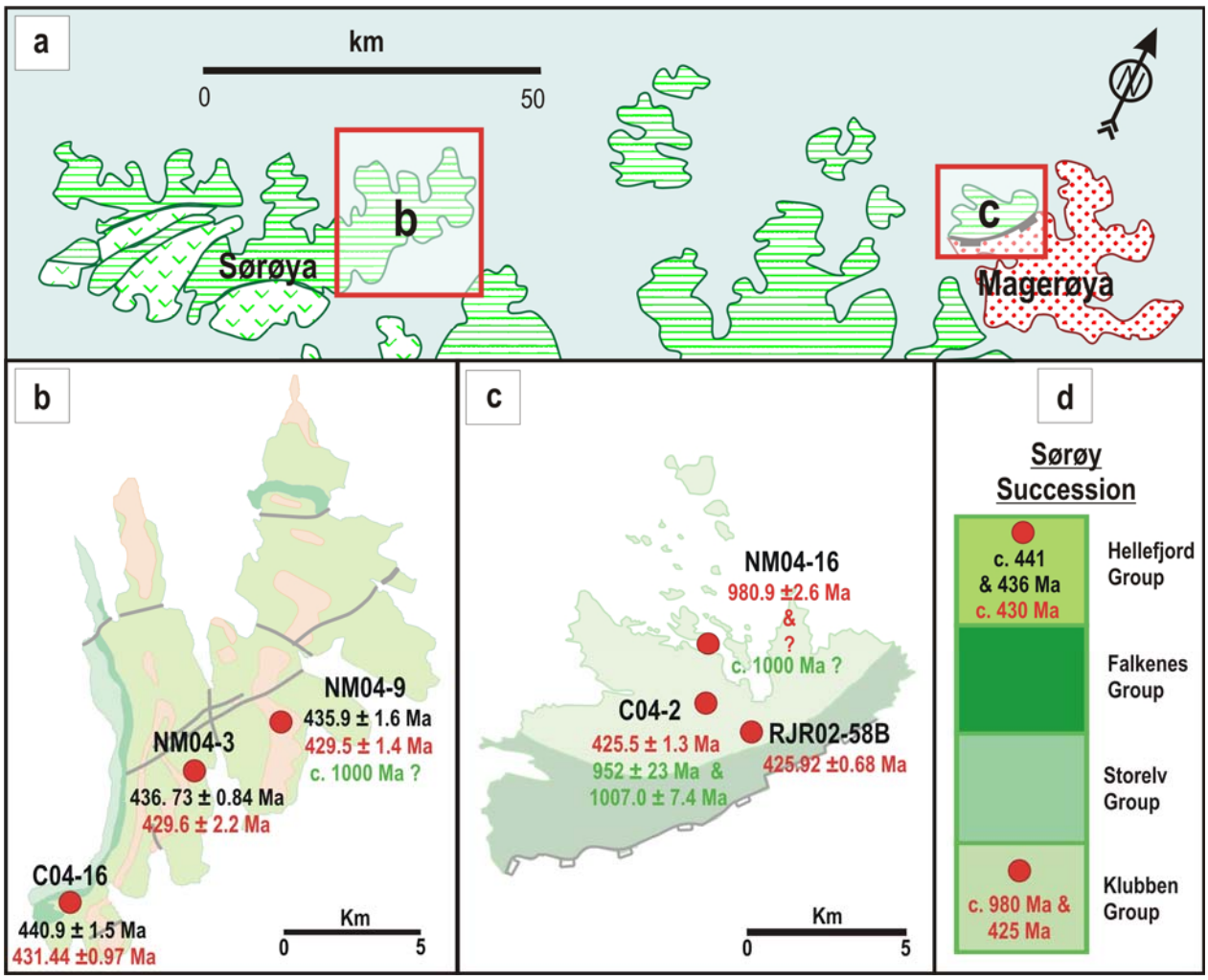


Figure 6.1 Schematic summary of results obtained in this study. *(a)* Relative positions of Sørøya and Magerøya. Inset *(b)* shows the intrusive (given in black) and metamorphic ages (given in red) for the various plutons intruding Hellefjord Group on Sørøya. Magmatic activity appears to have continued for c. 5 m.y. (from c. 441-436 Ma), while metamorphism is relatively well constrained to c. 430 Ma. Both magmatism and metamorphism are therefore related to the *Scandian* event. In contrast, two distinct episodes of metamorphism (given in red) are recorded in the Klubben Group on Magerøya *(c)* – one at c. 980 Ma (*Grenvillian*) and one at c. 425 Ma (*Scandian*). Although both the Klubben Group and Hellefjord Group have suffered *Scandian* deformation and metamorphism, there is a slight discrepancy in the specific timing *(d)*, with younger ages (c. 425 Ma) recorded in the lower Klubben Group compared to the older c. 430 Ma ages recorded in the upper Hellefjord Schists. In addition, the Hellefjord Group does not record the c. 980 Ma event seen in the Klubben Group. Approximated ages of inherited components (given in green) observed in both the Hellefjord Group and the Klubben Group suggest a Mesoproterozoic source, although this is not considered conclusive based on the large errors associated with the Concordia intercepts.

The c. 980 Ma age obtained for the younger leucosome generation from the Gjesvær Migmatite complex (NM04-16) overlaps well with 970-980 Ma *Grenvillian* ages for adamellites and a granite intruding the Klubben Group in the Olderfjord Nappe (Kirkland et al., 2005a; Kirkland et al., 2006; Corfu et al., 2005a). This supports the existence of a major tectonothermal event in the KNC related to the amalgamation of Rodinia (Meert & Torsvik, 2003). In addition, the upper intercept age obtained for fraction 87/9, sample C04-2 (952 ± 23 Ma) is almost within error of the c. 980 Ma age from sample NM04-18 and

may reflect the presence of an inherited zircon component grown during this *Grenvillian* event. CL-bright rims observed around cores from C04-2 are also suggested to be related to this event. The interpretation of the lower discordia intercept of NM04-16 (704 ± 180 Ma) is somewhat ambiguous due to the large error. As discussed in section 4.6.5, intercepts through the discordant data points only yield realistic ages of inheritance if they are anchored at c. 850 Ma (± 10 m.y.). An anchor-age of <850 Ma (e.g. 425 Ma) yields upper intercepts that are younger than the magmatic data point at 980.9 ± 2.6 Ma. Ages of 800-870 Ma are known from numerous intrusive rocks throughout the KNC (e.g. Lillefjord granite, Klubben Group, 849 ± 6 Ma, Corfu et al., in press; Litlefjord granite, Klubben Group, 850 ± 15 Ma, Kirkland & Daly, 2003), supporting a possible c. 850 event in the Gjesvær Migmatite Complex. A *Scandian* overprint and related Pb-loss may then account for the large error observed in the lower intercept. In addition, discordant fractions 87/1 (sample C04-2) and 89/16 (sample NM04-16) yield upper intercepts of c. 1000 Ma (1007.0 ± 7.4 Ma and 1087 ± 90 Ma, respectively), suggesting a similarly-aged Mesoproterozoic source for the inherited component.

The original model of a conformable Sørøy Succession (Ramsay, 1971b) dictates that the entire succession suffered the same tectonometamorphic evolution. However, the assumption of a conformable sedimentary sequence appears to be invalid for several reasons. Firstly the Hellefjord Group has not been intruded by the SIP, and conversely, the *Scandian* plutonism present in the Hellefjord is not present in underlying units of the Sørøy Succession. Secondly, migmatites of the Gjesvær Migmatite Complex (Klubben Group) that were supposedly of early Caledonian origin (c. 500; Sturt et al., 1978), are related to a distinct *Grenvillian* event. Migmatites from the Hellefjord Group (sample NM04-9, migmatised gneiss), which were originally suggested to be part of the same early Caledonian anatexis (Sturt et al., 1978), are *Scandian* in origin. Thirdly, *Scandian* metamorphic ages in the Hellefjord (c. 430 Ma) are slightly older than those in the Klubben Group (c. 425 Ma). These data suggest that there may be a previously undetected structural break in the Sørøy Succession. A marked decrease in deformation is observed in the Hellefjord Group, from highly deformed at the contact with the Falkenes Group to relatively undeformed further away from the contact. It is also noteworthy that no transitional facies has been observed between the Åfjord Group and the Hellefjord Group (Ramsay, 1971). Therefore it appears that the Hellefjord may represent a completely different tectonic unit to the rest of the Sørøy Succession. A structural break is therefore proposed at the base of the Hellefjord Group (figure 6.2)

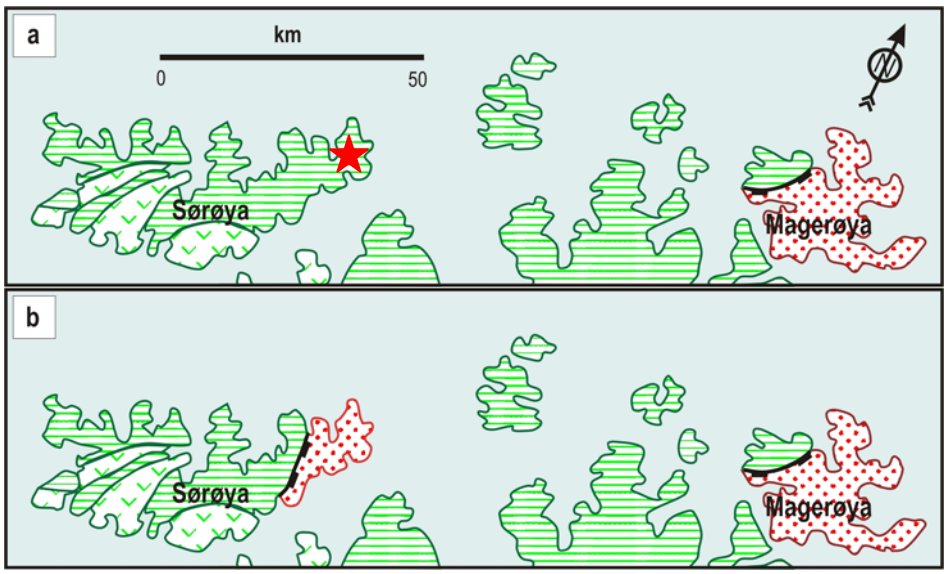


Figure 6.2 Ages for plutonism in the Hellefjord Group presented in this study (c. 441-436 Ma) as well as the dominance of metaturbidite sequences in this unit are greatly similar to the lithological characteristics of the Magerøy Nappe (metaturbidite sequences) and ages of intrusion determined by Corfu *et al.* (in press) (c. 440-436 Ma). Based on this, the present study suggests that the Hellefjord Group, currently of the Sørøy Succession (diagram *a*, indicated by a red star on Sørøy Island), is an extension of the Magerøy Nappe (diagram *b*) and rests unconformably on the underlying Sørøy Succession.

The Magerøy Nappe overlying the KNC consists largely of several formations of thick meta-turbidites sequences of Silurian age (Curry, 1975; Andersen, 1984) that are intruded by bimodal plutons dated between c. 440-436 Ma (Corfu et al., 2006). These characteristics are similar to the HG, which is also a) largely composed of thick metaturbidite sequences (Roberts, 1968; Ramsay, 1971), and b) intruded by bimodal plutonism from c. 441-436 Ma as shown by this study. In addition, no older tectonothermal activity is recorded in either the HG (this study) or the MN (Corfu et al., 2006). Based on the similarities in style of deposition and ages and compositional range of intrusions in the HG and Magerøy Nappe, it is suggested that the HG is an extension (or equivalent unit) of the Magerøy Nappe (figure 6.2). Furthermore, Corfu *et al.* (2006) remarked on the peculiarity of rapidly deposited low temperature turbidite/greywacke successions intruded by high temperature mafic/ultramafic/granitic intrusions. This association has also been noted by other authors for the Hidaka magmatic zone (Maeda & Kagami, 1996) and the Ofoten-Efjorden area, northern Norway (Northrup, 1997). Both ridge subduction, suprasubduction zone rifting and basinal rifting have been put forward as possible explanations (Corfu *et al.*, 2006; Northrup, 1997; Maeda & Kagami, 1996). In the case of progressive ridge subduction, MORB magmas erupted from the ridge will at first intrude the accretionary prism and associated deep water sediments. This leads to anatexis of the sediments and subsequent intrusion of granites. Some intermediate

magmas (notably tonalite) from mixing of MORB and the anatectic melts are also observed (Northrup, 1997; Maeda & Kagami, 1996). It is less clear how this association is achieved with basinal rifting since the turbidites are deposited along the margins of the basin while MORB volcanism occurs along the central spreading ridge. Furthermore, rifting is usually associated with additional more alkaline magmas besides granites and gabbros (e.g. feldspathoid-syenite, syenite; Burke *et al.,* 2003; Bailey, 1992, 1977, 1974). Since only gabbros and granites are observed in both the HG and the Magerøy Nappe (Corfu *et al.*, 2006; Roberts, 1968; current author) development in a rift environment is thought unlikely. However, the alternative model of ridge subduction is likely only if the granites are proven to be derived from the host sediments. However, this is beyond the current scope of this project. On the other hand, the presence of closely temporally spaced bimodal volcanism (e.g. metagabbro – NM04-3, 436.7 ±0.8 Ma; migmatised granite gneiss – NM04-9, 435.9 ± 1.6 Ma) intruding into a turbidite host and the absence of alkali magmatism suggests that ridge subduction may be a plausible scenario.

Geophysical constraints on the evolution of the Caledonian Orogeny (figure 1.1) have determined that the docking of Baltica-Avalonia with Laurentia occurred between c. 440 Ma and 420 Ma. The intrusion of the plutons into the turbidite succession during the evolution of the ridge-trench intersection provides a maximum age for the thrusting of the Magerøy Nappe of c. 436 Ma. However, the ages obtained for the deformation and anatexis of the Hellefjord Group suggests that collision of the ridge-trench complex with the Kalak Nappe Complex may have occurred at c. 430 Ma. Furthermore, the c. 425 Ma ages obtained for the intrusion of the granodiorite pegmatite (sample RJR02-58B) and migmatisation of the Klubben Group (sample C04-2, granitic leucosome) are suggested to best approximate the minimum age for the thrusting of the Magerøy Nappe over the Kalak Nappe Complex. It therefore appears as though thrusting of the Magerøy Nappe may have occurred between c. 430-425 Ma.

7. Conclusions

The bimodal plutonism that intruded the Hellefjord Group (Sørøy-Seiland Nappe, Sørøy Island) from c. 441-436 Ma is not related to the large scale SIP intrusions (c. 570-560 and c. 530-520 ma) present in the underlying Sørøy Succession. However, the bimodal plutonism is coeval with similar magmatic activity in the Magerøy Nappe overlying the Kalak Nappe Complex dated at c. 440-436 Ma (Corfu et al., 2006). Additionally, the Hellefjord Group and Magerøy Nappe are both dominantly composed of metaturbidite sequences. Therefore, a structural break is proposed at the base of the Hellefjord Group in the Sørøy Succession of the Kalak Nappe Complex, and it is suggested that the Hellefjord Group represents an extension of or an equivalent nappe to the Magerøy Nappe. Additionally, the intrusion of bimodal volcanism (with an absence of alkaline magmas) into a turbiditic sequence suggests that the Hellefjord Group, like the Magerøy Nappe, may have developed at a ridge-trench intersection.

The Klubben Group (Olderfjord Nappe; Magerøy Island) contains evidence for an extensive pre-Caledonian evolution. The c. 980 Ma age obtained from the second generation leucosome in the Gjesvær Migmatite Complex ties the anatexis to a major *Grenvillian* event recorded elsewhere in the Olderfjord and Kolvik Nappes (Kirkland et al., in press; Corfu et al., 2005b). This ties the initial evolution of the KNC to the amalgamation of Rodinia. D1 deformation and anatexis is therefore older than c. 980 Ma. Data from this study further suggest a later period of tectonothermal activity at c. 850 Ma, which caused partial U-Pb resetting in the Gjesvær Migmatite Complex. This was later followed by the thrusting of the Magerøy Nappe at c. 425 Ma during the Caledonian Orogeny, and locally produced upper amphibolite-granulite conditions in the underlying Kalak Nappe Complex. Figure 7.1 is a summary of the evolution of the KNC.

A window of 5 m.y. (from c. 430-425 Ma) is suggested for the thrusting of the Magerøy Nappe over the Kalak Nappe Complex. The upper limit of c. 430 Ma is based on the formation of post-intrusion deformational fabrics in the Hellefjord Group. The lower limit is constrained by the c. 425 Ma age for anatexis and intrusion in the Klubben Group.

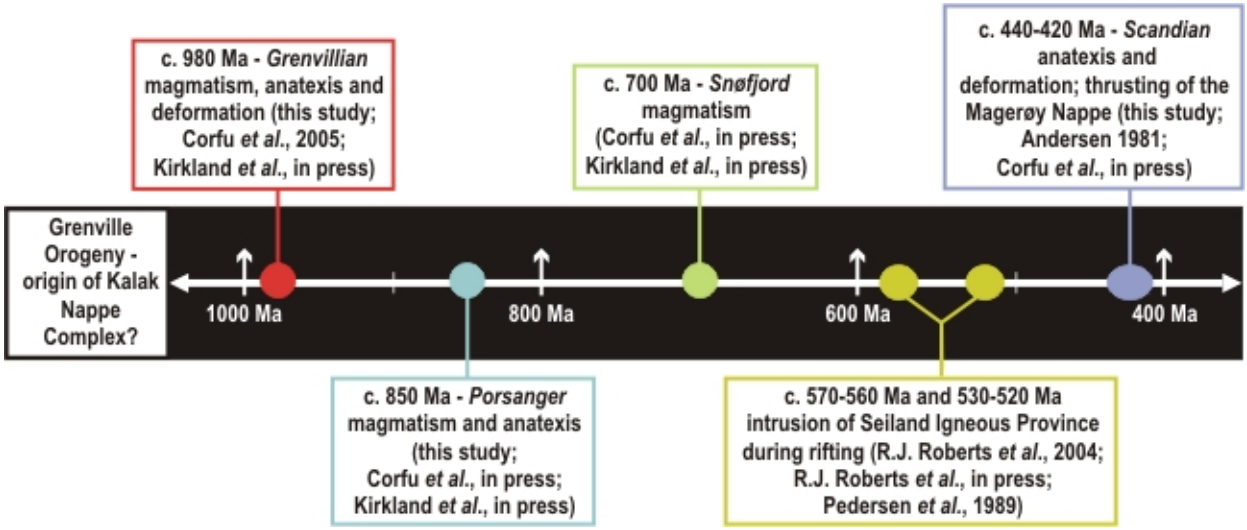


Figure 7.1 Timeline summarising the evolution of the Kalak Nappe Complex (KNC). The KNC is suggested to have originated off the Baltic margin during the *Grenville* Orogeny (Corfu *et al.*, in press, a; Kirkland *et al.*, in press) with subsequent deformation and metamorphism at the end of the *Grenville*. This was followed by at least four tectonothermal events, including the *Porsanger* (c. 850 Ma) and *Snøfjord* (c. 700 Ma) orogenies and possible rifting related intrusion of the SIP (c. 570-560 Ma and c. 530-520 Ma). The *Scandian* event resulted only in deformation and local anatexis in the KNC close to the thrusted boundary with the Magerøy Nappe.

Appendix A - Visually estimated modal proportions

Table A- 1 Visually estimated modal proportions

	C04-16	NM04-3	NM04-9	RJR02-58B	C04-2	NM04-16
K-feldspar	22	-	23	15	40	27
Myrmekite	5	-	3	-	1	<1
Plagioclase	10	44	13	40	21	10
Quartz	20	-	30	34	30	40
Biotite	10	5	20	6	5	20
Muscovite	-	-	-	5	3	3
Amphibole	20	40	<1	-	<1	-
Garnet	5	-	10	<1	-	<1
Titanite	7	10	<1	-	-	<1
Zircon	1	-	<1	1	<1	<1
Apatite	<1	-	-	-	<1	-
Oxides	<1	1	<1	<1	<1	<1
K	42	-	35	17	44	35
P	19	52	20	45	23	13
Q	38	-	45	38	33	52
PYX		48				
Name	Syenogranite	Gabbro	Granite	Granodiorite	Granite	Syenogranite

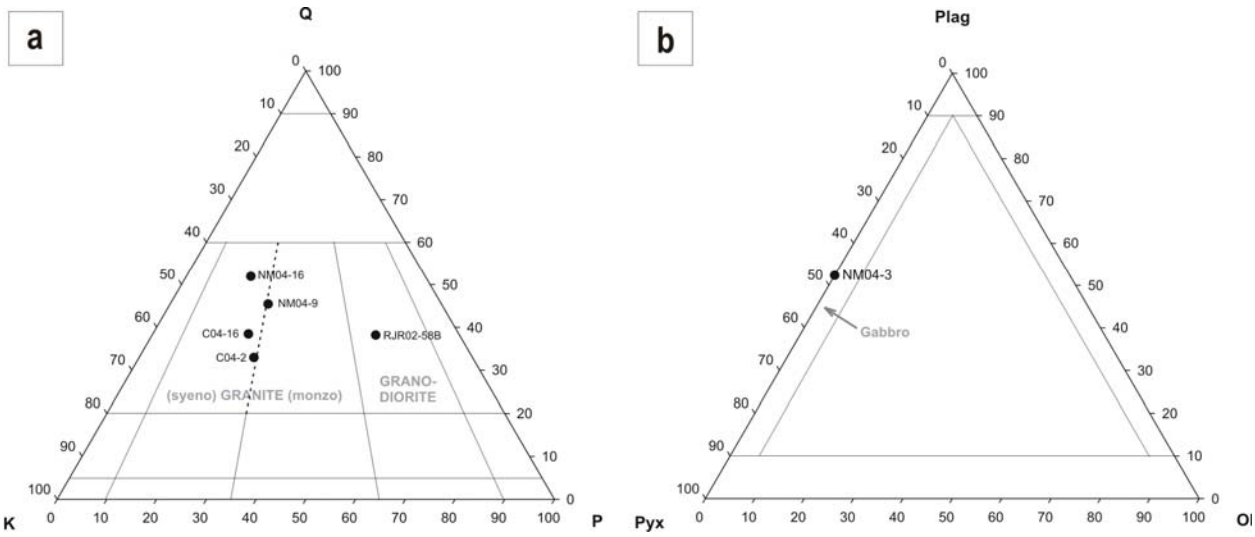


Figure A- 1 Modal classification of samples based on visually estimated modes. *(a)* Classification of felsic plutons and *(b)* mafic rocks *(After Streckeisen, 1976)*. Note that the metamorphic amphibole after pyroxene in the metagabbro (NM04-3) is used to determine the original composition of the gabbro.

Fraction Analysed	Weight [µg]*	Pb (total) (ppm)*	U (ppm)*	Th/U	$^{206}Pb/^{204}Pb$	Common Pb [pg] ‡	$^{207}Pb/^{206}Pb$§	2σ [abs]¶	$^{207}Pb/^{235}U$§	2σ [abs]¶	$^{206}Pb/^{238}U$§	2σ [abs]¶	rho	$^{206}Pb/^{238}U$§ (Ma)	$^{207}Pb/^{235}U$§ (Ma)	$^{207}Pb/^{206}Pb$§ (Ma)	2σ [abs]¶
C04-16 (Sample 1, Syenogranitic augen gneiss, Sørøy Island)																	
87/5 (Long prisms)	25	22	311	0.33	12639	2.7	0.05585	0.00010	0.53437	0.0019	0.06939	0.00023	0.86	432	435	447	4
87/6 (Tips)	15	14	200	0.45	3771	3.5	0.05554	0.00013	0.53385	0.0020	0.06972	0.00023	0.81	434	434	434	5
87/7 B (Short prisms)	1	62	863	0.42	2912	1.3	0.05568	0.00016	0.5412	0.0029	0.07050	0.00032	0.85	439	439	440	6
89/51 (Tips)	1	24	337	0.33	896	1.7	0.05597	0.00042	0.5403	0.0048	0.07002	0.00031	0.55	436	439	451	17
89/57 (Long prisms)	1	42	524	0.45	452	5.4	0.05559	0.00041	0.5425	0.0046	0.07078	0.00024	0.48	441	440	436	16
89/S3 (Pale)	43	4	43	0.05	144	63.2	0.05517	0.00128	0.527	0.012	0.06922	0.00026	0.12	431	430	419	51
89/S4 (Yellow)	63	5	62	0.06	191	97.2	0.05558	0.00095	0.5304	0.0092	0.06922	0.00021	0.16	431	432	435	38
NM04-3 (Sample 2, Metagabbro, Sørøy Island)																	
87/11	1	14	131	1.41	160	4.1	0.0551	0.0014	0.532	0.014	0.07002	0.00027	0.38	436	433	416	54
87/12	1	17	193	1.34	1385	0.6	0.05550	0.00027	0.5384	0.0032	0.07036	0.00026	0.59	438	437	432	11
89/54	1	11	126	1.18	1315	0.4	0.05573	0.00034	0.5361	0.0040	0.06977	0.00034	0.59	435	436	441	13
89/58	1	21	240	1.32	2075	0.5	0.05544	0.00021	0.5360	0.0030	0.07012	0.00029	0.73	437	436	430	9
89/S8	52	4	22	3.78	91	66.8	0.0549	0.0022	0.521	0.021	0.06891	0.00037	0.09	430	426	407	89
117/S7	30	4	18	2.95	65	50.0	0.0532	0.0034	0.498	0.032	0.06789	0.00056	0.07	423	410	338	100
117/S10	22	5	25	3.90	102	28.3	0.0547	0.0018	0.518	0.017	0.06867	0.00032	0.08	428	424	399	73
NM04-9 (Sample 3, Migmatised granite, Sørøy Island																	
87/2 (Tips)	17	21	304	0.27	5765	3.9	0.05544	0.00007	0.5286	0.0013	0.06916	0.00016	0.86	431	431	430	3
87/3 (Prisms)	16	16	231	0.27	5373	3.0	0.05563	0.00011	0.5337	0.0018	0.06958	0.00020	0.83	434	434	438	4
87/4 (Broken prisms)	10	17	258	0.20	3195	3.5	0.05550	0.00013	0.5268	0.0022	0.06885	0.00026	0.83	429	430	432	5
89/52 (Tips)	11	14	182	0.33	535	17.3	0.05628	0.00035	0.5532	0.0038	0.07129	0.00021	0.41	444	447	464	14
89/56 (Broken prisms)	1	29	417	0.33	5473	0.3	0.05548	0.00011	0.5359	0.0024	0.07006	0.00028	0.90	437	436	432	4
RJR02-58B (Sample 4, Granodioritic pegmatite, Magerøy Island)																	
89/13 (Tips)	1	198	3189	0.00	22110	0.6	0.055361	0.000052	0.5223	0.0018	0.06843	0.00023	0.96	427	427	427	2
89/14 (Tips)	1	213	3432	0.00	14009	1.0	0.055255	0.000064	0.5202	0.0019	0.06828	0.00025	0.95	426	425	423	3
89/15 (Tips)	1	52	843	0.01	2875	1.3	0.05543	0.00016	0.5220	0.0022	0.06829	0.00019	0.74	426	426	430	6
C04-2 (Sample 5, Granitic leucosome, Magerøy Island)																	
87/1 (Short prisms)	3	35	302	0.20	10604	0.6	0.06784	0.00011	1.1168	0.0048	0.11939	0.00047	0.93	727	761	864	3
87/9 (Short prisms)	1	40	452	0.07	1972	1.4	0.06312	0.00023	0.8333	0.0039	0.09576	0.00037	0.66	590	615	712	8
89/59 (Tips)	1	115	1828	0.00	2200	3.6	0.05521	0.00012	0.5200	0.0020	0.06830	0.00022	0.81	426	425	421	5
NM04-16 (Sample 6, Syenogranitic leucosome, Magerøy Island)																	
89/16 (Tips)	1	20	119	0.50	1099	1.1	0.07081	0.00036	1.522	0.010	0.15585	0.00065	0.63	934	939	952	10
89/17 (Tips)	1	43	281	0.15	1300	2.2	0.07117	0.00028	1.5688	0.0094	0.15988	0.00069	0.76	956	958	962	8
89/18 (Tips)	1	28	175	0.25	1332	1.4	0.07143	0.00029	1.601	0.011	0.16258	0.00085	0.81	971	971	970	8
89/55 (Prisms)	2	12	71	0.31	3280	0.4	0.07187	0.00015	1.6274	0.0068	0.16423	0.00056	0.86	980	981	982	4
Standard																	
STD 91500	27	10	53	0.35	2549	6.4	0.07487	0.00010	1.8550	0.0050	0.17970	0.00042	0.86	1065	1065	1065	3
STD 91500 (Wiedenbeck *et al.*, 1995)			**81.2**		**12000-162000**		**0.07488**	**0.00001**	**1.8502**	**0.0008**	**0.17917**	**0.00008**		**1062.4**		**1065.4**	0.3

‡ Initial Pb + Blank

§ Corrected for fractionation, spike, blank and initial Pb

¶ Errors calculated by propagating the main sources of uncertainty

* Weight and concentrations known to better than 10%, except for those near and below the c. 1µg limit of the balance resolution

Appendix C - Methods

Relevant theory is given in italics following the associated method.

C.1 Sample Preparation

C.1.1 Sampling:

Hand samples of no more than 1-2 kg were selected, with special attention paid to the selection of specimens that represented the particular features of the rocks that were to be dated. Due to zircon's resistance to weathering, less attention was paid to selecting pristine samples since slight amounts of weathered surface would not upset the U-Pb systems in the zircons. Where necessary (and possible) the samples were further reduced using a diamond edged saw – this was done primarily to isolate specific features of the sample (e.g. a specific phase of anatectic melt) in order to increase the chances of recovering zircons related to that feature.

C.1.2 Crushing:

Prior to crushing, samples were brushed clean to remove any loose surface particles and placed in an ultrasonic bath for 10 minutes, after which they were transferred to an oven to dry overnight. Crushing was performed in a clean crushing room at Department of Geosciences, Oslo University, with extraction vents placed at the openings of both the primary and secondary crushers. All work surfaces were wiped clean. As an extra precaution, clean paper towel was laid down to work on. All working parts and contact surfaces of the primary and secondary crushers were removed before crushing, scrubbed and placed in an ultrasonic bath for 10 minutes, followed by thorough rinsing with ethanol and oven drying. Primary crushing was done using a Sturtevant Roll Jaw Crusher, reducing the sample size to a maximum of 7 mm in size. Secondary crushing was done with a Retch Cross Beater (rotor) Mill SK 100. The sample was put through the rotor mill twice, first reduced to <5 mm diameter and then to <0.5 mm diameter.

C.1.3 Mineral separation:

Primary separation was performed on a Wilfley table. Only the densest fraction was collected, which included zircon, titanite, plagioclase, rutile, pyroxene, garnet and sulfides. The water streams on the Wilfley board were set to minimise the amount of plagioclase collected in the heavy fraction in order to increase the efficiency of the heavy liquid separation. The collected fraction was washed into a porcelain dish with ethanol and dried overnight in an oven.

Secondary separation was performed firstly by vertical free fall magnetic separation using a Frantz Isodynamic Magnetic Separator, model L-1 (1.5 Amperes), and secondly by horizontal slope magnetic separation using a Frantz Magnetic Barrier Separator, model LB-1 (15° horizontal tilt, 15° vertical tilt, 0.4 Amperes). Due to a positive correlation observed between the amount of paramagnetism (magnetic susceptibility), uranium content and discordance (Silver & Deutsch, 1963; Krogh, 1982b), zircons in the magnetic fractions from magnetic free-fall and horizontal slope separation were not chosen for analyses.

The magnetic fraction from the 'free fall' separation removed most of the oxides, sulfides and garnet. The non-magnetic fraction from the vertical 'free fall' was transferred to the horizontal slope separator, which further separated out any paramagnetic minerals such as pyroxene, amphibole, sphene and only the most U- and Th-rich zircons. The non-magnetic fraction from the horizontal slope separator contained zircon and sphene ideal for dating, as well as feldspars.

Magnetic separation methods are based on permanent magnetism / paramagnetism versus non-magnetism (diamagnetism) (Huheey, Keiter & Keiter, 1993; Kearey, Brooks & Hill, 2002). Paramagnetic minerals have unpaired electrons that align themselves under the influence of an external magnetic field, creating a temporary induced magnetic field (i.e. induced magnetism). The greater the amount of unpaired electrons in the mineral's atoms, the greater the induced magnetic field and the smaller the external field required to induce magnetic properties. Diamagnetic minerals (non-magnetic) have only paired electrons – under an external magnetic field, the opposed spin of the electron pairs cancel out each other's induced magnetic field and the mineral remains non-magnetic.

For the final mineral separation, Diiodomethylene (DIM = methylene iodide, ρ = 3.28 kg/dm^3) and the non-magnetic fraction of the horizontal slope magnetic separation were poured into a separating funnel. DIM allows for the separation of the accessory minerals most commonly used for U-Pb dating (e.g. zircon, monazite, titanite, baddeleyite, xenotime) from other less dense minerals that passed through the magnetic separation (e.g. feldspar). After agitating the DIM-sample combination, the heavy minerals were allowed to settle to the bottom of the separating funnel and decanted into a filtration paper, repeating several times. The collected heavy mineral fraction was washed with acetone and ethanol to remove any trace of the DIM.

Only sample NM04-9 had a sufficiently large heavy mineral fraction after DIM separation to warrant further horizontal magnetic separation (15° horizontal tilt, 15° vertical tilt, 1.5 Amperes).

C.1.4 Mineral picking:

The heavy mineral fraction was transferred into a plastic Petri dish filled with ethanol. A Leica MZ16 binocular microscope with fibre optic light source and fine nosed tweezers were used for picking. Zircon selection was based on the morphologies of Pupin (1980), with preference given to 'simple euhedral prisms' dominated by one of either the common prism or pyramidal faces (also see Appendix D, section D-1). Euhedral simple prismatic crystals (or parts of crystals) with no evidence for cores or inclusions were selected for abrasion and analysis. A simple prismatic crystal is defined as a crystal with one dominant prism and pyramidal termination (also see Appendix E, section E-1). It was generally accepted that broken tips and crystals large length: width ratios of >1:3 stood a better chance of containing no inheritance, and were preferentially selected. However, this value is somewhat arbitrary and the division may be adapted for a specific sample if backed by visual evidence. Where the last magma phase was represented by large prismatic overgrowths on cores, the tips were removed from the cores by gently squeezing the latter with a pair of tweezers. The cores would usually crack and fall away, leaving core-free tips.

C.1.5 Abrasion:

Abraders were based on the design of Krogh (1982b). The selected zircons were pipetted into the base of the abrader. Pyrite was added (~5 mg pyrite: 0.5-1 mg zircon; Krogh, 1981) to keep the crystals from completely disintegrating during abrasion, to aid rounding of the crystals and to provide a smooth polish. Air exit vents in the abrador were covered by 28 μm abrader mesh. Any residual ethanol in the abrader was removed by keeping the abrader at a low pressure for about 30 min. The pressure was then increased and left overnight. Where multiple cycles of abrasion were required within one day, it was also possible to achieve comparable results by increasing the air pressure and leaving the abrader for only 4-6 hours. The results were usually well rounded crystals with a shiny, smooth finish. Titanites were only lightly abraded (3-4 hours) with no pyrite, resulting in matte, rounded crystals. After abrasion, the crystals were carefully removed from the abrader by tipping it over a glass Petri dish and giving the abrader a slight tap. Any crystals that remained in the abrader were washed into the Petri dish with ethanol. Care was taken to check the abrader mesh for any crystals that may have clung to it by rinsing it into the Petri dish

with ethanol. The ethanol in the Petri dish was carefully decanted and replaced with HNO_3, after which it was placed on a hotplate to dissolve the pyrite. After complete pyrite dissolution, aliquots of distilled H_2O were repeatedly added to the Petri dish, decanting after each addition. Care was taken not to add distilled H_2O while decanting (the extra turbulence could cause the crystals to go over the side of the Petri dish). This process was repeated with ethanol. The abraded crystals were then examined by binocular microscope again, and the final selection made for analysis.

The crystals selected for abrasion were usually clear grains completely devoid of inclusions, cracks and cores. However, this was not possible in some samples due to generally poor quality of zircon/titanite, especially in the case of gabbros, where the zircons were largely fractured or carried inclusions with only few clear zones. Other samples contained potentially good quality large zircons that had either one or two surficial inclusions or elongate inclusions that stretched the crystal's length. In these cases it proved advantageous to abrade these crystals, since the abrasion process removes a proportion of the outer zircon, and also often cleaved the crystal along the length of the inclusion. Abrasion also removed any surface impurities or highly cracked zones. This yielded satisfactory abraded zircon fragments.

C.1.6 Mineral cleaning:

The zircons/ sphenes were transferred to ~2 ml glass vials with 2-4 drops of distilled H_2O. The vial was then topped up with 8 N HNO_3 and placed on a hotplate at 100°C for 20-30 min. After heating, the vial was held in an ultrasonic bath for a few tens of seconds, and then gently tapped with a pair of scissors. As much as possible of the HNO_3 was removed with a pipette. The vial was filled with distilled H_2O and the process repeated twice more with acetone. The aim of the cleaning was to remove any sulphide (or other coatings) that may still adhere to the crystal surface, and to loosen the crystals in the vial.

C.1.7 Weighing, spiking and dissolution:

The glass vial was gently tipped over into a pre-zeroed aluminium foil 'boat'. Using a pair of fine tweezers, the boat was placed on a Mettler Toledo microbalance, and the weight measured to an accuracy of 1 µg. One drop 8 N HNO_3 was added to a cleaned Teflon® bomb. The weighed aluminium foil 'boat' was gently tipped over the bomb using tweezers to transfer the minerals to the bomb, followed by 12 drops 48% HF. Throughout the weighing, no two vials or

bombs were open at the same time, and all surfaces were cleaned to avoid cross-contamination between samples. Care was taken to avoid any hand movements directly across an open bomb in an attempt to keep common Pb contamination to a minimum. The same procedures were followed for titanite. Titanite, however, does not require such high temperatures for dissolution and was transferred into 3 ml Savillex® rounded screw cap vials after weighing. An in-house artificial $^{205}Pb/^{235}U$ spike was added to the Teflon® and Savillex® bombs before closing them fully.

The sealed Teflon® bombs were dressed in Teflon® jackets and enclosed in a Monel-alloy metal sleeve capped top and bottom with a dual Teflon®-metal puck. The metal sleeves were placed on a metal carousel (six sleeves per carousel) and secured by hand tightened screws. The carousel was placed in an oven for 4-6 days at 191°C. After 4-6 days, the bombs were removed and the HF-HNO_3 evaporated. It was extremely important that all the HF-HNO_3 evaporated, since HF forms fluoride complexes with U and Pb that can hinder full equilibration of sample and spike, causing subsequent incorrect measurements. Fluoride complexes of U and Pb are also undesirable because they do not form temporary bonds with ions exchange resins, which leads to improper separation (see following section). Ten drops of 3 N HCl were added to the bombs after evaporation, and the bombs were placed back in the carousel overnight at ~191°C. HCl acts to dissociate any fluoride complexes that may have formed during the dissolution. The Savillex® vials were placed on a hotplate at ~120°C for 3-4 days, followed by HF-HNO_3 evaporation. Ten drops 3 N HCl were added to the Savillex® vials, after which they were placed back on the hotplate overnight at ~120°C.

C.1.8 Ion exchange columns:

Analytical grade AG 1-X8 Cl-form anion exchange resin (200-400 mesh) was used in the columns.

The ion exchange columns were based on the design of Krogh (1973). The columns are made from 1:4 heat shrinkable Teflon® FEP tubing with ~15 x 2 mm resin beds and ~10 x 10 mm loading chambers. The resin beds were terminated by porous polyethylene frits to keep the resin in place, and the columns were stored in HCl. Before clean resin was added, the columns were thoroughly rinsed with distilled H_2O to remove any residual resin from previous separations, and to check for air bubbles. From this point forwards it became important to ensure that only extremely clean H_2O was used. H_2O, HF and HCl

were triple distilled in-house by sub-boiling, and the common Pb levels measured with a Finnigan MAT 262 Mass Spectrometer with thermal source ionisation (≤1 ppt Pb and 0.1 ppt U, F. Corfu, 2004). The resin was added while the column was still full of water to ensure that no air bubbles formed. If air bubbles were present and large enough, they could disrupt the flow rate or even lead to improper separation. Distilled H_2O, 6 N HCl and 8 N HNO_3 were added to the columns in sequential steps (Krogh, 1973). Care was taken not to make any hand movements over the columns to avoid common Pb contamination. The columns were rinsed on the outside to avoid any spilt resin from falling into the sample during elution, as this leads to improper ionisation and inaccurate measurements. Column and resin preparation was the same for both zircon and titanite.

The samples were loaded onto the columns and allowed to settle for a few minutes. For zircon, Zr, Hf and the REEs were eluted out first with a four-step elution with 3 N HCl. This eluant was received in a centrifuge tube. The U + Pb were then eluted into the Teflon® bombs with a three-step elution with 1x 6 N HCl and 2x distilled H_2O. A drop of H_3PO_4 was added to the bomb, after which it was placed on the hotplate at ~100°C. Under these conditions, HCl and H_2O evaporate, leaving behind the H_3PO_4 which forms a small droplet that contains the U + Pb. Because titanite has larger concentrations of REEs, Ca, Ti, Fe, and Al, it requires more washes with 3 N HCl. This poses problems since U and Pb will elute out with the REEs after about 4-5 washes of HCl (Tremillon, 1965). In order to solve this, 0.5 N HBr is added to the initial eluant, since Br^- increases U and Pb retention on the resin (Tremillon, 1965). Consequently, the REEs in titanite were eluted out with an eight-step elution with 5x [3N HCl + 0.5 N HBr] and 3x 3 N HCl, and the eluant collected in a centrifuge tube. However, since HBr increased the retention time of the U and Pb, it was necessary to elute them out with a four-step elution of 1x 6 N HCl and 3x distilled H_2O compared to the three-step elution for zircon. The eluant was collected in the Savillex® vials. One drop H_3PO_4 was added to the eluant and the Savillex® vial then placed on the hotplate.

The resin (or stationary phase) is composed of silica particles that have polar organic compounds bonded to the surface (Skoog et al., 1996). The organic compounds are bonded by reacting organochlorosilanes ($Cl\text{-}Si(Me)_2R$, where Me = methyl, CH_3- and R = straight chain carbon compound) with –OH groups on the silicon particles' surface. For anion exchange, the R-group usually ends in an amine group (amine = carbon compound with N on the terminating C atom).

In order for separation of different analyte anions to take place, the analyte anion must be able to form temporary bonds with the resin. The strength of the temporary bond will determine how long the anion will remain on the resin (retention time). Retention time is ion specific. The ability for these bonds to form depends largely on the respective polarities of the resin and the analyte anions – analyte ions and resins with comparable polarities will form sufficient bonds to ensure separation i.e. polar analyte ions will bond to polar resins and vice versa. If the polarities are not well matched, no bonds will form between the analyte anions and the resin. Consequently no separation will occur and the analyte will elute out. In this regard, it is preferable that the analyte ions are present as Cl^--complexes and not F^--complexes. F^- and Cl^- are 'hard bases' and U^{6+} and Pb^{4+} are 'hard acids' i.e. they are ions with large charge: size ratios and are slightly polarizable, and preferentially bond with each other (Huheey, Keiter & Keiter, 1993). Important to note, however, is that the Cl^--ion is slightly larger (167 pm) than the F^--ion (114.5 pm) and therefore more polarizable (Huheey, Keiter & Keiter, 1993; table 4.4). Since the amine groups on the resin are polar, Cl^--complexes will better match the polarity of the resin than the F^--complexes, and will be separated more thoroughly.

Even though F^-, Cl^-, Pb^{4+} and U^{6+} are all 'hard' ions, there is a tendency for F^- (smaller radius) and U^{6+} (higher oxidation state) to preferentially bond due to their slightly 'harder' natures, compared to Cl^- and Pb^{4+}. Since this has potential to negatively affect the ion exchange chemistry, it is crucial to ensure that both the U and Pb are present as Cl^--complexes before commencement of ion exchange chromatography. The evaporation of HF-HNO_3 after dissolution and the addition of HCl swamps the analyte ion/spike mixture with Cl^--ions, forcing the formation the Cl^--complexes.

The ion exchange process is based on equilibrium exchange between the ions in the mobile phase or eluant and the stationary phase (the resin), represented by

$$xRN(CH_3)_3^+Cl^- + A^{x-} \leftrightarrow [RN(CH_3)_3^+]_xA^{x-} + xCl^-$$

where x = integer and A = anion. When the sample is initially loaded onto the column, the anions (in the mobile phase) exchange with the Cl^- on the resin and form temporary bonds. The number of Cl^--ions that are expelled from the resin is 1:1 with the valence of the anion. The larger the valence of the anion, the stronger it will be held on the resin and the longer it will take to elute out of the column. When the eluant is added to the column (HCl), the Cl^--ion from the dissociation of HCl competes with the analyte anions on the resin, and eventually replaces them. Once the Cl^--ion replaces the analyte anion, it passes down the column and is eluted out.

C.1.9 Filament loading:

New Re-filaments were outgassed prior to use by passing currents of 1.0, 2.0, and 3.0 A through each filament for 20 minutes, and finally 3.5 A for 1 minute to remove any dust/other contaminants. The filaments were then attached to the sample turret (carries 13 samples) of the mass spectrometer. One drop of SiO_2-gel was mixed in with the spiked sample and the sample-SiO_2 mixture then carefully loaded onto the filament with a pipette. A 1-1.5 A current was run

through the filament until a small trail of smoke appeared. The filament was covered with a metal plate with a slit opening along the entire length of the filament.

C.2 Isotope Dilution Thermal Ionisation Mass Spectrometry (ID-TIMS)

A Finnigan MAT 261 Mass Spectrometer with thermal source ionisation was used for the measurements. The sample chamber was pumped down with a dual turbo and rotary pump, and the flight tube by two ion pumps. The ideal sample chamber pressure was around 10^{-7} atm.

Measurements were taken in several blocks (each block containing 20 analyses) on both Faraday cups and Secondary Electron Multiplier (SEM). The Faraday cups were only used if the smallest signal from the sample was >3-4 mV (10^{-13} A) (relatively larger U and Pb concentrations and stronger intensities). Data were collected separately for the U and Pb systems. Four Faraday cups were in use, which allowed for the simultaneous measurement of all isotopes of either U or Pb. Pb is measured as Pb^{+} ions with atomic masses Pb 204, 206, 207 and 208. U oxidises readily and is measured as UO_2^{2+} ions with molecular masses of 267 (for ^{235}U) and 270 (for ^{238}U). The alignment and spacing of the Faraday cups was periodically checked since improper alignment could lead to a decrease in the intensity and incorrect measurements. In addition, the beam was centred at the beginning of each set of measurements by 'scanning' the ion beam across the entrance of the cups. This was achieved through changing the high voltage, thereby changing the flight path of the ion beam. The highest intensity measured during this process corresponds to the peak flight angle. The Faraday cups generally gave better precision compared to the SEM, because the former are used to measure larger concentrations (larger intensities). The SEM only has a single collector and can measure one isotope at a time. A discrepancy of ~1‰ (although it can be larger) exists between Faraday cups and SEM measurements – it is uncertain as to why the discrepancy exists or what causes it. Subsequently, the measurements from the SEM are corrected according to an empirical formula based on standard measurements. The reproducibility of the measurements for both Pb and U on the Faraday cups is estimated at ± 0.06% /AMU and ± 0.1% /AMU on the SEM.

NBS 982 Pb + U 500 (Catanzaro *et al.*, 1968) was used as standard reference at the beginning of each set of TIMS measurements to gauge the stability of operating conditions in the TIMS.

A mass spectrometer precisely measures isotopic ratios by accelerating isotopes along a curved flight path that passes through an electromagnetic field. The electromagnetic field separates the isotopes based on differences in weight as determined by the equation,

$$\frac{m}{e} = \frac{B^2 r^2}{2V}$$

where m = the atomic mass of the isotope (neutrons + protons), e = charge on the isotope, B = magnetic field strength, r = radius of the flight path of the particular isotope and V = potential difference applied over the flight tube (Faure, 1986). From the equation it is apparent that the mass and flight path radius of any isotope are directly proportional. For example, ^{204}Pb will have a smaller flight path radius than heavier ^{206}Pb. Individual isotopic masses are measured and the ratios computed. The ratios are determined by comparing the intensities of the different isotopic masses to a reference isotope (the spike) of which a known quantity is added to the sample.

C.3 Data conversion and error analysis:

For each sample, measurements were taken in several blocks, each block containing 20 analyses. Mean (M) values, standard deviation (SD) and 2σ-errors (2σE) were determined at the end of each block (based only on analyses that fell within statistical probability). The M, SD and 2σE values from each block were combined at the end of the complete sample run to give total values for the sample run (based on ~20 analyses x number of blocks).

The $^{207}Pb/^{235}U$, $^{206}Pb/^{238}U$ and $^{207}Pb/^{206}Pb$ ages and associated uncertainties were computed with Romage 5.3. Error estimates on the input data for the calculations were given as 0.001 mg for sample weight and 0.1 mg for spike weight. The programme also calculated [U], $[Pb]_{total}$, $[Pb]_{common}$, $[Th]_{model}$, Th/U_{model}, discordance (%) and Rho. Final errors are calculated by propagating all sources of uncertainty and quadratically adding the resulting deviations. Line fitting and plotting was done with Isoplot (Ludwig, 2003). A full breakdown of the data reduction process is given in Appendix D.

C.4 Cathodoluminescence (CL) imaging

For this study a Jeol SEM with CL-detector was used due to the small crystal size of some of the zircons (a few tens of microns). The zircon crystals were mounted in resin on thin section slides and polished down to roughly half the width of the zircon, followed by carbon coating for conductance. Black and white photographs of relative CL intensity were taken of each crystal. Due to time restrictions, CL images were only taken after the ID-TIMS analyses as a

means to clarify discordant data. Where the samples showed concordant data no CL images were deemed necessary.

When an energetic ray (e.g. ion or electron beam) bombards a mineral, the electrons of the crystal's constituent atoms are excited to a higher energy level (Skoog et al., 1996; Potts, 1987). This excited atomic state is inherently unstable, and the electrons soon decay back to their groundstate. The decay is accompanied by an emission of energy proportional to the magnitude of the fallback of the electrons to the groundstate. When the energy is emitted in the visible light region the mineral is said to be fluorescent (emission time $<10^{-8}$s) or luminescent (emission time $>10^{-8}$s) (Curie, 1960). CL uses an electron beam to excite constituent atoms of minerals, compared to radioluminescence (x-ray source) or ionoluminescence (ion-beam source) (Skoog et al., 1996).

Cathodoluminescence in minerals may be inherent to a crystal composition and structure, or may be caused by defects that include anomalies such as impurities/ substitution or broken Si-O bonds, and solid solution (Ramseyer & Mullis, 2000). In inherent luminescence, a variety of cations are potential activators, and the emission wavelength of the activator is determined by its cation position. In zircon the most important CL activators include Ce^{3+}, Pr^{3+}, Gd^{3+} and Ho^{3+} (Ramseyer & Mullis, 2000).

CL is a particularly useful tool for distinguishing different generations of a mineral or internal structure (such as zoning) in a fair number of minerals, including zircon (Corfu et al., 2003; Ramseyer & Mullis, 2000; Kempe et al, 2000). Differences in concentrations of trace elements (potential luminescence centres) between different zones in zircon (and subsequent differences in CL) allow for detailed study of phenomena such as oscillatory growth zoning (OGZ), sector zoning and core-and-rim complexes (e.g. Corfu et al., 2000). In the latter type of study CL (especially when combined with backscatter electron images, BSE) proves invaluable in the recognition of cores that would lead to discordant data and which may otherwise be invisible under normal binocular studies (e.g. Kempe et al., 2000; Poller, 2000).

Appendix D - Data Reduction & Standards

(Adapted from F. Corfu lab notes)

D.1 Data reduction:

D.1.1 Fractionation correction, U:

$$\left(\frac{^{238}U}{^{235}U}\right)_f = \left(\frac{^{238}U}{^{235}U}\right)_{measured} \times \left(1+3\left(\frac{0.1\%/AMU}{100}\right)\right)$$

where 0.1%/*AMU* = the percentage fractionation for U per atomic mass unit

D.1.2 Total ^{238}U in sample:

$$\therefore [^{238}U]_f(nanomols) = \left(\frac{\left(\frac{^{238}U}{^{235}U}\right)_f - \left(\frac{^{238}U}{^{235}U}\right)_{spike}}{1-\frac{\left(\frac{^{238}U}{^{235}U}\right)_f}{\left(\frac{^{238}U}{^{235}U}\right)_{today}}} \right) \times \left(\frac{[^{235}U]_{spike}(ng/g)}{235.0439 g/mol}\right) \times W_{sp}(mg)$$

$$\therefore [^{238}U]_f(nanomols) = \left(\frac{\left(\frac{^{238}U}{^{235}U}\right)_{f,sample}}{1-\frac{\left(\frac{^{238}U}{^{235}U}\right)_f}{\left(\frac{^{238}U}{^{235}U}\right)_{today}}} \right) \times \left(\frac{[^{235}U]_{spike}(ng/g)}{235.0439 g/mol}\right) \times W_{sp}(mg)$$

where $\left(\frac{^{235}U}{^{238}U}\right)_{spike}$ = 1429; $\left(\frac{^{235}U}{^{238}U}\right)_{today}$ = 137.88; $[^{235}U]_{spike}$ = 586.00 ng/g;

W_{sp} = Spike weight

D.1.3 Total ^{235}U in sample:

$$[^{235}U]_f(nanomols) = \frac{[^{238}U]_f(nanomols)}{\left(\frac{^{238}U}{^{235}U}\right)_{today}}$$

D.1.4 Fractionation correction, Pb:

$$\left(\frac{^{207}Pb}{^{206}Pb}\right)_f = \left(\frac{^{207}Pb}{^{206}Pb}\right)_{measured} \times \left(1 + \left(\frac{0.05\%/AMU}{100}\right)\right)$$

$$\left(\frac{^{207}Pb}{^{205}Pb}\right)_f = \left(\frac{^{207}Pb}{^{205}Pb}\right)_{measured} \times \left(1 + 2\left(\frac{0.05\%/AMU}{100}\right)\right)$$

$$\left(\frac{^{207}Pb}{^{208}Pb}\right)_f = \left(\frac{^{207}Pb}{^{208}Pb}\right)_{measured} \times \left(1 - \left(\frac{0.05\%/AMU}{100}\right)\right)$$

$$\left(\frac{^{207}Pb}{^{204}Pb}\right)_f = \left(\frac{^{207}Pb}{^{204}Pb}\right)_{measured} \times \left(1 + 3\left(\frac{0.05\%/AMU}{100}\right)\right)$$

where $0.05\%/AMU$ = the percentage fractionation for Pb per atomic mass unit.

Please note that for Pb, percentage fractionation per AMU is 0.05% if measured using Faraday cups, and 0.1% if measured with the Secondary Electron Multiplier.

D.1.5 Total Pb in sample:

$$[^{205}Pb]_f\,(nanomols) = \left(\frac{[^{205}Pb](ng/g)}{204.974 g/mol}\right) \times \left(\frac{W_{sp}(mg)}{1000}\right)$$

$$[^{206}Pb]_f\,(nanomols) = \left(\frac{^{207}Pb}{^{205}Pb}\right)_f \times \left(\frac{[^{205}Pb](nanomols)}{\left(\frac{^{207}Pb}{^{206}Pb}\right)_f}\right)$$

$$[^{207}Pb]_f\,(nanomols) = [^{205}Pb](nanomols) \times \left(\frac{^{207}Pb}{^{205}Pb}\right)_f$$

$$[^{208}Pb]_f\,(nanomols) = [^{207}Pb]_f\,(nanomols) \times \left(\frac{^{207}Pb}{^{208}Pb}\right)_f$$

$$[^{204}Pb]_f\,(nanomols) = \frac{[^{207}Pb]_f\,(nanomols)}{\left(\frac{^{207}Pb}{^{204}Pb}\right)_f}$$

where [^{205}Pb] = 4.28 ng/g

D.1.6 Removal of spike contribution:

$$[^{206}Pb]_{f,s}(nanomols) = [^{206}Pb]_{f}(nanomols) - \left(\frac{[^{205}Pb]_{f}(nanomols)}{\left(\frac{^{205}Pb}{^{206}Pb} \right)_{spike}} \right)$$

$$[^{207}Pb]_{f,s}(nanomols) = [^{207}Pb]_{f}(nanomols) - \left(\frac{[^{205}Pb](nanomols)}{\left(\frac{^{205}Pb}{^{207}Pb} \right)_{spike}} \right)$$

$$[^{208}Pb]_{f,s}(nanomols) = [^{208}Pb]_{f}(nanomols) - \left(\frac{[^{205}Pb](nanomols)}{\left(\frac{^{205}Pb}{^{208}Pb} \right)_{spike}} \right)$$

$$[^{204}Pb]_{f,s}(nanomols) = [^{204}Pb]_{f}(nanomols) - \left(\frac{[^{205}Pb](nanomols)}{\left(\frac{^{205}Pb}{^{204}Pb} \right)_{spike}} \right)$$

where $\left(\frac{^{205}Pb}{^{206}Pb} \right)_{spike} = 6670$; $\left(\frac{^{205}Pb}{^{207}Pb} \right)_{spike} = 7590$; $\left(\frac{^{205}Pb}{^{208}Pb} \right)_{spike} = 3190$; $\left(\frac{^{205}Pb}{^{204}Pb} \right)_{spike} = 28{,}000$

D.1.7 Removal of blank contribution to sample:

Calculation of blank ^{206}Pb composition

$$B = \left(\frac{^{207}Pb}{^{206}Pb} \right) + \left(\frac{^{208}Pb}{^{206}Pb} \right) + 1 + \left(\frac{1}{\left(\frac{^{206}Pb}{^{204}Pb} \right)} \right)$$

$$\therefore B = \frac{^{207}Pb + ^{208}Pb + ^{206}Pb + ^{204}Pb}{^{206}Pb}$$

$$[^{206}Pb]_{bl}(nanomol) = \frac{[Pb]_{bl}(pg)}{1000(205.9745 g/mol)(B)}$$

$$\therefore [^{206}Pb]_{bl}(nanomol) = \frac{[^{207}Pb + ^{208}Pb + ^{206}Pb + ^{204}Pb]_{bl}(pg)[^{206}Pb]_{bl}}{1000(205.9745g/mol)[^{207}Pb + ^{208}Pb + ^{206}Pb + ^{204}Pb]_{bl}}$$

$$\therefore [^{206}Pb]_{bl}(nanomol) = \frac{[^{206}Pb](pg)}{1000(205.9745g/mol)}$$

where B = total blank Pb expressed as a ratio to $^{206}Pb_{blank}$; $\left(\frac{^{206}Pb}{^{204}Pb}\right) = 18.3$;

$$\left(\frac{^{207}Pb}{^{206}Pb}\right) = 15.555 \text{ ; } \left(\frac{^{208}Pb}{^{206}Pb}\right) = 2.056$$

$$[^{206}Pb]_{f,s,bl}(nanomols) = [^{206}Pb]_{f,s}(nanomols) - [^{206}Pb]_{bl}(nanomols)$$

$$[^{207}Pb]_{f,s,bl}(nanomols) = [^{207}Pb]_{f,s}(nanomols) - \left([^{206}Pb]_{bl} \times \left(\frac{^{207}Pb}{^{206}Pb}\right)_{blank}\right)(nanomols)$$

$$[^{208}Pb]_{f,s,bl}(nanomols) = [^{208}Pb]_{f,s}(nanomols) - \left([^{206}Pb]_{bl} \times \left(\frac{^{208}Pb}{^{206}Pb}\right)_{blank}\right)(nanomols)$$

$$[^{204}Pb]_{f,s,bl}(nanomols) = [^{204}Pb]_{f,s}(nanomols) - \left([^{206}Pb]_{bl} \times \left(\frac{^{204}Pb}{^{206}Pb}\right)_{blank}\right)(nanomols)$$

D.1.8 Removal of initial Pb:

Calculation of Stacey & Kramers (1975) initial Pb

$$\left(\frac{^{206}Pb}{^{204}Pb}\right)_{SK}(nanomols) = \left(\frac{^{206}Pb}{^{204}Pb}\right)_{initial} + \left(\frac{^{238}U}{^{204}Pb}\right)(e^{\lambda_1 \times 10^9 T} - e^{\lambda_1 \times 10^9 SK})$$

$$\left(\frac{^{207}Pb}{^{204}Pb}\right)_{SK}(nanomols) = \left(\frac{^{207}Pb}{^{204}Pb}\right)_{initial} + \left(\frac{\left(\frac{^{238}U}{^{204}Pb}\right)}{\left(\frac{^{238}U}{^{235}U}\right)_{today}}\right)\left(e^{\lambda_2 \times 10^9 T} - e^{\lambda_2 \times 10^9 SK}\right)$$

$$\left(\frac{^{208}Pb}{^{204}Pb}\right)_{SK}(nanomols) = \left(\frac{^{208}Pb}{^{204}Pb}\right)_{initial} + \left(\frac{^{232}Th}{^{204}Pb}\right)\left(e^{\lambda_3 \times 10^9 T} - e^{\lambda_3 \times 10^9 SK}\right)$$

Where $\left(\frac{^{206}Pb}{^{204}Pb}\right)_{initial} = 11.152$; $\left(\frac{^{238}U}{^{204}Pb}\right) = 9.74$; $\left(\frac{^{207}Pb}{^{204}Pb}\right)_{initial} = 12.998$; $\left(\frac{^{208}Pb}{^{204}Pb}\right)_{initial} = 31.23$; $\left(\frac{^{232}Th}{^{204}Pb}\right) = 37.19$; $\lambda_1 = 1.55125\text{x}10^{-10}$; $\lambda_2 = 9.8485\text{x}10^{-10}$; $\lambda_3 = 4.9475\text{x}10^{-11}$; *SK* = Estimated age for the Stacey & Kramers (1975) Pb-isotope evolution model ; $T = 3.70$ Ga

$$[^{206}Pb]_{f,s,bl,i}(nanomols) = [^{206}Pb]_{f,s,bl}(nanomols) - \left([^{204}Pb]_{f,s,bl} \times \left(\frac{^{206}Pb}{^{204}Pb}\right)_{SK}\right)(nanomols)$$

$$[^{207}Pb]_{f,s,bl,i}(nanomols) = [^{207}Pb]_{f,s,bl}(nanomols) - \left([^{204}Pb]_{f,s,bl} \times \left(\frac{^{207}Pb}{^{204}Pb}\right)_{SK}\right)(nanomols)$$

$$[^{208}Pb]_{f,s,bl,i}(nanomols) = [^{208}Pb]_{f,s,bl}(nanomols) - \left([^{204}Pb]_{f,s,bl} \times \left(\frac{^{208}Pb}{^{204}Pb}\right)_{SK}\right)(nanomols)$$

D.1.9 Calculation of U-Pb ratios and ages:

$$\frac{^{206}Pb}{^{238}U} = \frac{[^{206}Pb]_{f,s,bl,i}}{[^{238}U]_f} \qquad \frac{^{207}Pb}{^{235}U} = \frac{[^{207}Pb]_{f,s,bl,i}}{[^{235}U]_f}$$

$$t_{\left(\frac{^{206}Pb}{^{238}U}\right)} = \ln\left(\frac{\left(\left(\frac{[^{206}Pb]_{f,s,bl,i}}{[^{238}U]_f}\right)+1\right)}{\lambda_1 x10^6}\right) \qquad t_{\left(\frac{^{207}Pb}{^{235}U}\right)} = \ln\left(\frac{\left(\left(\frac{[^{207}Pb]_{f,s,bl,i}}{[^{235}U]_f}\right)+1\right)}{\lambda_2 x10^6}\right)$$

D.1.10 Calculation of $^{207}Pb/^{206}Pb$ ratio and age:

$$\frac{^{206}Pb}{^{207}Pb} = \frac{[^{207}Pb]_{f,s,bl,i}}{[^{206}Pb]_{f,s,bl,i}}$$

Calculation of the $^{207}Pb/^{206}Pb$ is a reiterative procedure:

$$Ra = \frac{\left(\frac{\{^{206}Pb\}_{f,s,bl.i}}{[^{238}U]_f}\right)}{\left(\frac{[^{207}Pb]_{f,s,bl.i}}{[^{235}U]_f}\right)}$$

$$A = starting\ age\ estimate$$

$$F_1 = \left(e^{(\lambda_1 \times 10^6 \times A)} - Ra\right) \times \left(e^{(\lambda_2 \times 10^6 \times A)} + Ra\right) - 1$$

$$F_2 = \left(\left(\lambda_1 \times 10^6\right) \times e^{(\lambda_1 \times 10^6 \times A)}\right) - \left(\left(\left(\lambda_2 \times 10^6\right) + Ra\right) \times e^{(\lambda_2 \times 10^6 \times A)}\right)$$

$$AA = A - \frac{F_1}{F_2}$$

The calculation is repeated until $|AA\text{-}A| < 0.01$

D.1.11 Calculation of concentrations:

$$[U](ppm) = \frac{\left([^{238}U]_f (nanomols) 238.0508 g/mol\right) + \left([^{235}U]_f (nanomols) 235.0439 g/mol\right)}{W_{sp}(mg)}$$

$$[Pb]_{radiogenic}(ppm) = \frac{\left(\begin{array}{l}\left([^{206}Pb]_{f,s,bl.i} (nmols) 203.973 g/mol\right) \\ + \left([^{207}Pb]_{f,s,bl,i} (nmols) 206.9759 g/mol\right) \\ + \left([^{208}Pb]_{f,s,bl,i} (nmols) 207.9767 g/mol\right)\end{array}\right)}{W_{sp}(mg)}$$

D.1.12 Calculation of total Common Pb (max. value for Pb-blank):

$$\begin{aligned} Pb_{common}(pg) &= [^{204}Pb]_{f,s} (nmols) 203.973 g/mol \\ &+ \left([^{204}Pb]_{f,s} (nmols) \times \left(\frac{^{206}Pb}{^{204}Pb}\right)_{blank}\right) 205.9745 g/mol \\ &+ \left([^{204}Pb]_{f,s} (nmols) \times \left(\frac{^{206}Pb}{^{204}Pb}\right)_{blank} \times \left(\frac{^{207}Pb}{^{206}Pb}\right)_{blank}\right) 206.9759 g/mol \\ &+ \left([^{204}Pb]_{f,s} (nmols) \times \left(\frac{^{206}Pb}{^{204}Pb}\right)_{blank} \times \left(\frac{^{208}Pb}{^{206}Pb}\right)_{blank}\right) 207.9767 g/mol \end{aligned}$$

D.1.13 Calculation of percentage discordance:

Calculated from the $^{206}Pb/^{238}U$ and $^{207}Pb/^{206}Pb$ ages along a line to 0 Ma.

$$\%Discordance = 100 \times \left(\left(\frac{^{207}Pb}{^{206}Pb}\right)^{age} - \left(\frac{^{206}Pb}{^{238}U}\right)^{age}\right)$$

D.2 Standard:

A single sample of zircon standard 91500 (Wiedenbeck *et al.*, 1995) was analysed as an internal check for the preparation sequence. Values obtained for

91500 by the author yielded errors that are consistently one order of magnitude larger than those obtained by Wiedenbeck *et al.* (1995). Published values for 91500 and values measured by the author are given in table B-1. The chief source for the larger errors appears to be a generally smaller measured U concentration (~53 ppm in the analysed samples vs. 81.2 ppm in the standard) and radiogenic Pb (suggested by a smaller $^{206}Pb/^{204}Pb$ ratio). However, the almost identical $^{207}Pb/^{206}Pb$ and U-Pb ratios, as well as U-Pb and $^{207}Pb/^{206}Pb$ ages suggest fairly similar levels of contamination.

Appendix E - Additional Theory: Zircon, Titanite and U-Th-Pb systematics

E.1 – Zircon:

Zircon is a fairly common accessory mineral in igneous rocks, occurring more commonly in acid and alkali plutons than in mafic rocks. Primary magmatic zircon is generally characterised by euhedral crystals (Corfu *et al.*, 2003) of which the morphology is a combination of {100}/{110} prism and {101}/{211}/{301} pyramidal faces (Pupin, 1981; Corfu *et al.*, 2003; figure D-1). Simple prismatic morphologies are usually dominated by one of each prism and pyramidal faces, and specific combinations of faces appear to be associated with specific melt compositions. For instance, zircon crystals from relatively dry, alkalic and tholeiitic melts are dominated by {100} and {101} faces, while pegmatites and water-rich granites tend to have dominant {110} and {101} faces (Corfu *et al.*, 2003; Pupin, 1981). In prisms with a complex morphology, more than one prism and pyramidal face is present (e.g. {100} + {110} and {101} + {211}), giving the crystal a rounded appearance (figure D-1). Length: width ratios are thought to be an indication of growth rate, where ratios >1:3 indicate fairly fast crystallisation and ≤1:3 fairly slow (Corfu *et al.*, 2003). Magmatic zircon is usually characterised by well defined oscillatory growth zones (OGZ) under CL, and may also develop sector zoning that cuts across the OGZs (Corfu *et al.*, 2003).

Zircon can also be produced under metamorphic conditions, either as 1) crystals grown from an anatectic melt, or 2) crystals grown from subsolidus processes such as the release of Zr from Zr-bearing minerals through metamorphic reactions or recrystallisation of existing zircons. The first instance requires that a small reservoir of melt exists that is capable of crystallising zircon. Where melting is in an incipient stage with only small volumes of melt, zircons crystallise along grain boundaries of existing minerals and have acicular morphologies with little or no development of the pyramidal terminations (Schaltegger *et al.*, 1999). However, if sufficient pools of melt exist, normal euhedral magmatic zircons will develop (Schaltegger *et al.*, 1999; Corfu *et al.*, 2003). In this case the zircons are usually enclosed in melt-mineral phases such as feldspars and quartz (e.g. Schaltegger *et al.*, 1999). Zircon grown during anatexis may also grow as rims around pre-existing zircon grains. Sources of Zr during melting include inherited zircon that is resorbed by the melt (Watson & Harrison, 1983), biotite (Vavra *et al.*, 1996), garnet and amphibole (Fraser *et al.*, 1997). Evidence suggests that zircon is more likely to crystallise early in an

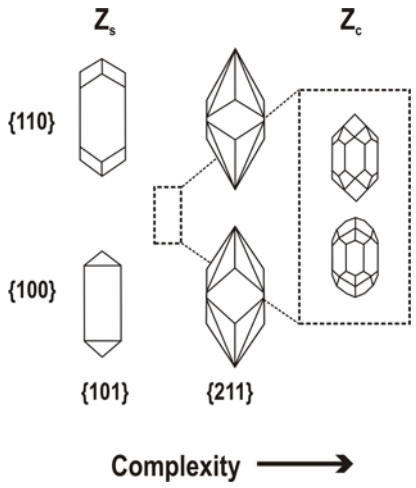


Figure E-1 Schematic diagrams of common zircon morphologies. Zircons with simple prismatic morphologies are dominated by either the {100} or {110} prismatic faces, and commonly have either the {101} or {211} pyramidal terminations. When both of the respective prismatic and pyramidal faces are present in roughly equal proportions, the prism is said to have a complex morphology. ***(After Pupin, 1981; adapted from Corfu,* et al., *2003)***

anatectic melt since: a) the composition of the initial melt is felsic, implying a lower Zr-solubility (Watson & Harrison, 1983) and b) the small amount of melt would be easily supersaturated in Zr. Further production of anatectic melt would be less Zr-saturated and more mafic in composition, thereby allowing less or no zircon to crystallise and will eventually partially/wholly resorb the early zircons (Vavra *et al.*, 1996). With subsolidus growth, zircons can be grown through the net-transfer of Zr from the metamorphic breakdown of Zr-bearing phases (e.g. amphibole and garnet) (Fraser *et al.*, 1997; Degeling *et al.*, 2001) without necessarily involving a fluid phase. Breakdown reactions of this nature are common in high-grade (upper-amphibolite/granulite) rocks and include (Fraser *et al.*, 1997):

1) $2Fe_3Zr_2Al_2Si_2O_{12} + 4Al_2SiO_5 + 13SiO_2 \rightarrow 3Fe_2Al_4Si_5O_{19} + 4ZrSiO_4$

garnet + sillimanite + quartz → cordierite + zircon

2) $2Fe_3Zr_2Al_2SiO_{12} + 11SiO_2 \rightarrow Fe_2Al_4Si_5O_{18} + 4FeSiO_3 + 4ZrSiO_4$

garnet + quartz → cordierite + opx + zircon

This style of growth yields rounded zircon morphologies (Schaltegger *et al.*, 1999) that occur within the reaction rims surrounding the garnets (Fraser *et al.*, 1997). However, the growth of zircon under these conditions is controlled by the solubility of Zr into the product phases. If Zr is easily accommodated in the crystal structure of one of the daughter phases, then it is unlikely that free

zircon will form (Degeling *et al.*, 2001). For example, in the reaction (Degeling *et al.*, 2001):

$$\text{gnt} + \text{biot} + \text{qtz} + \text{sil} \rightarrow \text{osumilite} + \text{opx} + \text{spinel} + \text{mgt}$$

all the Zr contained in the garnet is accommodated in the opx and osumilite structures, thereby inhibiting the formation of free zircon. Such net-transfer reactions appear capable of producing new zircon as well as nucleating new growth around existing zircons caught in the reaction rims around the Zr-bearing phase (Degeling *et al.*, 2001).

Subsolidus recrystallisation of zircons is not responsible for any new growth, but merely for the reorganisation of the internal crystal structure without any change in external morphology. During this process, however, trace elements and Th and Pb are sequentially expelled from the crystal structure (Hoskin & Black, 2000) thereby yielding discordant ages. In an extreme case the zircon would be completely reset, although this appears to be very rare. Complete recrystallisation takes a long time (Hoskin & Black, 2000) and a limited period of recrystallisation may lead to 'false' metamorphic events since the U-Pb clock has not completely reset. Temperatures lower than amphibolite facies appear to be insufficient to instigate the growth of new metamorphic zircon or internal recrystallisation of existing grains (Fraser *et al.*, 1997; Hoskin & Black, 2000). Zircons that have undergone recrystallisation may show blurring of the primary OGZs, often leading to segments of crystals or whole zircons that show poorly defined growth zoning. These recrystallisation textures may also occur as completely CL-homogeneous patches or 'flow textures', the latter appearing similar to smeared paint or agate-like patterns (e.g. sample NM04-16, figure 4.20b). Recrystallisation textures in zircon are associated with Pb-loss, where the degree of Pb loss is considered proportional to the amount of preservation of the original OGZs (Connelly, 2001).

An important characteristic that makes zircon a useful geochronometer is the ready accommodation of U into its crystal structure during crystallisation through simple substitution of U^{4+} for Zr^{4+}, and the complete exclusion of common Pb (Hoskin & Schaltegger, 2003). More importantly, zircon has a high closure temperature to the diffusion of Pb through its crystal structure, effectively trapping radiogenic Pb. In addition zircon is resistant to weathering (Faure, 1986). This creates a closed system that is highly amenable to geochronological investigations. Since zircon is grown under both metamorphic and igneous conditions it is possible to date these respective events. In this

regard, it is important to determine the origin of the zircon. Besides petrographic associations and zircon morphologies, Th/U ratios in zircons were considered to act as a fingerprint for distinguishing between magmatic and metamorphic zircons (Rubatto & Gebauer, 1999). Th/U ratios of >0.4 are considered magmatic while values <0.1 are considered metamorphic. Values of $0.1 < x < 0.4$ are somewhat obscure and suggested to represent zircon growth during the incipient stages of partial melting before the volumes of melt are sufficient to provide an essentially 'magmatic' environment. However, zircons collected from a plutonic source (e.g. Wiedenbeck *et al.*, 1995; Corfu *et al.*, 2006) have shown values below 0.4 and even as low as 0.1. In addition, Ashwal *et al.* (1999) also observed a spread in Th/U ratios of ~0.2-0.9 in zircons from cogenetic plutons, and concluded that this was a result of fractional crystallisation. Th/U ratios are therefore not used as a diagnostic tool to distinguish zircon with a definite metamorphic overprint from purely 'melt' derived zircon. In accordance with general practise in U-Pb geochronology publications, however, Th/U are noted for all samples. The distinction between metamorphic and magmatic zircon is largely based on petrographic studies (including binocular inspection of crystal morphologies), cathodoluminescence (CL) and backscatter electron (BSE) imaging.

E.2 – Titanite:

Titanite is a common accessory mineral both in primary igneous and metamorphic assemblages. In the former, titanite is abundant in rocks with high bulk Ca content, but less abundant or absent in rocks with high Al activities or low Ca/Al ratios (Frost *et al.*, 2000). Consequently, titanite is generally found in metaluminous I-type diorites and granodiorites, as well as alkali-rocks (Frost *et al.*, 2000). Typical igneous titanite has euhedral morphologies with a distinct diamond-shaped cross-section. Titanite is a common metamorphic mineral in mafic rocks that have undergone mild metamorphism, as well as orthogneisses, calc-silicate rocks and marbles (Frost *et al.*, 2000). Metamorphic titanite generally has a rounded, subhedral diamond-shaped to anhedral cross-section that is easily distinguished from euhedral igneous titanite (Corfu & Stone, 1998). One reason for the abundance of titanite in metamorphic assemblages is the relative abundance of Ca and Ti in rock forming minerals (e.g. ilmenite, feldspar, pyroxene, amphibole, biotite), which is released during metamorphic reactions (Frost *et al.*, 2000; Corfu *et al.*, 1998).

Easy incorporation of U into titanite's crystals structure and a high closure temperature to Pb diffusion (≤700°C; Frost *et al.*, 2000) makes it a useful geochronological tool. Since titanite is readily grown in metamorphic environments, it potentially provides ages for such events, especially where the growth of titanite is visibly associated with the formation of a deformational fabric or metamorphic reactions (Corfu & Stone, 1998). However, titanite reacts easily during high temperature metamorphism in the presence of other Ti-bearing phases (Scott & St. Onge, 1995). Under these circumstances titanite may reset its U-Pb age, and as a result, even remnant primary titanite will date the metamorphic event with little trace of the original magmatic age. In addition, since Pb is also easily accommodated into structure, age data obtained from titanite are prone to large errors due to a large ^{204}Pb component.

E.3 - U-Th-Pb Systematics:

Pb has four natural stable isotopes (Pb 204, 206, 207 and 208) and U three unstable isotopes (U 234, 235 and 238) (Faure, 1986). ^{207}Pb and ^{206}Pb are formed from the radioactive decay of ^{235}U ($\lambda = 9.8485 \times 10^{-10}$) and ^{238}U ($\lambda = 1.55125 \times 10^{-10}$), respectively, via a lengthy chain of intermediate radioactive daughter products, while ^{208}Pb is formed from the radioactive decay of ^{232}Th (Faure, 1986). ^{204}Pb occurs naturally (termed 'common Pb'), and is used as a reference isotope. The age of a rock and initial Pb can be related to the present-day ratios of $^{206}Pb/^{204}Pb$, $^{238}U/^{204}Pb$, $^{207}Pb/^{204}Pb$ and $^{235}U/^{204}Pb$ in a sample through the equation,

$$\left(\frac{^{206}Pb}{^{204}Pb}\right) = \left(\frac{^{238}U}{^{204}Pb}\right)\left(e^{\lambda t - 1}\right) + \left(\frac{^{206}Pb}{^{204}Pb}\right)_i$$

where ($^{206}Pb/^{204}Pb$) and ($^{238}U/^{204}Pb$) are the respective ratios as measured, λ = decay constant, t = age and $(^{206}Pb/^{204}Pb)_i$ = the Pb ratio at the time of mineral closure (Faure, 1986). A similar equation can be written for the $^{235}U/^{204}Pb$-$^{207}Pb/^{204}Pb$ system. If the two decay systems are left undisturbed, they will give the same ages within error and are said to be concordant. If the systems are disturbed in some way the two U-systems may no longer yield the same age and are said to be discordant. This is usually due to Pb loss or the addition of U to either or both the systems. This 'youngs' the age of the rocks since there is less Pb than there should be for the same amount of U at that age.

All the concordant ages throughout Earth's 4.5 Ga history define a non-linear curve called the Concordia (Wetherill, 1956), which plots $^{206}Pb/^{238}U$ vs. $^{207}Pb/^{235}U$. The curve is a function of the decay constants of the two U-Pb systems, and is non-linear due to dissimilar decay constants. The actual curve itself is a thin band because of the uncertainties on the decay constants (Jaffey *et al.*, 1971). If the two U-Pb systems for any sample are concordant, the sample is said to behave as a closed system and the data will plot as a point that overlaps on the concordia curve. However, if the system has suffered any disturbance with subsequent Pb loss or U addition, the system's behaviour is open and the data will plot discordantly. Such discordant data plot in a linear array *below* concordia, and define an upper and lower intercept for which the interpretation differs from sample to sample. In addition to Pb loss, inheritance of radiogenic Pb from an older source will also cause discordant data. Both Pb loss and inheritance yield identical concordia plots, and require further investigation by additional methods (e.g. CL, BSE) to determine the dominant process. Besides Pb-loss and inheritance, exclusion of ^{230}Th (one of the intermediate daughter products of the decay of ^{238}U, which eventually decays to ^{206}Pb) from the zircon structure during crystallization, will also lead to discordant data (Parish & Noble, 2003). On rare occasions, the decay of ^{231}Pa (Protactinium) to radiogenic ^{207}Pb is invoked to account for the horizontal spread of data points on a Concordia diagram due to excess radiogenic ^{207}Pb (Mortensen *et al*, 1992; Anczkiewicz *et al*, 2001).

In addition to the U-Pb isochron and $^{206}Pb/^{238}U$ vs. $^{207}Pb/^{235}U$ concordia ages, $^{207}Pb/^{206}Pb$ ages are also determined from the equation:

$$\left(\frac{^{207}Pb}{^{206}Pb}\right)^{*} = \left(\frac{^{235}U}{^{238}U}\right)\left(\frac{\left(e^{\lambda_2 t}-1\right)}{\left(e^{\lambda_1 t}-1\right)}\right)$$

where $(^{207}Pb/^{206}Pb)^*$ = the ratio of radiogenic Pb, $(^{235}U/^{238}U)$ = the measured ratios of the U-isotopes, λ = the decay constant of the respective U isotopes (Faure, 1986). This equation does not require knowledge of the specific U concentration in the given sample. $^{207}Pb/^{206}Pb$ ages are particularly useful as indicators of old Pb-loss events or inheritance.

References

Akselsen, J. (1982): *Precambrian and Caledonian Tectonometamorphic Evolution of Northeastern Seiland, Finnmark, North Norway;* Norges Geologiske Undersøkelse **373**, p. 45-61.

Anczkiewicz, R., Oberli, F., Burg, J.P., Villa, I.M., Gunther, D. & Meier, M. (2001): *Timing of normal faulting along the Indus Suture in Pakistan Himalaya and a case of Major Pa-231/U-235 initial disequilibrium in zircon*; Earth and Planetary Science Letters, **191**, p. 101-114.

Andersen, T.B. (1984): *The Stratigraphy of the Magerøy Supergroup, Finnmark, North Norway*; Norges Geologiske Undersøkelse, Bulletin, **395**, p. 25-37.

Andersen, T.B. (1981): *The Structure of the Magerøy Nappe, Finnmark, north Norway;* Norges Geologiske Undersøkelse, **363**, p. 1-23.

Andersen, T.B., Austrheim, H., Sturt, B.A., Pedersen, S. & Kjærsrud, K. (1982): *Rb-Sr whole rock ages from Magerøy, north Norwegian Caledonides*; Norsk Geologiske Tidsskrift, **62**, p. 79-85.

Ashwal, L.D., Tucker, R.D. & Zinner, E.K. (1999): *Slow cooling of deep crustal granulites and Pb-loss in zircon;* Geochimica et Cosmochimica, **63 (18)**, p. 2839-2851.

Bailey, D.K. (1992): *Episodic alkaline activity across Africa: Implications for the causes of continental break-up;* In, Storey, B.C. *et al.* (Eds.), Magmatism and the causes of continental break-up; Geological Society of London Special Publication, **68**, p. 91-98.

Bailey, D.K. (1977): *Lithospheric control of continental rift magmatism;* Journal of the Geological Society, London, **133**, p. 103-106.

Bailey, D.K. (1974): *Continental rifting and alkaline magmatism;* In, Sorensen, H. (Ed.), The alkaline rocks; New York, Wiley, p. 148-159.

Burke, K., Ashwal, L.D. & Webb, S.J. (2003): *New way to map old sutures using deformed alkaline rocks and carbonatites;* Geology, **31**, p. 391-394.

Catanzaro, E.J., Murphy, T.J., Shields, W.R., & Garner, E.L. (1968): *Absolute isotopic abundance ratios of common, equal atom, and radiogenic lead isotope standards*; Journal for Research of the U.S. National Bureau of Standards, Section, A, 72, 261-267, 1968.

Connelly, J.N. (2001): *Degree of preservation of igneous zonation in zircon as a signpost for concordancy in U/Pb geochronology*; Chemical Geology, **172**, p. 25-39.

Corfu, F., Torsvik, T.H., Andersen, T.B., Ashwal, L.D., Ramsay, D.M. & Roberts, R.J. (2006): *Early Silurian mafic-ultramafic and granitic plutonism in*

contemporaneous flysch, Magerøy, northern Norway: U-Pb age and regional significance; Journal of the Geological Society, London, **163**, p. 291-301.

Corfu, F. Roberts, R.J., Gerber, M. Torsvik, T.H., Andersen, T.B., Ramsay, D.M. & Ashwal, L.D. (2005a): *Exotic terranes in the Finnmarkian Caledonides: U-Pb evidence for Peri-Gondwanan and Laurentian elements;* Norwegian Geological Winter meeting, Abstracts and Proceedings no. 1, Røros, January, 9-12, 2005, p. 22.

Corfu, F., Hanchar, J.M., Hoskin, P.W.O. & Kinny, P. (2003): *Atlas of Zircon Textures;* Reviews in Mineralogy and Geochemistry, **53**, p. 469-500.

Corfu, F. & Stone, D. (1998): *The significance of titanite and apatite U-Pb ages: Constraints for the post-magmatic thermal-hydrothermal evolution of a batholithic complex, Berens River area, northwestern Superior Province, Canada;* Geochimica et Cosmochimica Acta, **62 (17)**, p. 2979-2995.

Corfu, F., Roberts, R.J., Torsvik, T.H., Ashwal L.D & Ramsay, D.M. (in press): *Peri-Gondwanan elements in the Caledonian nappes of Finnmark, northern Norway: implications for the palæogeographic framework of the Scandinavian Caledonides.*

Curie, D. (1960): *Luminescence cristalline; Dunod, Paris.*

Curry, C.J. (1975): *A Regional Study of the Magerøy basic igneous complex and its envelope*; Unpublished Ph.D thesis, University of Dundee, 244 pp.

Dallmeyer, R.D. (1988): *Polyorogenic $^{40}Ar/^{39}Ar$ mineral age record within the Kalak Nappe Complex, Northern Scandinavian Caledonides*; Journal of the Geological Society, London, **145**, p. 705-716.

Daly, J.S., Aitcheson, S.J., Cliff, R.A., Gayer, R.A. & Rice, A.H.N. (1991): *Geochronological evidence from discordant plutons for a late Proterozoic orogen in the Caledonides of Finnmark, northern Norway;* Journal of the Geological Society, London, **148**, p. 29-40.

Deer, W.A., Howie, R.A. & Zussman, J. (1992): *An introduction to the rock forming minerals, 2nd Ed*; Longman Scientific and Technical.

Degeling, H., Eggins, S. & Ellis, D.J. (2001): *Zr budgets for metamorphic reactions, and the formation of zircon from garnet breakdown;* Mineralogical Magazine, **65 (6)**, p. 749-758.

Dunning, G.R. (1987): *U-Pb zircon ages of Caledonian ophiolites and arc sequences: implications for tectonic setting;* Abstract, Terra Abstr., EUG IV, Strasbourg, 179.

Faure, G. (1986): *Principles of Isotope Geology, 2nd Ed.;* Wiley.

Fraser, G., Ellis, D. & Eggins, S. (1997): *Zirconium abundance in granulite-facies minerals, with implications for zircon geochronology in high-grade rocks;* Geology, **25**, p. 607-610.

Frost, B.R., Chamberlain, K.R. & Schumacher, J.C. (2000): *Sphene (titanite): phase relations and role as a geochronometer;* Chemical Geology, **172**, p. 131-148.

Gayer, R.A., Hayes, S.J. & Rice, A.H.N. (1985): *The structural development of the Kalak Nappe Complex of Eastern and Central Porsangerhalvøya, Finnmark, Norway;* Norges Geologiske Undersøkelse Bull. **400**, p. 67-87.

Hoskin, P.W.O. & Black, L.P. (2000): *Metamorphic zircon formation by solid-state recrystallization of protolith igneous zircon*; Journal of Metamorphic Petrology, **18**, p 423-439.

Hoskin, P.W.O. & Schaltegger, U. (2003): *The composition of zircon and igneous and metamorphic petrogenesis*; In, Hanchar, J.M. & Hoskin, P.W.O. (Eds.), Reviews in Mineralogy & Geochemistry, **53**, p. 27-62.

Huheey, J.E., Keiter, E.A. & Keiter, R.L. (1993): *Inorganic Chemistry: Principles of Structure and Reactivity, 4th Ed.;* Harper Collins.

Jaffey, A. H., Flynn, K.F., Glendenin, L.E., Bentley, W.C & Essling, A.M (1971): *Precision measurements of half-lives and specific activities of ^{235}U and ^{238}U;* Physical Reviews, **C4**, p. 1889-1906.

Kearey, P., Brooks, M. & Hill, I. (2002): *An Introduction to Geophysical Exploration, 3rd Ed.*; Blackwell Science.

Kempe, U., Gruner, T., Nasdala, L. & Wolf, D. (2000): *Relevance of Cathodoluminescence for the Interpretation of U-Pb Zircon Ages, with an Example of an Application to a Study of Zircons from the Saxonian Granulite Complex, Germany*; In, Pagel, M. *et al.* (Eds.), Cathodoluminescence in Geosciences; Springer, p. 415-455.

Kirkland, C.L., Daly, J.S., Eide, E. & Whitehouse, M.J. (2005a): *The Kalak Nappe Complex, arctic Norway: a major revision of its tectonometamorphic history:* Recent developments in the geological history of the British Isles – a tribute to W. Stuart McKerrow, Oxford.

Kirkland, C.L., Daly, J.S., Eide, E. & Whitehouse, M.J. (2005b): *Tectonic events in The Kalak Nappe Complex, arctic Caledonides redefined through a linked structural and geochronological approach*; Geophysical Research Abstracts, **7**, 10097.

Kirkland, C.L. & Daly, J.S. (2003): *Confirmation of the Porsanger Orogeny in the Caledonides of Arctic Norway;* (abstract), Highlands Workshop- May 2003, British Geological Survey, Edinburgh, Abstract volume.

Kirkland, C.L., Daly, J.S. & Whitehouse, M.J. (in press): *Granitic magmatism of Grenvillian and late Neoproterozoic age in Finnmark, Artic Norway – constraining pre-Scandian deformation in the Kalak Nappe Complex;* Precambrian Research.

Krogh, T.E. (1982b): *Improved accuracy of U-Pb zircon dating by selection of more concordant fractions using a high gradient magnetic separation technique;* Geochimica et Cosmochimica Acta, **46** (4), p. 631-635.

Krogh, T.E. (1982a): *Improved accuracy of U-Pb zircon ages by the creation of more concordant systems using an air abrasion technique*; Geochimica et Cosmochimica Acta, **46**, p. 637 – 649.

Krogh, T.E. (1972): *A low-contamination method for hydrothermal decomposition of zircon and extraction of U and Pb for isotopic age determinations*; Geochimica et Cosmochimica Acta, **37**, p. 485 – 494.

Ludwig, K.R. (2003): *Isoplot 3.0. A geochronological toolkit for Microsoft Excel;* Berkeley Geochronology Center Special Publication, **4**, 70 p.

Maeda, J. & Kagami, H. (1996): *Interaction of a spreading ridge and an accretionary prism: Implications from MORB magmatism in the Hidaka magmatic zone, Hokkaido, Japan;* Geology, **24**, p. 31-34.

Meert, J.G. & Torsvik, T.H. (2003): *The making and unmaking of a supercontinent: Rodinia revisited;* Tectonophysics, **375**, p. 261-288.

Mortensen, J.K., Roddick, J.C. & Parrish, R.R. (1992): *Evidence for high levels of unsupported radiogenic ^{207}Pb in zircon from a granitic pegmatite: Implications for interpretation of discordant U-Pb data;* EOS Transcripts, American Geophysical Union, **73**.

Nordgulen, Ø., Bickford, M.E., Nissen, A.L. & Wortman, G.L. (1993): *U-Pb zircon ages from the Bindal Batholith, and the tectonic history of the Helgeland Nappe Complex, Scandinavian Caledonides;* Journal of the Geological Society, **150**, p. 771-783.

Northrup, C.J. (1997): *Timing structural assembly, metamorphism and cooling of Caledonian Nappes in the Ofoten-Efjorden Area, north Norway: Tectonic insights from U-Pb and $^{40}Ar/^{39}Ar$ geochronology;* Journal of Geology, p. 565-582.

Parish, R.R. & Stephen, R.N. (2003): *Zircon U-Th-Pb Geochronology by Isotope Dilution-Thermal Ionization Mass Spectrometer (ID-TIMS);* In, Hanchar, J.M. & Hoskin, P.W.O. (Eds.), Reviews in Mineralogy and Geochemistry, **53**, p. 183-213.

Pedersen, R.B., Nordgulen, Ø., Barnes, C.G., Prestvik, T. & Barnes, M.A. (1999): *U-Pb dates from dioritic and granitic rocks in Velfjord, north-central Norway;* Abstract, Geonytt, 81 (January).

Pedersen, R.B., Dunning, G.R. & Robins, B. (1989): *U-Pb ages of nepheline syenite pegmatites from the Seiland Magmatic Province, north Norway;* In, Gayer, R.A. (Ed.), The Caledonian Geology of Scandinavia; Graham & Trotman, London, p. 3-8.

Poller, U. (2000): *A Combination of Single Zircon Dating by TIMS and Cathodoluminescence Investigations on the Same Grain: The CLC Method - U-Pb Geochronology for Metamorphic Rocks;* In, Pagel, M. *et al.* (Eds.), Cathodoluminescence in Geosciences; Springer, p. 401-413.

Potts, P.J. (1984): *A Handbook of Silicate Rock Analysis;* Blackie, p. 339-340.

Pupin, J.P. (1980): *Zircon and Granite Petrology*; Contributions to Mineralogy and Petrology, **73**, p. 207-220.

Ramsay, D.M. (1971): *The Structure of North West Sørøy*; Abstract, Norges Geologiske Undersøkelse Special Edition, **269**, p. 15-20.

Ramsay, D.M. (1971): *Stratigraphy of Sørøy;* Abstract, Norges Geologiske Undersøkelse Special Edition, **269**, p. 314-317.

Ramsay, D.M. & Sturt, B.A. (1977): *A Sub-Caledonian Unconformity within the Finnmarkian Nappe Sequence and Its Regional Significance*; Norges Geologiske Undersøkelse, **334**, p. 107-116.

Ramsay, D.M. & Sturt, B.A. (1976): *The syn-metamorphic emplacement of the Magerøy Nappe;* Norsk Geologiske Tidsskrif, **56**, p. 291-307.

Ramsay, D.M., Sturt, B.A. & Andersen, T.B. (1979): *The sub-Caledonian unconformity on Hjemsøy – New evidence of primary basement/cover relations in the Finnmarkian Nappe sequence;* Norsk Geologiske Undersøkelse, **351**, p. 1-12.

Ramseyer, K. & Mullis, J. (2000): *Geologic application of Cathodoluminescence of Silicates;* In, Pagel, M. *et al.* (Eds.), Cathodoluminescence in Geosciences; Springer, p. 177-191.

Rice, A.H.N. (1985): *Staurolite growth and metamorphic zones in the Kalak Nappe Complex of north-eastern Porsangerhalvøya, north Norway;* Lithos, **18**, p. 281-294.

Rice, A.H.N. & Frank, W. (2003): *The early Caledonian (Finnmarkian) event reassessed in Finnmark: $^{40}Ar/^{39}Ar$ cleavage age data from NW Varangerhalvøya, N. Norway;* Tectonophysics, **374**, p. 219-236.

Roberts, D. (1974): *Hammerfest. Description of the 1:250 000 geological map;* Norges geologiske Undersøkelse, **301**, 66pp.

Roberts, D. (1973): *Geologisk kart over Norge, berggrunnskart. Hammerfest 1: 250 000;* Norges Geologiske Undersøkelse.

Roberts, D. (1971): *A conspectus of Eocambrian-lower Palæozoic sedimentation on Sørøy;* Abstract, Norges Geologiske Undersøkelse Special Edition, **269**, p. 242-245.

Roberts, D. (1968): *The Structural and Metamorphic History of the Langstrand-Finfjord Area, Sørøy, Northern Norway;* Norges Geologiske Undersøkelse, **253**.

Roberts, D. Melezhik, V.M. & Heldal, T. (2002): *Carbonate formations and NW-directed thrusting in the highest allochthons of the Norwegian Caledonides: evidence of a Laurentian ancestry;* Journal of the Geological Society, London, **159**, p. 117-120.

Roberts, R.J., Corfu, F., Torsvik, T.H., Ashwal, L.D. & Ramsay, D.M. (in press): *Short-lived mafic magmatism at 570 Ma in the northern Norwegian Caledonides – U-Pb zircon ages from the Seiland Igneous Province.*

Roberts, R.J., Corfu, F., Torsvik, T.H., Ramsay, D.M. & Ashwal, L.D. (2004): *Redefining the magmatic evolution of the Kalak Nappe Complex*; Abstract volume, Scandinavian Geological Society Winter Meeting, p. 10.

Robin, L., Cocks, M. & Torsvik, T.H. (2005): *Baltica from the late Precambrian to mid-Palæozoic times: The gain and loss of a terrain's identity;* Earth-Science Reviews, **72 (1-2)**, p. 39-66.

Robins, B. & Gardner, P.M. (1974): *Synorogenic layered basic intrusions in the Seiland Petrographic Province, Finnmark;* Norges Geologiske Undersøkelse, **312**, p. 91-130.

Rubatto, D. & Gebauer, D. (1999): *Eo/Oligocene (35 Ma) high-pressure metamorphism in the Gornergrat Zone (Monte Rosa, Western Alps): implications for palæogeography;* Schweizer. Mineral. Petrogr. Mitt., **79**, p. 353-362.

Schaltegger, U., Fanning, C.M, Günther, D., Maurin, J.C., Schulmann, K. & Gebauer, D. (1999): *Growth, annealing and recrystallization of zircon and preservation of monazite in high-grade metamorphism: conventional and in-situ U-Pb isotope, cathodoluminescence and microchemical evidence*; Contributions in Mineralogy and Petrology, **134**, p. 186-201.

Scott, D.J. & St. Onge, M.R. (1995): *Constraints on Pb closure temperature in titanite based on rocks from the Ungava Orogen, Canada: implications for U-Pb geochronology and P-T-t path determinations;* Geology, **23**, p. 1123-1126.

Siedlecka, A., Roberts, D., Nystuen, J.P. & Olovyanishnikov, V.G. (2004): *Northeastern and northwestern margins of Baltica in Neoproterozoic time: evidence from the Timanian and Caledonian Orogens;* In, Gee, D.G. & Pease,

V. (Eds.), The Neoproterozoic Timanide Orogen of Eastern Baltica; Geological Society, London, Memoirs, **30**, p. 169-190.

Siedlecka, A. & Roberts, D. (1996): *Finnmark Fylke, Berggrunnsgeologi, 1:500 000;* Norges Geologiske Undersøkelse.

Skoog, D.A., West, D.M. & Holler, F.J. (1996): *Fundamentals of Analytical Chemistry, 7th Ed.*, Saunders College Publishing.

Skår, Ø. (2002): *U-Pb geochronology and geochemistry of early Proterozoic rocks of the tectonic basement windows in central Nordland, Caledonides of north-central Norway;* Precambrian Research, **116**, p. 265-283.

Stacey, J.S. & Kramers, J.D. (1975): *Approximation of terrestrial lead isotope evolution by a two-stage model;* Earth and Planetary Science Letters, **26**, p. 485-494.

Streckeisen, A. (1976): *To each plutonic rock its proper name;* Earth Science Reviews, **12**, p. 1-33.

Stumpfl, E.F. & Sturt, B.A. (1965): *A preliminary account of the geochemistry and ore mineral parageneses of some Caledonian basic igneous rocks from Sørøy, Northern Norway;* Norwegian Geologiske Undersøkelse Årbok 1964, **234**, p. 196-230.

Sturt, B.A., Pringle, I.R. & Ramsay, D.M. (1978): *The Finnmarkian Phase of the Caledonian Orogeny;* Journal of the Geological Society, London, **135**, p. 597-610.

Sturt, B.A., Pringle, I.R. & Roberts, D. (1975): *Caledonian Nappe Sequence in Finnmark, northern Norway, and timing of orogenic deformation;* Geological Society of America, Bulletin, **86**, p. 710-718.

Silver, L.T. & Deutsch, S. (1963): *Uranium-Lead isotopic variations in zircons: a case study;* Journal of Geology, **71 (6)**, p. 721-758.

Torsvik, T.H. & Cocks, L.R.M. (2004): *Earth geography from 400 to 250 million years: a palæomagnetic, faunal and facies review;* Journal of the Geological Society, London, ???

Torsvik, T.H. & Cocks, L.R.M. (2003): *Lectures on reconstruction methods and palæogeography;* Course notes, Torsvik, T.H. (presenter), School of Geosciences, Wits University, S.A.

Torsvik, T.H., Smethurst, M.A., Van der Voo, R., Trench, A., Abrahamsen, N. & Halvorsen, E. (1992): *Baltica. A synopsis of Vendian-Permian palæomagnetic data and their palæotectonic implications;* Earth-Science Reviews, **33 (2)**, p. 133-152.

Townsend, C. (1986): *Thrust transport directions and thrust sheet restoration in the Caledonides of Finnmark, North Norway;* Journal of Structural Geology, **9**, p. 345-352.

Tremillon, B. (1965): Les *separations par les resines echangeuses d'ions;* Gauthier Villars, Paris.

Vavra, G., Gebauer, D., Schmid, R. & Compston, W. (1996): *Multiple zircon growth and recrystallization during polyphase Late Carboniferous to Triassic metamorphism in granulites of the Ivrea Zone (Southern Alps): an ion microprobe (SHRIMP) study*; Contributions to Mineralogy and Petrology, **122**, p. 337–358

Watson, E.B. & Harrison, T.M. (1983): *Zircon saturation revisited: Temperature and composition effects in a variety of crustal magma types;* Earth and Planetary Science Letters, **64**, p. 295-304.

Wetherill, G.W. (1956): *Discordant Uranium-Lead Ages;* International Transactions of the American Geophysical Union, **37**, p. 320-326.

Wiedenbeck, M., Allé, P., Corfu, F., Griffin, W.L., Meier, M., Oberli, F., Von Quadt, A., Roddick, J.C. & Spiegel, W. (1995): *Three Natural Zircon Standards for U-Th-Pb, Lu-Hf, Trace Element and REE Analyses;* Geostandards Newsletter, **19**, p. 1-23.

Zwaan, K.B., Cramer, J. & Ryshaug, P. (1975): *Prospekteringskartlegging I Kvænangen, Troms fylke*; Unpublished NGU-report nr. 1118/1.

Zwaan, K.B. & Roberts, D. (1978): *Tectonostratigraphic Succession and Development of the Finnmarkian Nappe Sequence, North Norway;* Norges Geologiske Undersøkelse, **343**, p. 53-71.